NASA CR-72950
EDD W-3207

# MULTISTAGE DEPRESSED COLLECTOR INVESTIGATION FOR TRAVELING-WAVE TUBES

by
Dr. I. Tammaru



HUGHES AIRCRAFT COMPANY
ELECTRON DYNAMICS DIVISION

prepared for

**NATIONAL AERONAUTICS AND SPACE ADMINISTRATION**

NASA Lewis Research Center

Contract NAS 3—11536

G. J. Chomos, Project Manager

Requests for copies of this report should be referred to

National Aeronautics and Space Administration
Scientific and Technical Information Facility
P.O. Box 33
College Park, Md. 20740

NASA CR-72950
EDD W-3207

FINAL REPORT

# MULTISTAGE DEPRESSED COLLECTOR INVESTIGATION FOR TRAVELING-WAVE TUBES

by

I. Tammaru

HUGHES AIRCRAFT COMPANY
ELECTRON DYNAMICS DIVISION
3100 WEST LOMITA BLVD.
TORRANCE, CALIFORNIA 90509

prepared for

NATIONAL AERONAUTICS AND SPACE ADMINISTRATION

June 1971

CONTRACT NAS 3-11536

NASA Lewis Research Center
Cleveland, Ohio

G. J. Chomos, Project Manager

# FOREWORD

The work described herein was performed at the Electron Dynamics Division of Hughes Aircraft Company under NASA Contract NAS 3-11536, with Dr. I. Tammaru as the principal investigator. The original collector scheme was proposed by Dr. O. G. Sauseng, who was also involved in the basic planning for utilizing the demountable apparatus for the collector evaluations. Mr. Gerald J.Chomos, Spacecraft Technology Division, NASA Lewis Research Center, was Project Manager.

TABLE OF CONTENTS

## ABSTRACT

Methods of analysis were developed for asymmetric multistage depressed collector schemes, with and without an initial transverse magnetic field. The scheme included beam expansion and refocusing into parallel flow prior to injection into the collector. A two-stage test collector was evaluated with a traveling-wave tube operated at 9 GHz and 4 kW output power for the purpose of verifying the analysis procedure. Satisfactory agreement was obtained between measured and predicted performance although some assumptions had to be made because of non-ideal experimental conditions. A four-stage asymmetric collector was designed, which promised to increase a tube efficiency of 28% to about 50%. It was concluded that a cylindrically symmetric collector is generally to be preferred over the asymmetric types that were investigated.

# I SUMMARY

An investigation was made of two asymmetric multistage depressed collector schemes for efficiency enhancement of traveling-wave tubes. One scheme utilized a transverse magnetic field for initial deflection of the beam, the other achieved a continuous transverse deflection with a slanting electric field. The collector was preceded by a section of reduced magnetic focusing field, designed to expand the beam and refocus it into approximately parallel flow, to reduce the beam spread in the depressed region due to space charge forces and angular velocity of the electrons. Analysis methods, based on a calculation of the entire electron motion from the beginning of the RF interaction to the capture in the collector by digital computer programs, were developed.

A two-stage test collector employing initial magnetic deflection was constructed and evaluated in a demountable apparatus with a solenoid focused traveling-wave tube at 9 GHz and 4 kW RF output power. The performance of the collector, which was not an optimized design, was used for verifying the validity of the analysis. The predicted performance agreed with measurements with the exception that the current to the first depressed stage was considerably smaller than estimated. The analysis was subsequently modified by including the effect of space charge forces due to beam bunching and, approximately, the effect of residual rotational motion in the spent beam. The corrected performance predictions were generally in satisfactory agreement with experimental values, even though a number of perturbing effects were present in the experiment. Some assumptions had to be made, however, to correct for reduced current transmission into the collector and imperfect shielding of the depressed collector region, which permitted some electrons to escape to the surrounding vacuum envelope.

An asymmetric electrostatic collector with four depressed stages was designed, which had a predicted efficiency of 62 percent. If operated with the traveling-wave tube used in the two-stage collector experiment, it would raise the undepressed tube efficiency of 28 percent to an estimated 50 percent. An effort was made to minimize the effect of variations in the velocity components of the incident electrons; this lends greater validity to the performance estimate.

The estimated efficiency of the asymmetric collector was comparable to the demonstrated efficiency of a cylindrically symmetric electrostatic collector. Because the construction as well as analysis of an asymmetric collector are more complex, it was concluded that, except for certain applications, a symmetric collector is generally more practical.

# II INTRODUCTION

The work described in this report is part of a continuing effort to increase the efficiency of high power transmitting systems for satellite applications. A high efficiency RF power source has the two-fold advantage of requiring less prime power and reducing the problem of heat rejection. Both of these advantages are very desirable in a space system.

The specific task consisted of an investigation of a multistage depressed collector, for enhancing the efficiency of traveling-wave tubes by recovering part of the kinetic energy in the spent beam. It was proposed in the final report to NASA Contract NAS 3-9719, entitled "Analytical Study Program to Develop the Theoretical Design of Traveling-Wave Tubes".[1] Although depressed collectors have been commonly used for efficiency improvement of electron beam devices, it is only recently that their design has been approached by satisfactory analytical methods.[2,3,4] It seems imperative that a successful design of a collector with several depressed stages should be based on trajectory calculations which are in some manner representative of the actual electron paths.

The electron velocities in the spent beam entering the collector are often guessed at in some way. A unique feature of the present study is that an attempt was made to calculate the entire electron motion from the beginning of the interaction with the RF wave to the capture in the depressed collector. The analysis method is thus conceptually very appealing.

The original program plan consisted of the development of analysis methods; the evaluation and optimization of a two-stage depressed collector in a demountable apparatus, for the purpose of verifying or correcting the analysis methods; and the design and evaluation of a multistage collector with up to five depressed stages. The collector scheme originally proposed for the investigation was an asymmetric one with initial deflection of the beam by a transverse magnetic field.

During the course of the work the plan was somewhat modified. Difficulties encountered with maintaining an adequate vacuum in the demountable apparatus during processing and testing delayed the evaluation of the first two-stage collector considerably. The test results, when finally obtained, indicated that a correction to the trajectory input conditions into the collector for the low and medium energy electrons was desirable. After the analysis procedure had been corrected, by including some additional effects, a better agreement with the measured performance was obtained.

In the meantime, improved two-stage collectors had been designed, one with initial magnetic deflection and one all-electrostatic collector with transverse deflection. Since both of these designs were based upon the original trajectory input conditions, they did not represent truly optimized designs, and their experimental evaluation was not considered sufficiently useful.

A detailed study of the experimental conditions and results indicated several possible perturbing influences, which were present because of the complexity of the collector scheme and geometry. The final multistage collector, an all-electrostatic asymmetric configuration with four depressed stages, was therefore designed to minimize the effect of uncertainties in the beam composition, at the cost of some efficiency degradation. Comparable efficiencies had been demonstrated elsewhere, and even higher efficiencies had been predicted, with electrostatic collectors of simpler geometry, possessing cylindrical symmetry. The designed asymmetric collector did thus not appear as practical as a symmetric one; upon request from NASA it was not evaluated.

In collector design analysis, the concept of collector efficiency is a very convenient figure of merit for comparing one collector design with another. It will be frequently referred to in this report, and is discussed in some detail in Appendix A; its relation to the often more directly useful DC-to-RF power conversion efficiency is also given.

## III. THE ORIGINAL, AND A MODIFIED, MULTISTAGE DEPRESSED COLLECTOR SCHEME

The essential process in multistage depressed collector operation is the sorting of the spent beam electrons according to their energy, and the collection of the electrons at different potentials.

The basic collector scheme, which was proposed for these studies, is illustrated in Figure 1. The electron sorting in this collector is accomplished in two steps. Initially the spent beam is subjected to a transverse magnetic field, which provides a deflection force perpendicular to the axial direction in an amount inversely proportional to the electron velocity. The slow electrons therefore acquire a greater deflection in angle than the fast ones. The main sorting is produced by an electrostatic field, which is maintained in the collector region proper by fixed voltages on the electrodes. The amount of depression increases with distance into the collector, in an approximately linear relation. The fast electrons penetrate deep into the collector, before being reflected, and are collected on one of the more depressed electrodes; the slow electrons penetrate a smaller distance and are collected on a less depressed electrode. Because most electrons are intercepted by the collector electrodes on the top (far side) surfaces, most of the secondary electrons produced by the impacting primaries will be suppressed by the electrostatic depression fields.

The sorting efficiency of this collector scheme depends on the vector velocity distribution of the beam entering the collector region. It is evident from considering the two high energy edge trajectories in the figure, for example, that an initial divergence of the beam will have a degrading effect on the performance. One of the displayed trajectories would tend to miss the most depressed electrode after being reflected, while the other might strike the electrode on the near side surface. Since at these surfaces no electrostatic barrier is present to prevent secondary electrons from cascading down to the next, more positive electrode, this will directly reduce the collector efficiency. The ideal condition is to have the beam electrons enter the collector in approximately parallel flow with minimum radial velocity spread. The purpose of the "refocusing region" shown in the figure is to produce such a beam flow from the less uniform (more disordered) electron motion present in the spent beam emerging from the output coupler.

It was indicated how an initially diverging beam is undesirable for effective collector operation. A beam divergence which is produced close to the collector entrance by reasons other than an initial trajectory spread is generally also undesirable. In the present investigation, which was made at X-band at an RF power level of 4 kW, there are strong space charge forces in the beam, which in the interaction region of the traveling-wave tube are balanced out by the magnetic focusing field. As the main focusing field is terminated just prior to the collector region, the beam tends to spread quickly as a result of these space charge forces. An additional effect is present for a semi-confined solenoid focused beam, originating from an

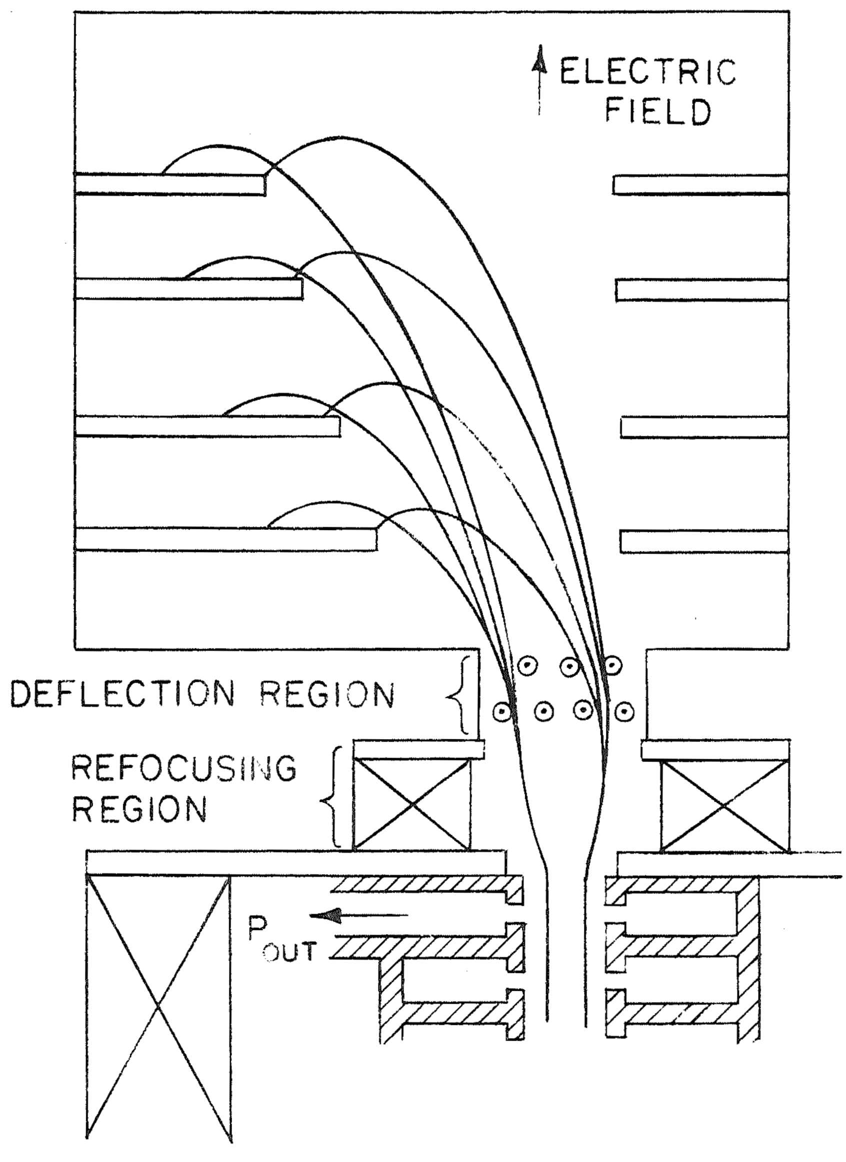


Figure 1 Original multistage depressed collector scheme.

unshielded cathode, such as here being considered. Such a beam, associated with non-zero cathode flux, will acquire angular momentum upon entering a field free region. This also tends to spread the beam. In the present case, in fact, the beam spread due to non-zero cathode flux dominates the space charge effect. A remedy for preventing the rapid beam spread in the collection region is to let the beam expand before being refocused into parallel flow. This reduces both the space charge forces and the angular velocity of the electrons in a field free region.* Preliminary analysis with a DC beam, described in Appendix B, revealed the necessity for first expanding the beam, and the original concept was modified accordingly. The expansion was accomplished by maintaining a reduced magnetic field over a suitable axial distance, as discussed in Appendix B.

Before proceeding with the detailed analysis of the system, the experimental apparatus will be described in the next section.

---

* By Busch's theorem, the angular velocity of an electron in an axially symmetric system is given by

$$v_\theta = r\,\dot{\theta} = \frac{1}{2}\,(e/m)(rB - r_c^{\,2}\,B_c/r),$$

where r is the distance of the electron from the axis and B is the axial field, here considered uniform over the circle with radius r; $r_c$ and $B_c$ are the corresponding quantities for the electron at the cathode. In a field free region (B = 0) an angular velocity due to the cathode flux remains. This angular velocity decreases with increasing r.

## IV. DESCRIPTION OF APPARATUS AND MEASUREMENT SETUP

The experimental collector evaluation was done in a previously developed demountable apparatus, which was modified for the collector experiments. A stacked coupled cavity circuit at X-band, producing 4 kW of saturated output power, was used to generate an RF modulated spent beam. The solenoid focused DC beam from the gun had been examined in a magnetic demountable beam analyzer for a separate contract. The beam characteristics, both those used in the analysis and the measured values, are listed in Table I. In the analysis, an ideal DC beam entering the slow wave circuit was assumed, although the actual scalloping radius of the beam was close to a maximum at the first interaction gap. It was verified, however, that such an entrance condition did not significantly change the results.

TABLE I DC BEAM CHARACTERISTICS

| PARAMETER | DESIGN VALUE | ACTUAL VALUE |
|---|---|---|
| Operating voltage, $V_o$ | 16 kV | 16 kV |
| Beam perveance | .46 μperv | .43 - .44 μperv |
| Beam diameter, $2r_o$ | .060" (.152 cm) | .061" (.155 cm) |
| Beam ripple | --- | 5 % |
| Scalloping wavelength | --- | .5" (.127 cm) |
| Focusing Field, $B_o$ | 1870 gauss (.187 T) | 1850 - 2150 gauss (.185 - .215 T) |
| Cathode flux, $k^*$ | .87 | .80 |

* The cathode flux parameter k is defined by the ratio $\psi_c/\pi r_o^2 B_o$ where $\psi_c$ is the flux through the cathode.

### DEMOUNTABLE APPARATUS

The main components of the demountable apparatus including the focusing solenoid, are displayed in Figure 2. A schematic of the assembly is shown in Figure 3. The stacked coupled cavity circuit is mounted on a baseplate, which supports the input and output waveguide guides and the electron gun assembly. The base also constitutes part of the lower pole piece for the focusing solenoid (not shown in Figure 3) which fits around the main vacuum envelope and rests on the vacuum flange

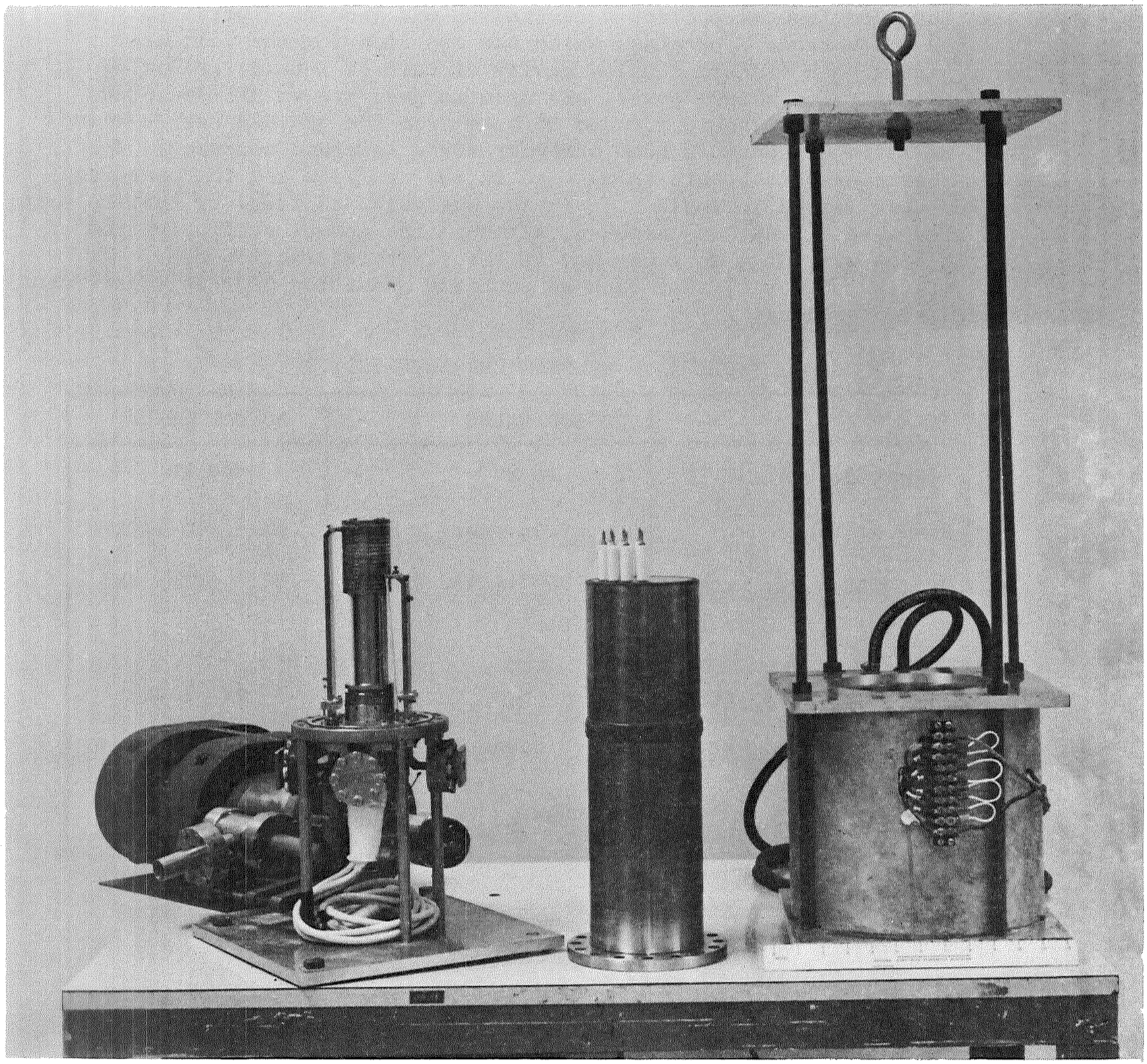

Figure 2 Demountable apparatus for collector evaluations. (A one foot rule rests at the base of the solenoid to the right.)

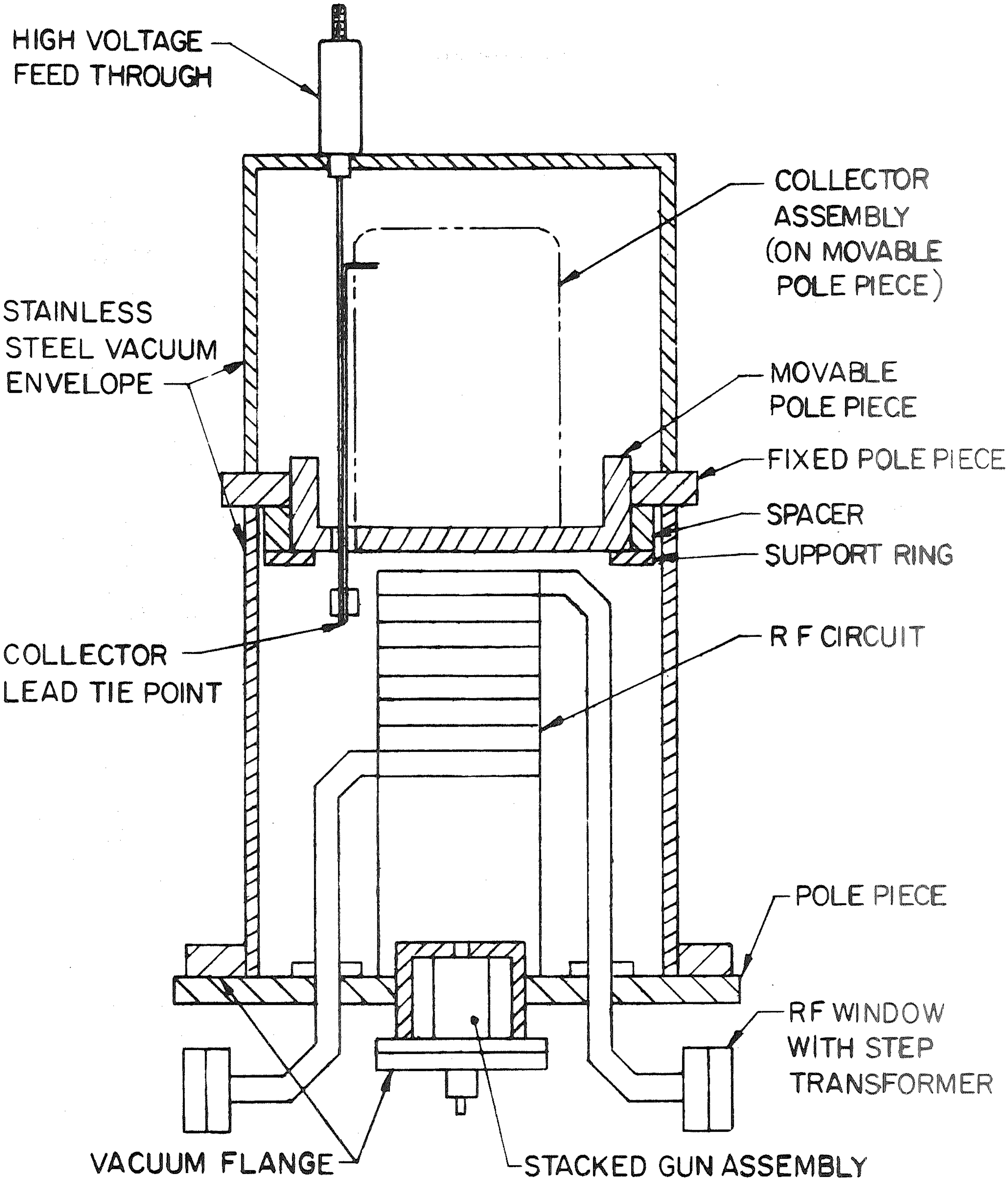


Figure 3    Schematic of demountable apparatus.

at the bottom. A copper gasket provides the vacuum seal between the welded vacuum envelope structure and the base. The electron gun assembly is stacked and spring loaded, and can be removed without disturbing the interaction circuit or the focusing configuration.

The collector structure is assembled onto a separate base, the "movable pole piece" in Figure 3, with the electrical connector leads, insulated by ceramic tubes, projecting through holes in the pole piece. Upon assembly of the system, the movable pole piece with the collector structure is inserted into the open vacuum envelope from the bottom end. Connector leads brazed to the high voltage feed-throughs on the top, and insulated by ceramic tubing, are guided through the holes in the process. The movable pole piece is secured by a spacer and a support ring to a pole piece ring, which is part of the vacuum envelope. The collector leads are connected to the feedthrough leads as the final step before placing the vacuum envelope into position on the base and tightening the vacuum seal.

The system is baked out by an oven which is lowered over the vacuum envelope. A separate water-cooled plate allows control of the temperature of the base. This is desirable in order to prevent repeated thermal stress on the ceramic feedthroughs in the base and the gun, and on the RF vacuum windows. The bakeout temperature was generally 300°C, with the base kept at around 100°C.

COLLECTOR ASSEMBLY

A schematic of the assembled two-stage test collector is shown in Figure 4; a photograph of the unit is presented in Figure 5. The collector is mounted on three stacking bolts, which are press fitted into the movable pole piece. The electrodes, with circular holes offset from the beam axis, are insulated from the stacking bolts by ceramic tubes and held in place by ceramic spacers. Shields attached to the electrodes minimize the effect of the surrounding grounded vacuum envelope on the potential distribution in the collector. They also help prevent electrons from escaping from the depressed region. The ceramic spacers are provided with shields to prevent their charging up.

The refocusing magnet, shown in Figure 6, consists of a foil-wound solenoid with 133 turns inside a vacuum-tight stainless steel can. It fits into a recess in the movable pole piece, which is thus the common pole piece between the main solenoid and the refocusing solenoid. An insert allows convenient modification of the pole piece hole configuration. The second pole piece of the refocusing solenoid rests on top of the non-magnetic solenoid vacuum can. This pole piece may be insulated from the can by a thin mica sheet for the purpose of measuring the intercepted current on it separately.

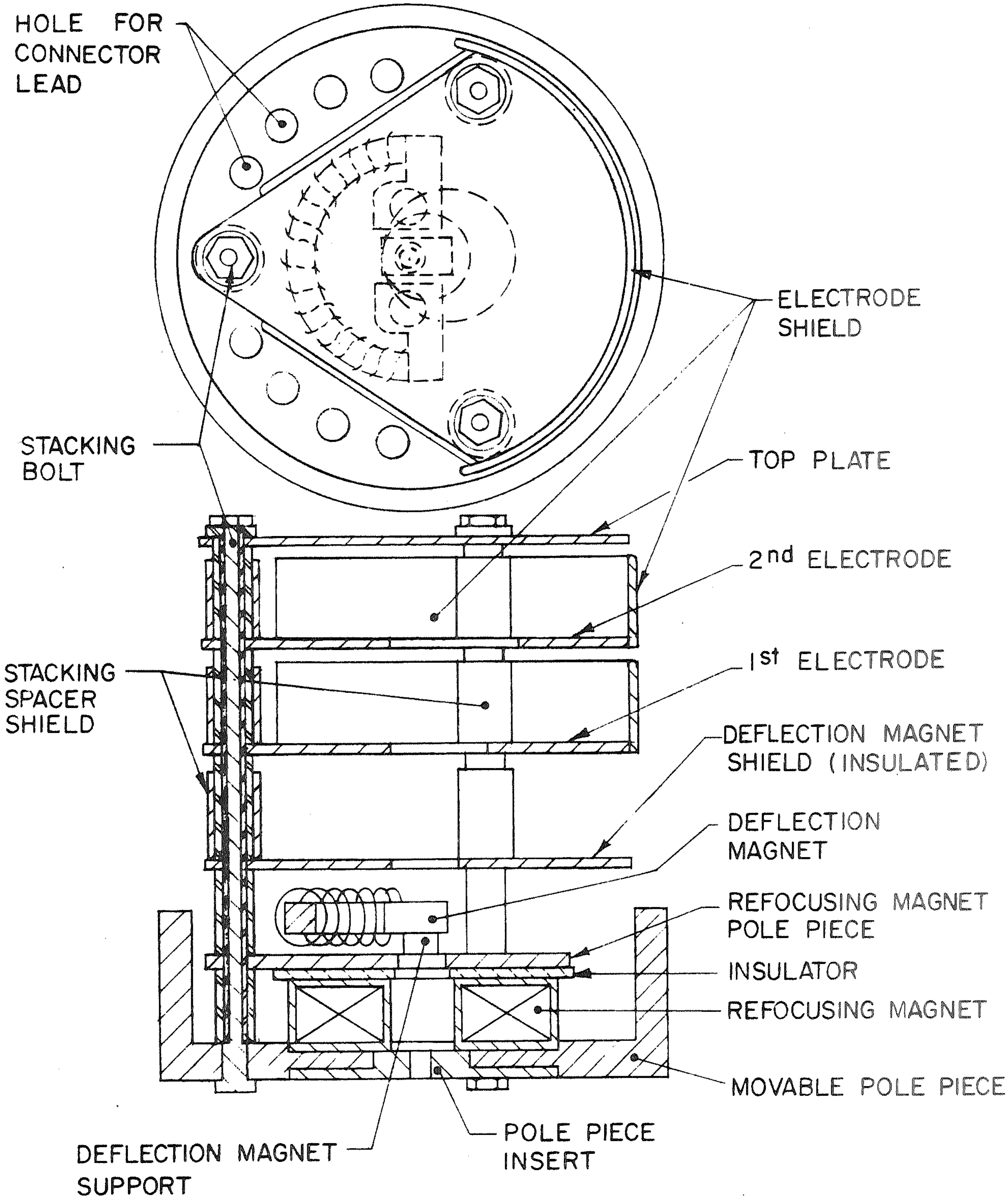


Figure 4 Schematic of two-stage test collector.

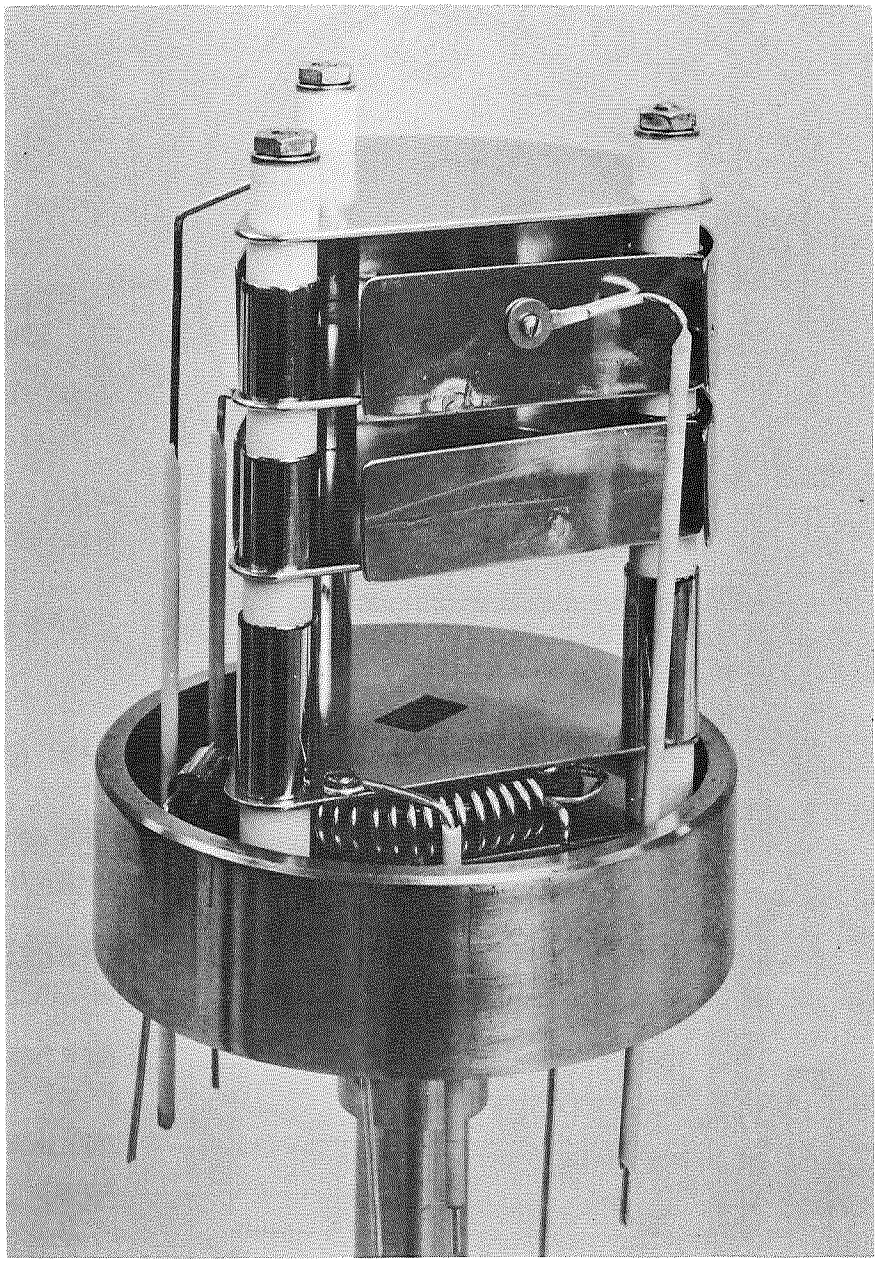

Figure 5    Assembled two-stage test collector.

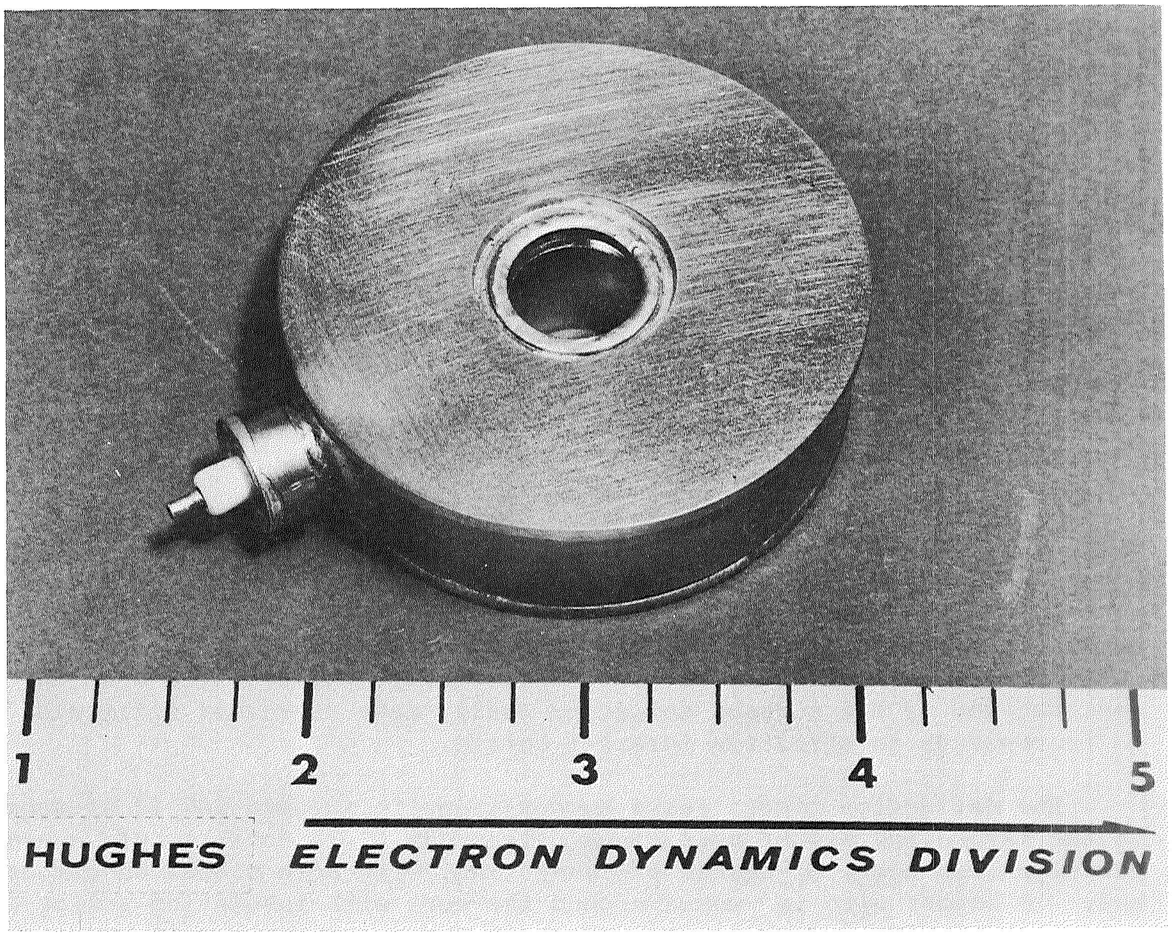


Figure 6 Refocusing solenoid (the scale, for size comparison, is in inches).

The magnet configuration of the refocusing section is exhibited in Figure 7. Also shown is the estimated field on the axis, obtained by superposition of Molnar-Moster type field transistions[5] at the three relevant pole piece faces. For convenience, this idealized field shape was used in the computer calculations, since it can be expressed by simple mathematical expressions. The measured field in the refocusing region was similar to the idealized one, except that the field between the two pole pieces was somewhat more peaked in the middle. This was principally caused by construction and insulation constraints, which prevented extending the current-carrying solenoid foil all the way to the pole pieces on either side. In the experimental case, an adjustment in the magnitude of the refocusing field was possible, by which some compensation of the difference in shape could be made. The magnitude of the refocusing field was typically 40% of the main focusing field, or about 800 gauss (.08 T); this was produced with a current of 8 A.

The axial leakage field into the collector was about 3%. It was produced almost entirely by the main solenoid. A magnetic shield was placed outside the vacuum envelope, but it was less effective than anticipated. A similar type shield for a conventional depressed collector on the demountable apparatus had been used successfully in the past, but the size of that collector had been appreciably smaller. The complex construction of the present collector would make it rather difficult to incorporate an effective internal shield.

The deflection magnet rests on non-magnetic spacers and is attached to the refocusing magnet pole piece (Figure 8). It consists of a semicircular iron core, of square cross-section, with pole pieces on either end. A copper wire is wound around the core with insulating strips of mica in between.

The transverse deflection field in the beam region is established between the pole pieces as shown in Figure 9. A magnetic shield, suspended on the stacking bolts, limits the extent of the field into the depressed collector region. It has a rectangular aperture (seen in Figures 4 and 5) to maintain, as far as possible, a uniform transverse field over the beam area in a given axial plane.

The shape of the transverse field on the axis, which was used in the collector trajectory analyses, was intially calculated with a computer program. The measured field configuration was later verified to be in excellent agreeement with predictions. The deflection field was adjusted in the calculations to give a deflection angle* of about $11^{o}$ (.2 rad) for spent beam electrons with an average energy of 12 kV. In the given configuration, this required a peak transverse field of about 80 gauss (.008 T), which was obtained with a current of 4 A through the coil.

*For small deflections the deflection angle is proportional to the integral of the magnitude of the transverse field over the path length.

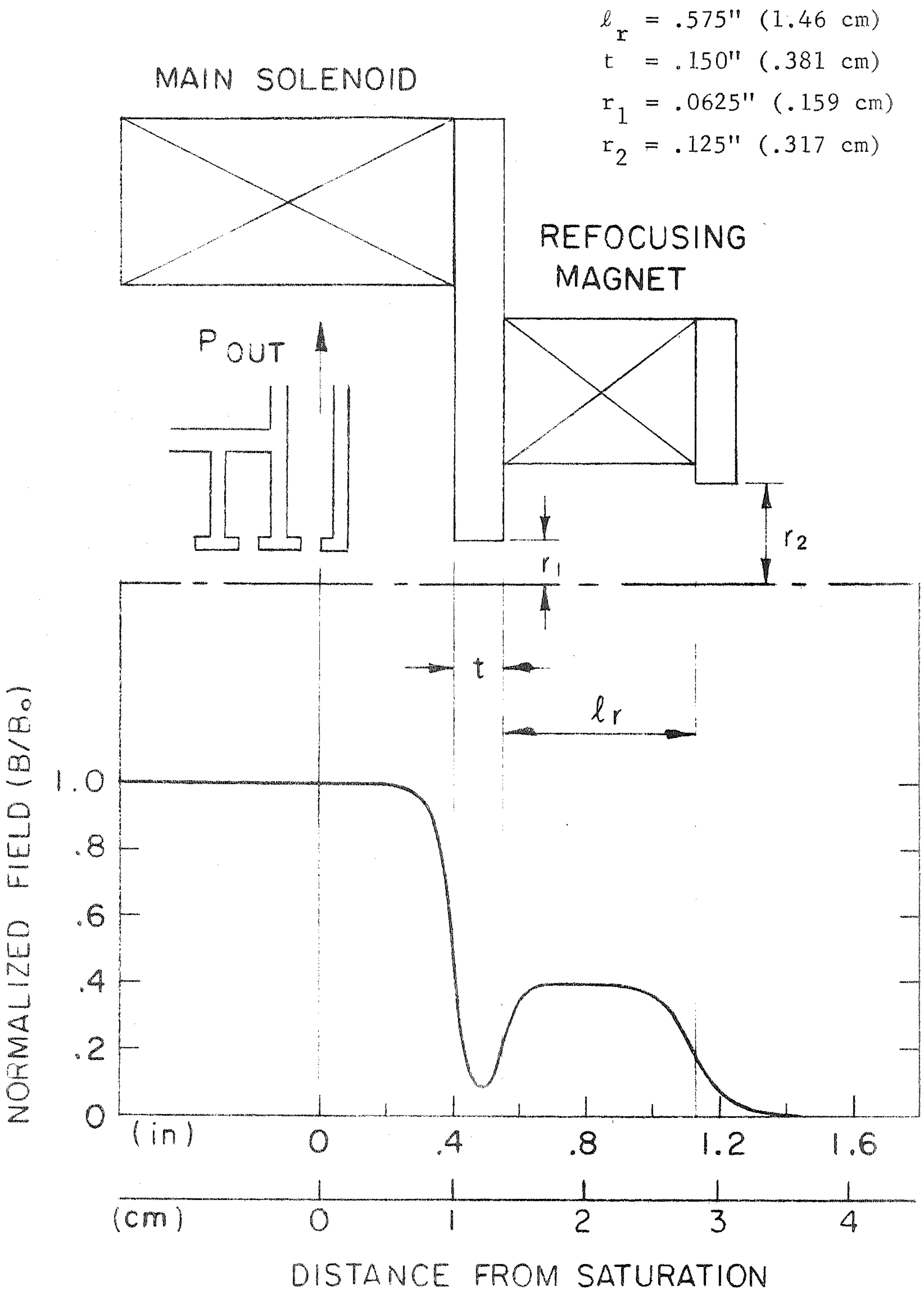


Figure 7 Refocusing magnet configuration and magnetic field on the axis.

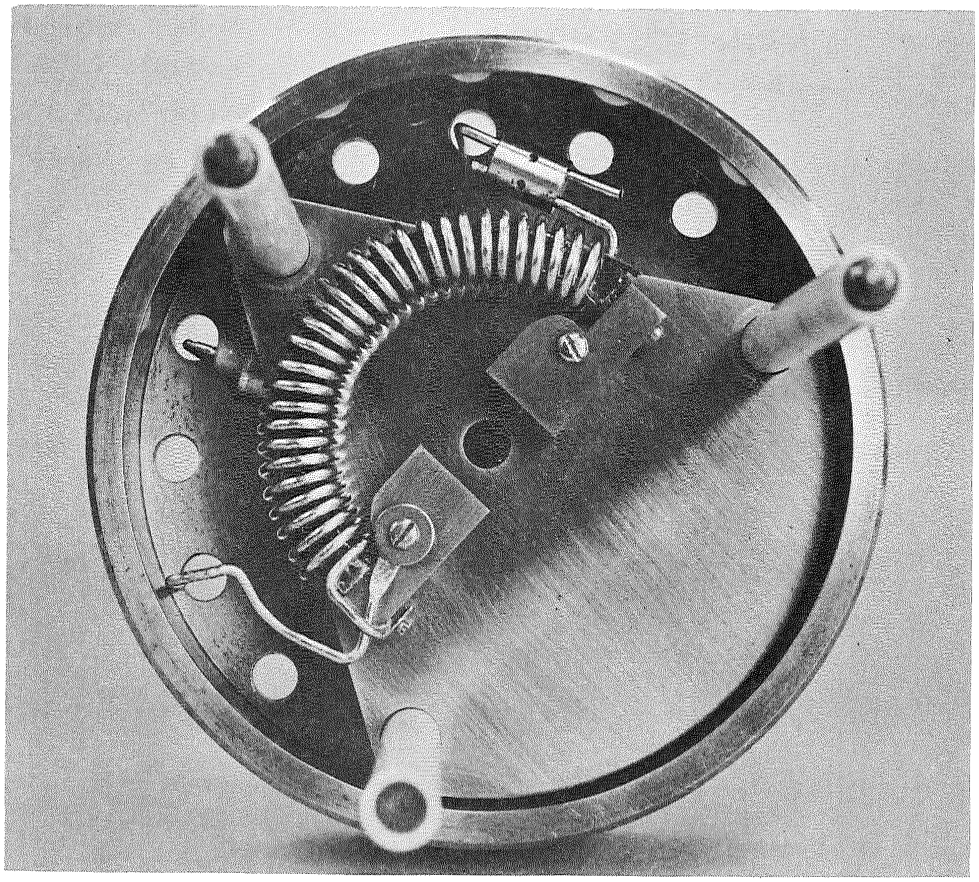

Figure 8 Deflection magnet mounted on the refocusing magnet pole piece.

$g$ = .50" (1.27 cm)
$d$ = .50" (1.27 cm)
$\ell_d$ = .20" (.508 cm)

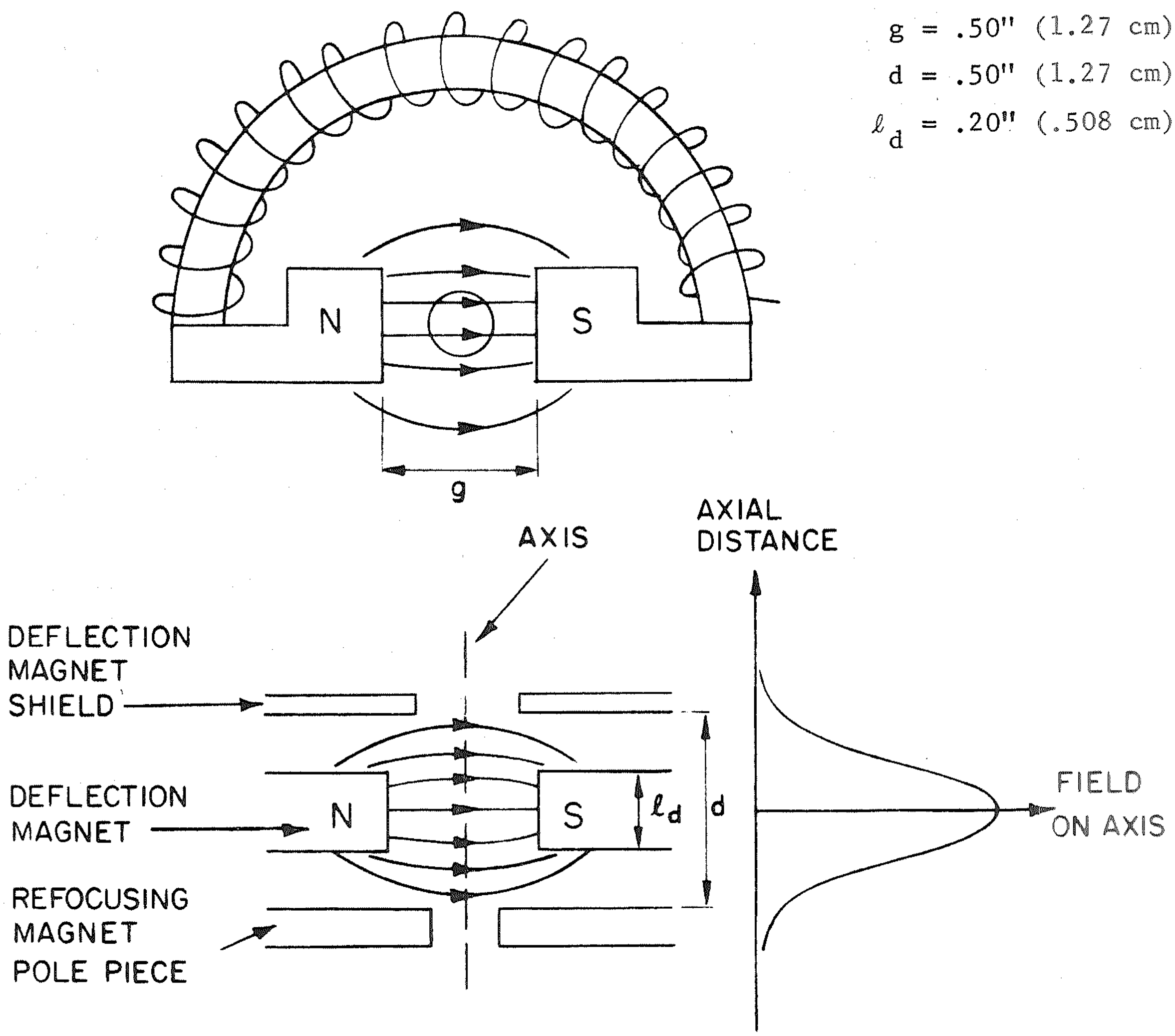


Figure 9 Deflection magnet and field configurations.

## MEASUREMENT SETUP

The collector was evaluated in the demountable apparatus by operating the traveling-wave tube in a cathode pulsed mode. Thermal considerations could thus be disregarded in the design of the collector. The pulse repetition rate was 100 pulses per second, and the pulse width 6 $\mu s$, giving a duty factor of .06%.

The electrical diagram for the measurements on the two-stage test collector is shown in Figure 10. A high power dropping resistor could be used to select various electrode voltages. The actual voltage during a current pulse was measured with a calibrated capactive voltage divider in conjunction with a precision voltage comparator. In practice, the voltages on electrodes No. 1 and 2 were maintained by available DC supplies which were provided with RC filters having long time constants. The supplies were calibrated with an accurate electrostatic voltmeter. The currents to the depressed electrodes (including the end plate), the deflection magnet shield, the deflection magnet - refocusing magnet pole piece assembly, the body (vacuum envelope), and the cathode were measured independently with calibrated current - viewing toroids. The currents could usually be measured within 1 mA, except for the body current pulse which tended to exhibit instability; for consistency, the magnitude of the body current was instead calculated from the other currents. In a second experiment the coupled cavity stack was isolated, and the current intercepted by the RF circuit was also measured.

The RF setup is shown in Figure 11. The RF input power was supplied by an X-band magnetron which was pulsed synchronously with the cathode. A klystron, which could be operated either CW or in pulsed mode at the same frequency as the magnetron, provided a power reference in the experiments. In the CW mode the klystron output power could be directly measured with the power meter. When the klystron was switched to pulsed mode, the peak power remained unchanged. A reference of a known peak power could therefore be displayed on the oscilloscope. Both the input and the output power pulses could be sampled and switched for display on the same scope. A calibration of the appropriate legs thus allowed direct measurement of the pulsed input and output power levels.

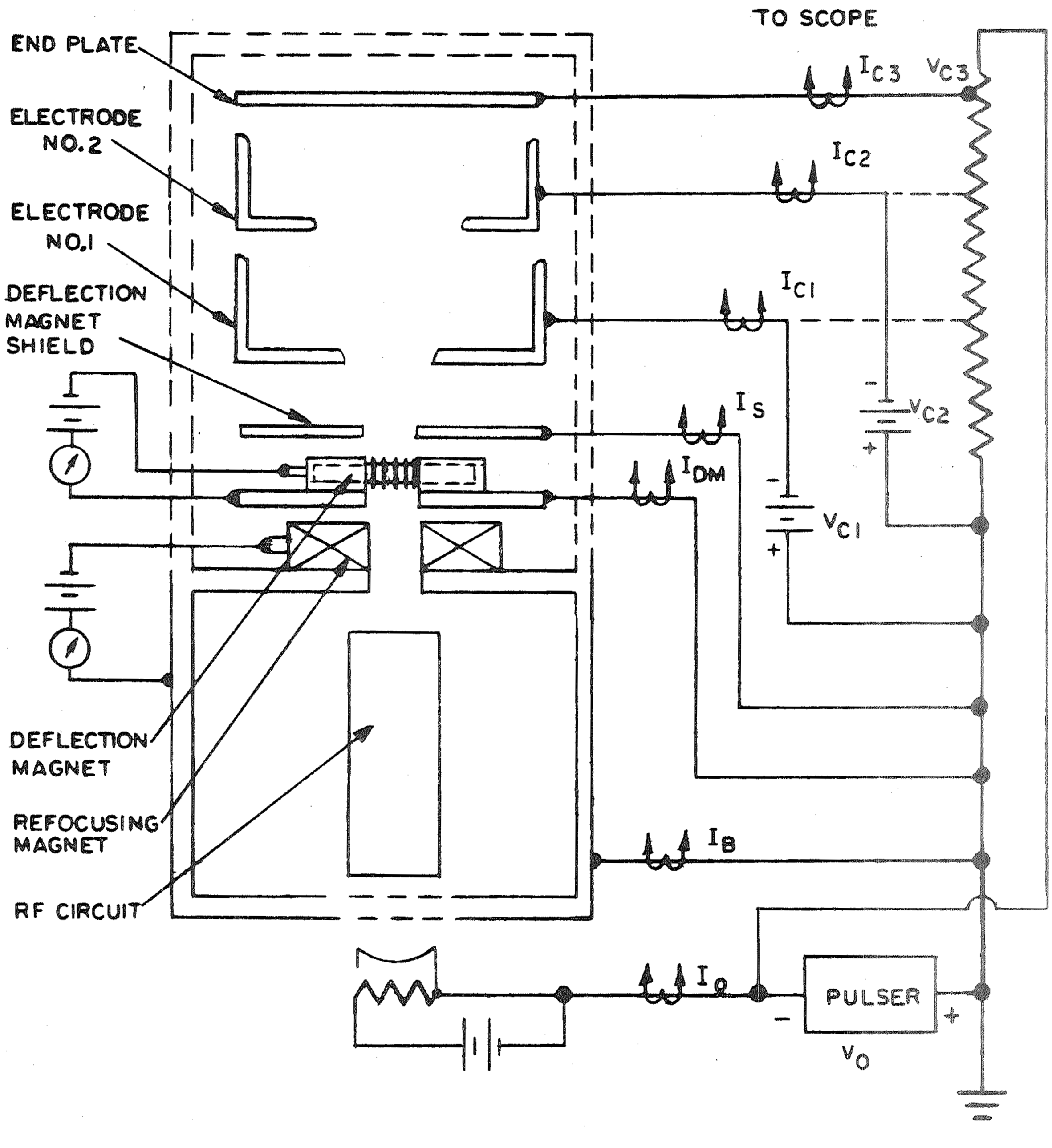


Figure 10 Electrical diagram for collector measurements.

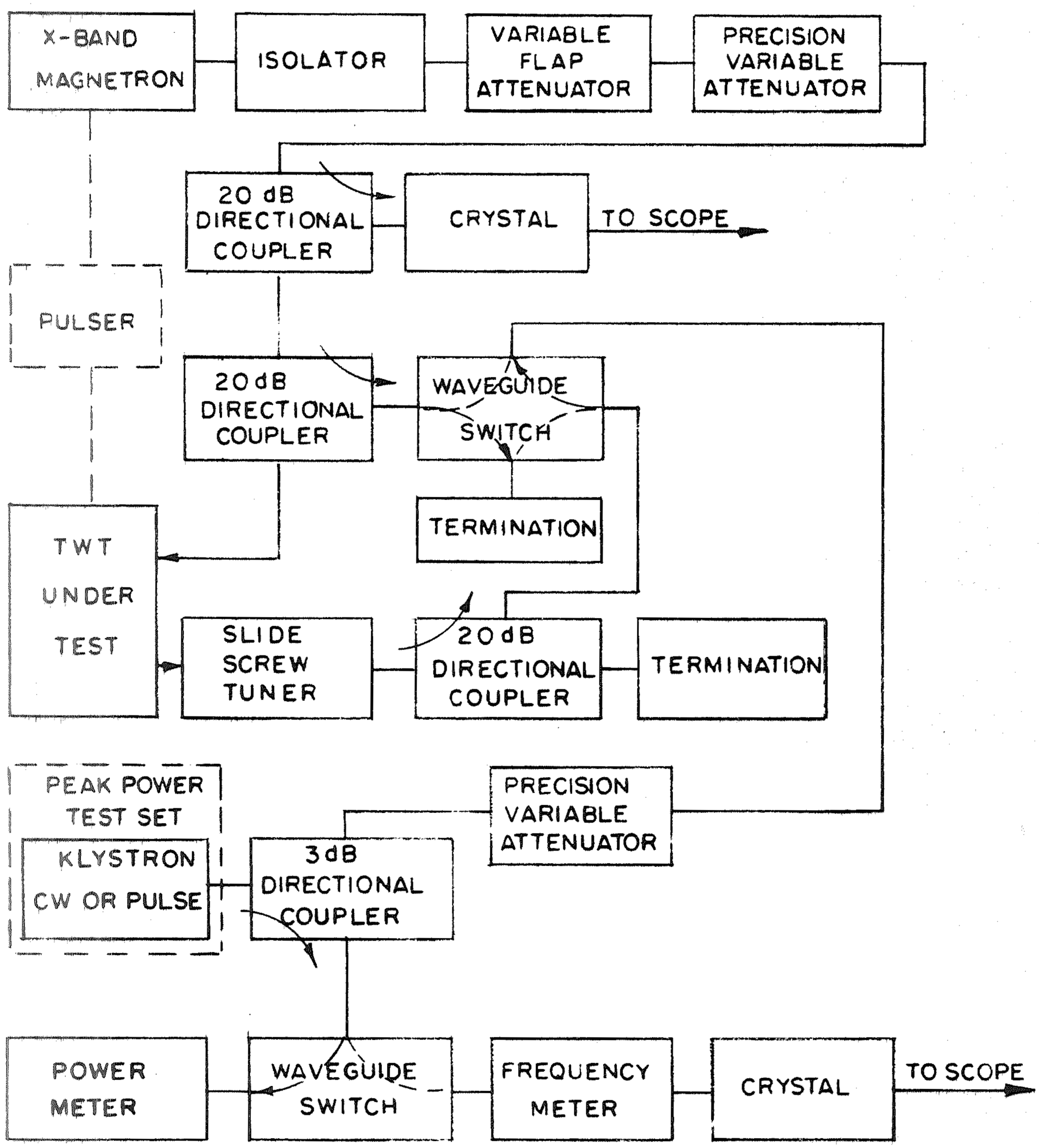


Figure 11 RF setup.

## V. METHOD OF ANALYSIS

The electron motion in the traveling-wave tube and the collector was analyzed with two digital computer programs. A two-dimensional large signal program, based on a charge disk model of the electron beam with variable disk radii,[6] was used to calculate the motion in the interaction region and through the refocusing section. The deflection region and the depressed collector region proper was analyzed with a trajectory program. Initially, the two-dimensional program did not include the space charge forces due to the beam bunching, which results from interaction with the RF wave. Although the majority of the trajectory calculations for the collector were based on trajectory launching conditions derived from this program, these computer runs are still useful in indicating the general effect of modifications in the collector design. In the present section, the original analysis method will be described in detail. The effect of the RF space charge forces will be taken up in Section VII.

Before the actual electron trajectory computations were initiated, a preliminary large signal analysis of the test circuit was carried out with a one-dimensional computer program in order to select suitable operating conditions for the efficiency evaluations. Some of the results of this investigation are presented in Appendix C. A beam voltage of 16 kV was selected for all the subsequent work.

### ANALYSIS OF THE REFOCUSING SECTION

The previously mentioned two-dimensional large signal computer program was used for calculating the electron motion in the refocusing section. The program, developed by Dr. H. K. Detweiler of Jet Propulsion Laboratory, was acquired for refocusing studies carried out under NASA Contract NAS3-11539. Several features were added to the program, among them plotting routines and a magnetic field option, in which a refocusing-type field could be specified by means of the relevant magnet parameters.

The analytical design of the refocusing field, shown in Figure 7 in the previous section, was derived by calculating the spent beam electron trajectories through the refocusing region, and changing the refocusing parameters until the desired beam expansion and beam flow at the output was obtained. The most significant parameters are the magnitude of the refocusing field and the length of the refocusing magnet. In the present case the refocusing field is 40% of the main field and the magnet length is .575" (1.46 cm) between pole pieces, or about 20 times the beam radius.

The effect of the refocusing section is seen in Figure 12. The edge radius of every other disk of the 32 disks used in the beam model has been plotted as a function of axial distance. The interior electrons in each disk are assumed to move in a laminar flow relation with the calculated edge electron. The beam composition at the end of the refocusing section is thus completely determined.

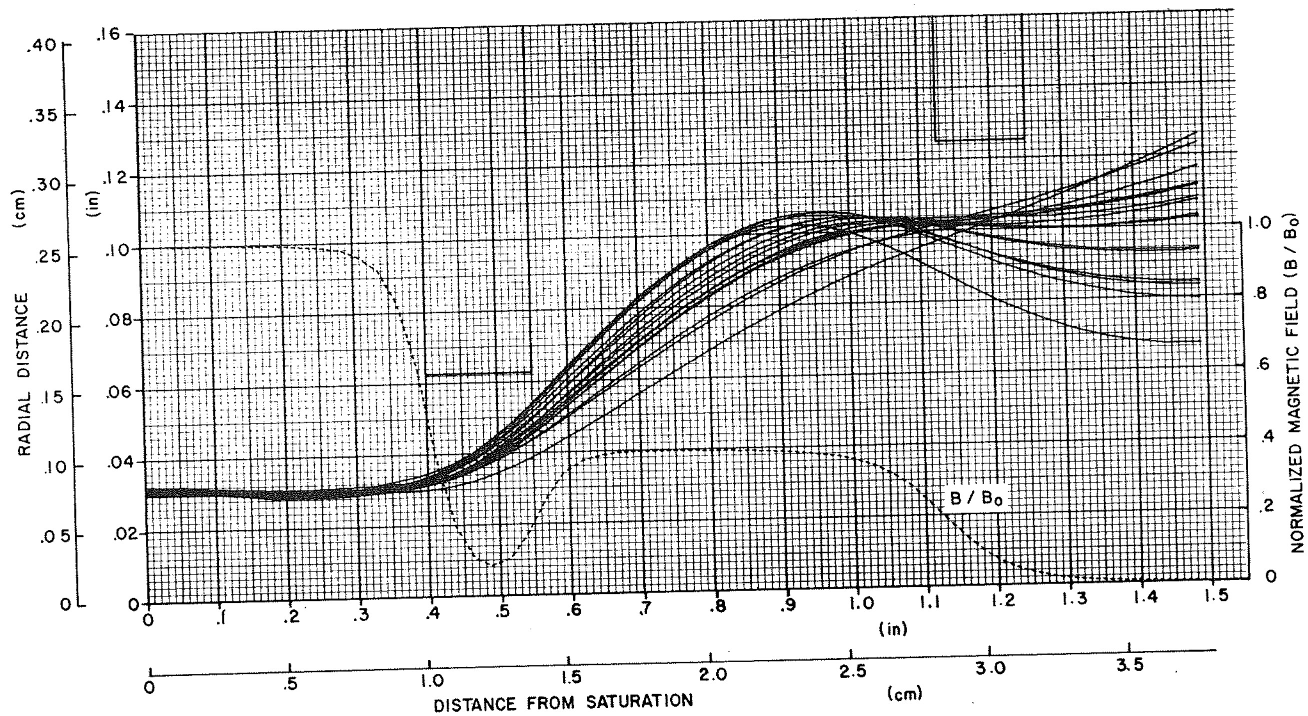


Figure 12 Disk edge trajectories in refocusing section (calculated without RF space charge forces).

Graphical information on the beam composition at the end of the refocusing section, 1.15" (2.92 cm) from saturation, is supplied by the plots in Figure 13. The first plot is an energy distribution graph which has been generated in the following way. The disks are ordered according to increasing energy. Then they are plotted in histogram fashion with the highest energy disk represented by a strip adjoining the horizontal, normalized energy (voltage), axis. The other disks are similarly plotted on top of the first strip in order of decreasing energy. A smoothed curve is obtained by joining the energy values at the midpoints of each strip. The other graphs are plots of the disk radii, and the trajectory slopes. They are presented in histogram form with the disks (strips) arranged in order of increasing energy, in the same way as in the energy distribution histogram.

A noticeable property of the refocusing section is that it produces a certain type of energy sorting of the electrons, as may be seen from the plot of the trajectory slopes. The trajectory angle increases from a negative value to a positive value in a fairly continuous fashion as a function of disk energy, while the disk radii are fairly constant. This makes it reasonable to represent the beam at the output of the refocusing section by a reduced number of energy groups, as is desirable in a trajectory model of the beam for the collector analysis.

## TRANSITION TO THE COLLECTOR

A realistic analysis of the depressed collector should be based on the actual potential distribution, which exists as a result of the different electrode voltages and the presence of the beam space charge in the collector region. Digital trajectory computer programs are available for such analysis provided the electron flow may be considered stationary (time-independent).

Although the spent beam from a traveling-wave tube is bunched, i.e., the charge flow is time-dependent, the bunches disperse relatively quickly after the RF wave has been removed, as a result of both the velocity spread of the electrons and the space charge forces. This has been found experimentally,[7] and is also demonstrated theoretically in Appendix D. The spent beam at the output of the refocusing section may thus be considered as being composed of many DC beams with varying velocities.

A trajectory analysis of the collector requires a representation of the spent beam in which several rays are launched over the beam cross-section, with each ray carrying an appropriate amount of current. A conversion from the disk model to the current ray model could, in principle, be made by representing each disk with a given number of rays at various radial positions, all of which have an axial velocity equal to the axial velocity of the disk. The method is impractical, however, since the number of rays would become excessively large. Instead, the approach that has been taken is to group together several disks with approximately the same energy and represent

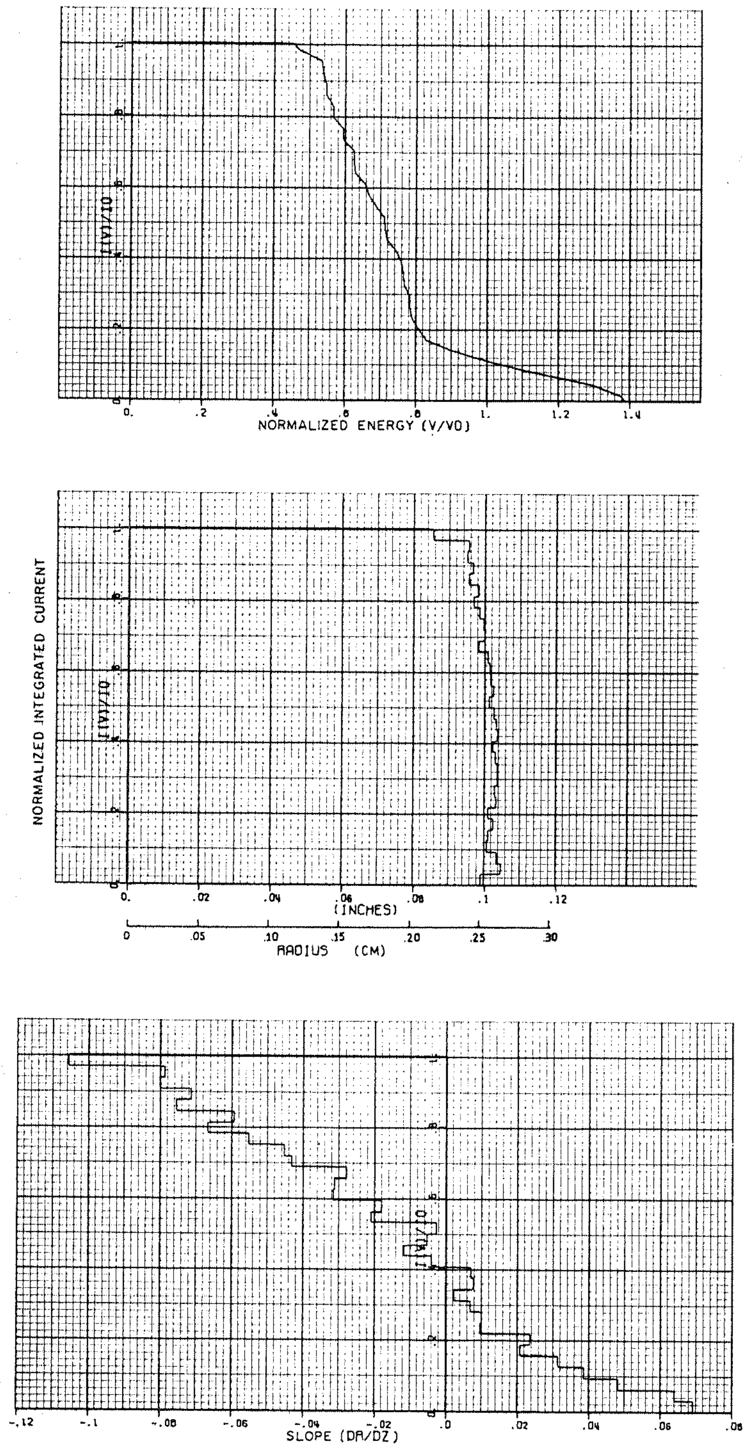


Figure 13 Spent beam composition at output of refocusing section (calculated without RF space charge forces).

each group by a set of rays over the beam area. For such a representation to be appropriate, all the disks with nearly the same energy, which would be included in a group, should also have nearly the same radius and the same trajectory slope of the edge electrons.

As was noted in the previous section, a property of the refocusing field is to provide a type of sorting of the disks which is principally dependent on the disk energy, in such a way that this condition is approximately satisfied. This was seen in Figure 13. In the collector computations, the spent beam was usually represented by five energy groups, although initially a number of runs were made with a four energy-group model. The spent beam distribution data in Figure 13 are therefore approximated by five discrete-step distributions as illustrated in Figure 14.

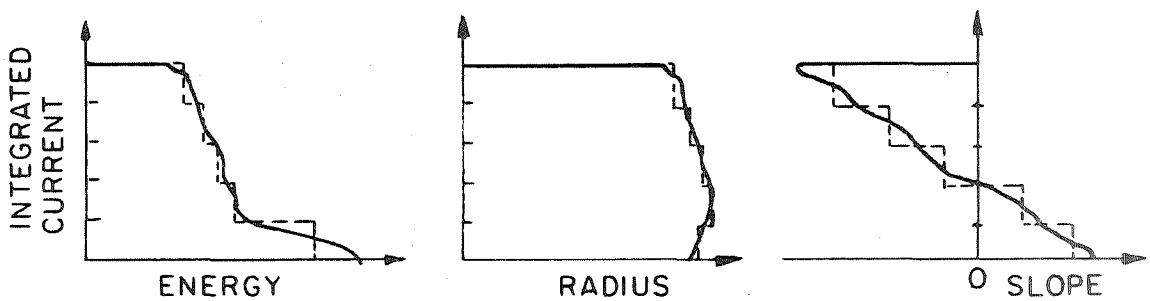


Figure 14 Five energy-group model of the spent beam.

Each group of disks, identified by a value of the subscript j, is then described by the following parameters:

| | |
|---|---|
| Electron energy | $V_j$ |
| Disk edge radius | $r_j$ |
| Edge trajectory slope | $(dr/dz)_j$ |
| Current | $I_j$ |

Table II gives the parameters of the four and five energy-group models of the beam derived from the spent beam distribution of Figure 13. In the five energy-group model of the beam, an equal current distribution among the groups was assumed, as indicated in Figure 14.

TABLE II PARAMETERS OF THE REDUCED ENERGY-GROUP MODELS OF THE SPENT BEAM AT THE OUTPUT OF THE REFOCUSING SECTION ($V_o$ = 16 kV)

| ENERGY GROUP j | | $\frac{V_j}{V_o}$ | $V_j$ (kV) | $r_j$ (in) | $r_j$ (cm) | $\left(\frac{dr}{dz}\right)_j$ | $\frac{I_j}{I_o}$ |
|---|---|---|---|---|---|---|---|
| 4 Energy-Group Model | 1 | .535 | 8.55 | .096 | .244 | - .07 | .219 |
| | 2 | .655 | 10.5 | .100 | .254 | - .04 | .344 |
| | 3 | .775 | 12.4 | .103 | .262 | - .01 | .250 |
| | 4 | 1.04 | 16.7 | .102 | .259 | + .03 | .187 |
| 5 Energy-Group Model | 1 | .53 | 8.5 | .095 | .241 | - .08 | .2 |
| | 2 | .615 | 9.8 | .099 | .252 | - .045 | .2 |
| | 3 | .705 | 11.3 | .103 | .262 | - .01 | .2 |
| | 4 | .78 | 12.5 | .103 | .262 | + .01 | .2 |
| | 5 | 1.085 | 17.4 | .102 | .259 | + .04 | .2 |

A current ray representation of an energy group, consisting of seven trajectories, is shown in Figure 15.

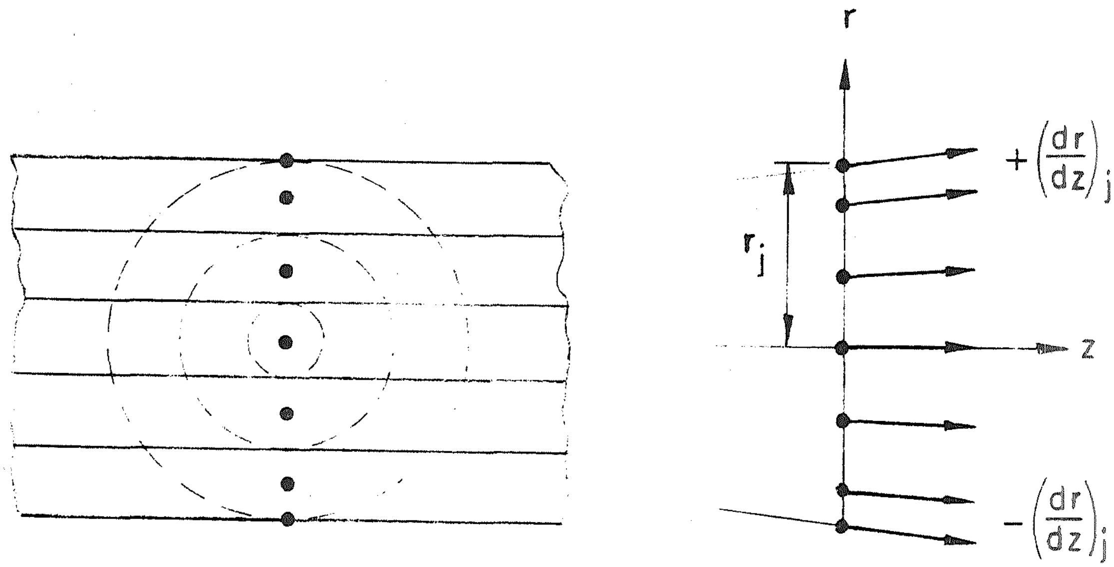


Figure 15 Ray model of an energy group.

The two extreme trajectories serve to define the beam contour for the group and carry no current. They are launched with slopes $\pm$ $(dr/dz)_j$ at a distance $r_j$ from the center of the beam to either side. The interior rays are launched with trajectory angles in proportion to the distance from the center of the beam. As will be discussed in the next subsection, the actual cylindrical beam is simulated in the trajectory calculation by a planar beam. The planar beam for each group is initially composed of five strips of equal width, as in Figure 15, with the current of each strip concentrated in the ray at its center.

All the energy groups, each with seven trajectories launched in the manner described, are included simultaneously in the collector trajectory calculation.

## COLLECTOR TRAJECTORY CALCULATION

The collector region was analyzed with a trajectory computer program in which the electron beam was represented by current rays distributed over the beam cross-section. A difficulty with the collector geometry under consideration was that it possessed neither planar nor cylindrical symmetry. A full three-dimensional computer program with space charge would therefore have been needed for a complete analysis of the collector. Since such a program was not available, the collector design was instead evaluated by computing the trajectories in the plane of reflection symmetry, assuming planar collector geometry.

The actual cylindrical beam thus had to be represented by a planar beam. If the space charge forces are strong, it is important to adjust the space charge in the planar beam so that the same beam spread is obtained as in the given cylindrical beam. Since a planar beam with the same width and current density as a cylindrical beam spreads more quickly than the cylindrical beam, a charge density reduction is needed. First, the initial current density in the planar beam is made half the current density in the cylindrical beam. This will give the identical initial electrostatic force tending to spread the beam in the two cases. During the subsequent spread, a further current density reduction in the planar beam, inversely proportional to the width, is necessary. The reason is that the cylindrical beam area increases in two dimensions, whereas the planar beam area increases only in one dimension; consequently, additional current density reduction is needed in the planar case to provide the same space charge force as in the cylindrical case.

The computer program had been modified to provide such a planar simulation of a cylindrical beam. In a test run with a beam expansion of three times the original width, the expanded beam size in the planar simulated case differed by less than one percent from the cylindrical beam. It has also been shown that the procedure is valid in a region with constant axial potential gradient.

Although the collector configuration does not possess planar symmetry, the potential distribution calculated in the plane of reflection symmetry, with the assumption of planar geometry, will be reasonably close to the actual distribution in the central collector region. This is because the voltages of the parallel electrodes were chosen so as to produce an approximately constant voltage gradient in the axial direction. Evidently, the shape of the holes in the electrodes, whether round or rectangular, will in this case not affect the field distribution, at least if the electrodes are thin. The calculated field distribution in the outer regions of the collector will be different from the actual distribution due to the presence of non-planar shields, but this is of little consequence as the main electron sorting takes place in the central region.

The trajectory computer program traces out the paths of the injected electrons in the potential distribution existing in the collector, including the transverse magnetic field in the deflection region. The measured deflection field, which was illustrated in Figure 9, is specified at individual mesh lines in the problem area as a function of axial distance. The field is assumed to be independent of position in both transverse directions; this is one of the approximations in the analysis.

Initially, the computer program solves the potential distribution in the problem area resulting from given voltages on the boundaries. The trajectories are computed through the potential distribution with the inclusion of the magnetic deflection field. The mutual force exerted by the beam electrons is not taken into account in this first calculation; it thus represents the behavior of a beam with negligible space charge.

An example of a computer-generated trajectory and equipotential plot in a two-stage depressed collector is shown in Figure 16. The collector scheme includes a magnetic deflection region in the small cavity at the beam entrance. A retarding field is produced by the two collector electrodes with voltages - 5.5 kV and - 10.3 kV, and by the end plate with a potential of - 19.2 kV. The potential gradient is approximately uniform in the central collector area in the original beam direction. Shields are attached to the electrodes to prevent the electrons from escaping to the grounded vacuum envelope which would actually surround the collector in the demountable apparatus. The shields distort the field at the sides but the main electron sorting takes place in the central region. The beam is composed of four groups with energies 8.55, 10.5, 12.4 and 16.7 kV respectively. The first two groups enter with converging trajectories from the refocusing region, the third group has almost parallel trajectories, and the fourth group is injected with diverging trajectories.

The no-space-charge trajectory plot demonstrates why this collector scheme appeared promising enough to warrant a detailed study. Evidently, with a suitable number and placement of collecting electrodes, a great deal of energy in the spent beam could be recovered. It is seen, for example, that nearly all the energy (about 98 percent) of the second group is recovered by the second electrode.

The effect of space charge is taken into account by the computer program through an iteration process. The currents associated with the trajectories in the first computation produce a charge distribution in the collector region, which is included in the potential calculation for the next iteration. Again the trajectories are traced out, producing a different space charge distribution for the third iteration, and so on. The process is continued until a self-consistent solution has been found. The result after seven iterations, usually sufficient to obtain self-consistency, is shown in Figure 17. The effect of the space charge in spreading the trajectories is considerable, even though the beam has already been expanded in area by a factor of ten in the refocusing section (the current density at the collector entrance is about 5 $A/cm^2$). The collector configuration, which looked promising for no space charge, is unsuitable when the space charge forces are included. Some of the trajectories return to ground potential because of insufficient deflection by the magnetic field. And some of the high energy electrons are deflected in the opposite direction because of a transverse electric field component established by the potential difference between the end plate and the shield on the second electrode.

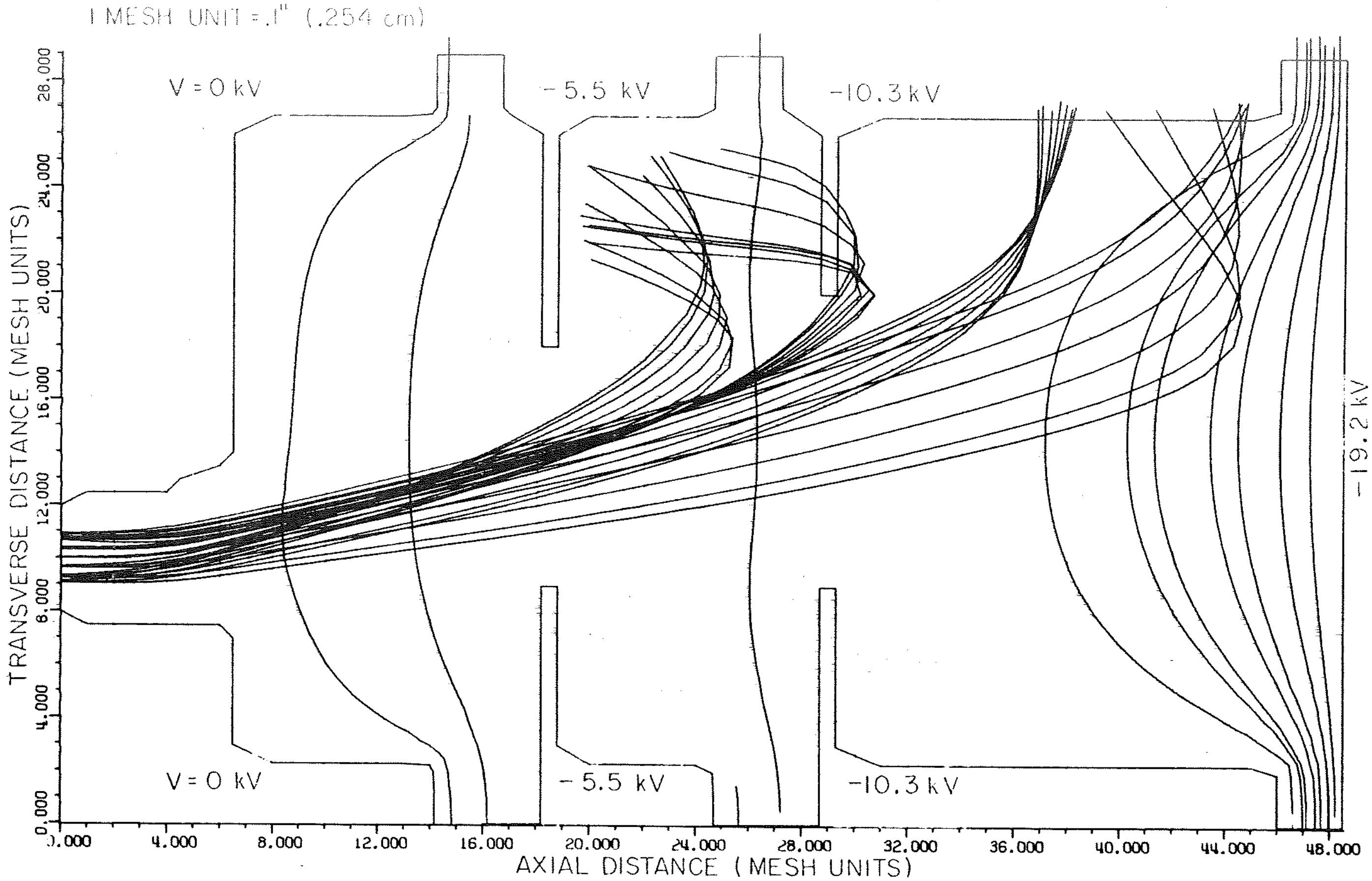


Figure 16 Calculated spent beam trajectories and equipotentials in a two-stage depressed collector in first iteration (without space charge).

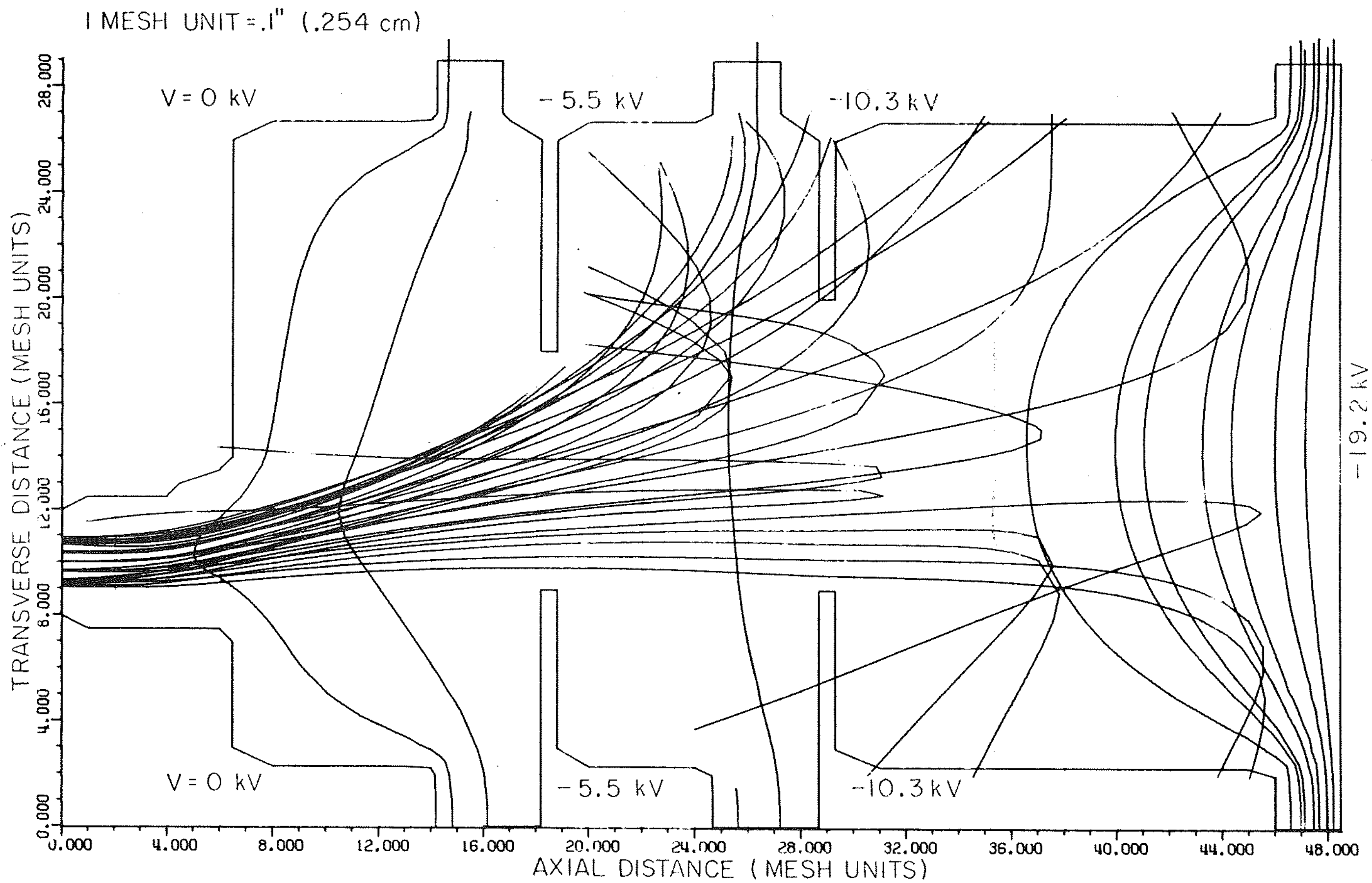


Figure 17 Calculated spent beam trajectories and equipotentials in last iteration (with space charge effects).

For an improved design, a larger deflection of the beam is needed. This may be achieved by having a stronger deflection field, in which case the electrodes also should be moved closer to the entrance. Or, additional electrostatic deflection force in the interior of the collector may be obtained by rearranging the shields.

## DESIGN ANALYSIS OF IMPROVED TWO-STAGE COLLECTORS

The initial attempt at improving the two-stage collector design was made by providing additional electrostatic deflection force beyond the first depressed electrode by rearranging the shields. Such a design is shown in Figure 18. Two shields on one side of the beam have been attached to the electrodes with the more depressed potential, producing a transverse electric field component which tends to deflect the electrons toward the opposite side. The spent beam in this case consists of five groups with the energies given in Table II.

An analysis of the performance of the collector indicated a collector efficiency of 56 percent. (The concept of collector efficiency, defined by the ratio of the power recovered by the collector to the power of the entering spent beam, is discussed in Appendix A). A general method of analyzing the collector performance from a trajectory plot in the plane of reflection symmetry is discussed, with an example, in Appendix E.

An investigation was made of the effect of various shield configurations in the region between the deflection field and the first electrode. The shields were moved closer to the beam, and were also attached to the depressed electrode, but without creating a transverse electrostatic field. It was found that the configuration of Figure 18, in which an approximately constant retarding field exists in the region, resulted in the best performance.

In the next step, the magnetic deflection field was replaced by an extended electrostatic deflection force throughout the region from the beam entrance hole in the refocusing magnet pole piece to the first electrode. Such a scheme is shown in Figure 19. The configuration of the first deflection control electrode was designed so that approximately the desired amount of deflection was obtained if its potential was the same as the potential of the first electrode. In practice, however, the voltage of the deflection electrode should be independently controlled. The estimated collector efficiency was 59 percent. It was thus somewhat better than the collector with initial magnetic deflection, even though the beam model and the voltages, as well as the location of the active electrodes, were the same in both cases.

The all-electrostatic collector also offers greater possibility for improvement, because the trajectories penetrate deeper into the collector. The third energy group, for example, turns around at the level of the second depressed electrode in the collector with the magnetic deflection, whereas

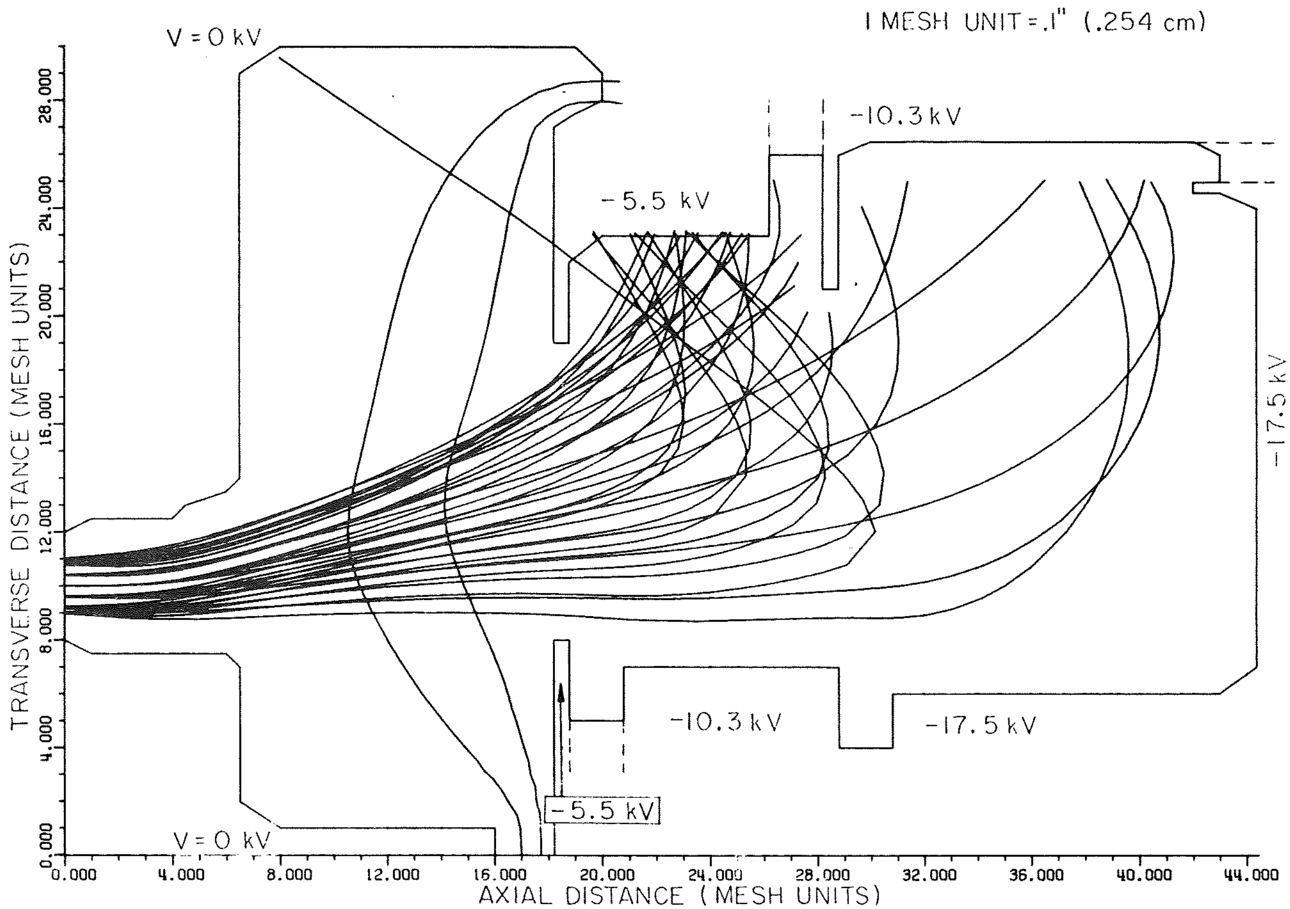


Figure 18 Two-stage depressed collector with initial magnetic deflection and transverse electrostatic deflection in the region beyond the first electrode.

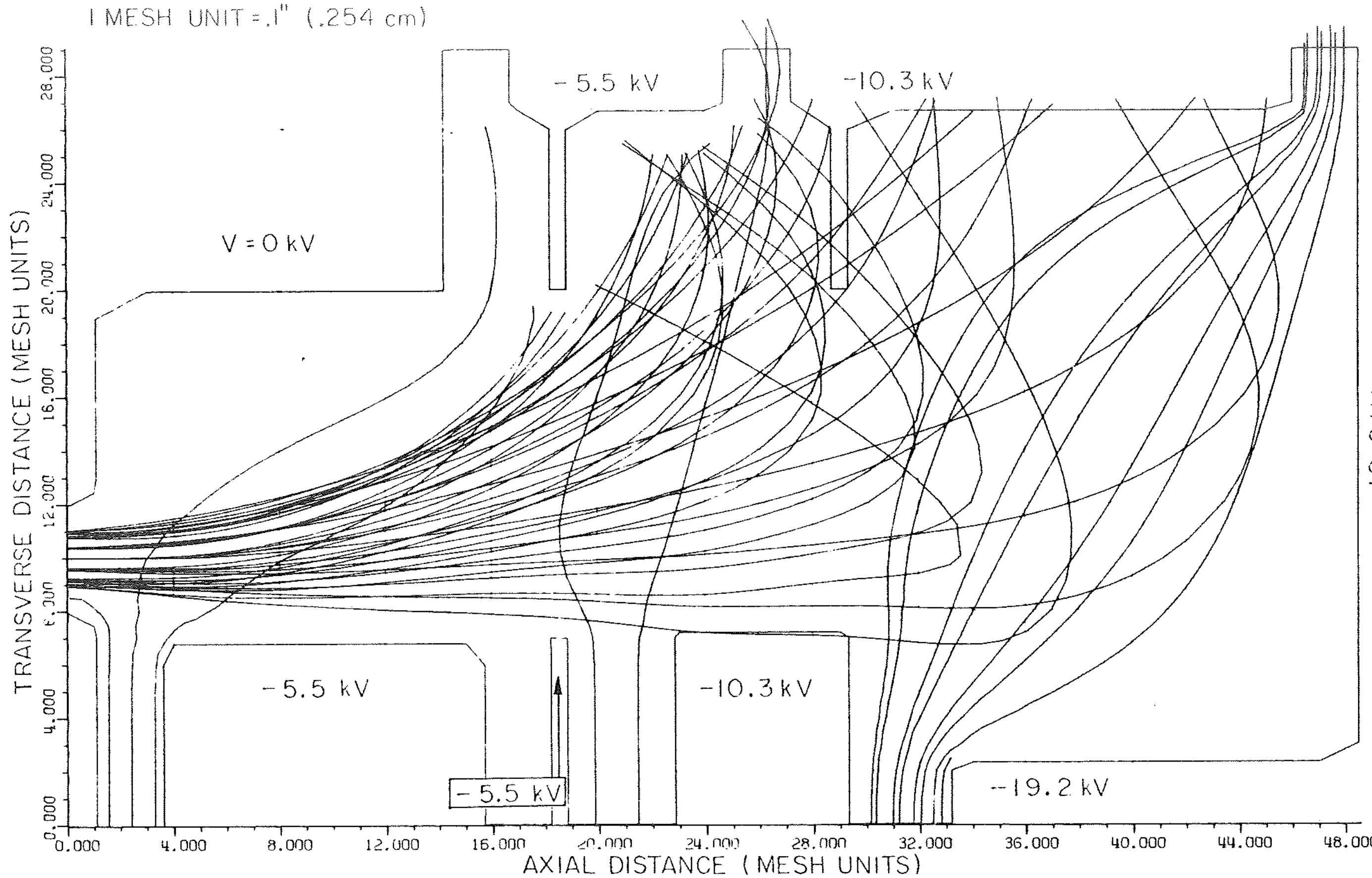


Figure 19 Two-stage depressed collector with electrostatic deflection.

it penetrates appreciably farther into the electrostatic collector. This is partly because of the greater spread in deflection as a function of electron energy, which is produced by the electric deflection field, resulting in smaller depression due to the space charge. (It can be shown that the deflection is inversely proportional to the electron velocity in the magnetic case, and inversely proportional to the square of the velocity in the electric case). A further advantage of the increased spread is that it is easier to add more stages to the collector. The collector scheme used for the final design of the multistage depressed collector, described in Section VIII, was therefore one with electrostatic deflection only.

## VI EVALUATION OF A TWO-STAGE TEST COLLECTOR

The objective of the study included the experimental evaluation and optimization of a two-stage collector for the purpose of comparing the methods of analysis with test results.

A collector was designed as an initial test vehicle, before the analysis methods had been developed, on the basis of estimated trajectories in the absence of space charge forces. The construction and assembly of the test collector was considered in Section IV. A trajectory plot for the configuration, with space charge effects included, is shown in Figure 20 for a five energy-group model of the spent beam. (The parameters of the beam model are listed in Table II.) An efficiency analysis of the collector trajectory plot, by a method which is described in detail in Appendix E, yielded an estimated collector efficiency of 48 percent. A trajectory calculation using a spent beam model with four energy groups gave an efficiency of 3.5 percentage points higher. It is believed that increasing the number of energy groups beyond five in the test collector analysis would not change the estimated efficiency by more than a few points.

Other computer runs with the four energy-group model were initially made in which the voltages of the first two electrodes were varied by 1 - 2 kV. The geometry of these runs differed only by a greater distance between the second electrode and the end plate, which was depressed beyond the cathode voltage of -16 kV. On the basis of these runs, the estimated optimum voltages of the test collector, with the end plate at cathode potential and a reduced distance between the second electrode and the end plate, are the values shown in Figure 20.

### PERFORMANCE OF THE TWO-STAGE TEST COLLECTOR

Two experiments were made on the two-stage test collector in the demountable apparatus. In the first experiment, extensive collector depression data were taken, even though the beam transmission was not very good. In the second experiment it was verified that significant improvement in the beam transmission into the collector could be obtained. This would, however, require enlarging the aperture in the deflection magnet shield, which had not been done for the second experiment. The data from the first experiment were generally used for a detailed analysis of the collector performance.

The operating characteristics of the traveling-wave tube, which was employed to evaluate the two-stage test collector in the demountable apparatus in the two experiments, are listed in Table III. The predicted RF performance given in this table was calculated with the two-dimensional program, without RF space charge effects and with no circuit losses, since this program was used for the refocusing analysis. Satisfactory agreement with measured values was obtained for the saturated output power and the gain.

In the first experiment the beam transmission was relatively poor for both the DC beam (95 percent) and the RF modulated beam (79 percent). The

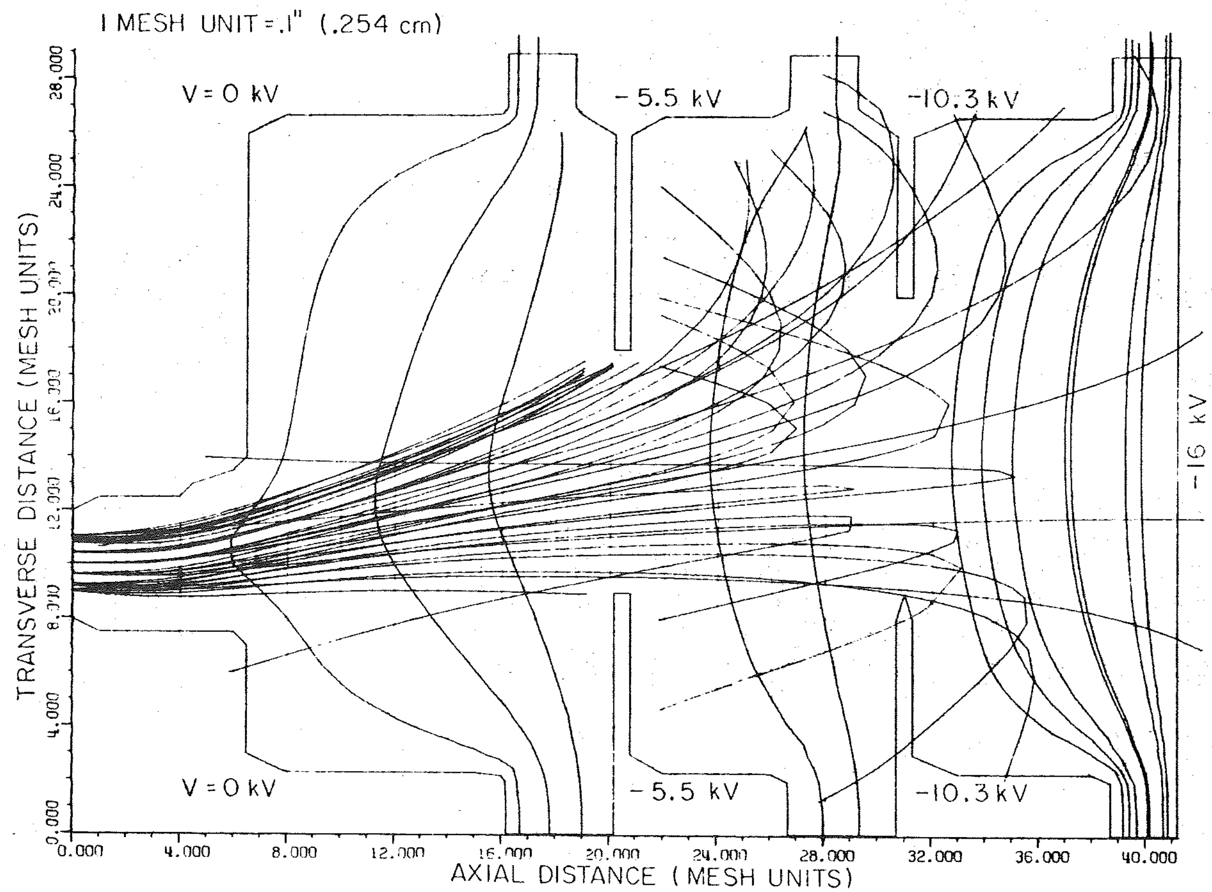


Figure 20 Calculated spent beam trajectories and equipotentials in two-stage test collector.

transmission was defined by the sum of the fractional currents going to the refocusing magnet pole piece (upon which the deflection magnet was mounted), the deflection magnet shield, and the collector electrodes. The measurements were made with undepressed collector to minimize the current escaping to the grounded vacuum envelope from unshielded portions of the collector. The transmission current would thus be very nearly equal to the current passing through the pole piece of the main solenoid.

TABLE III. TRAVELING-WAVE TUBE CHARACTERISTICS

| PARAMETER | ASSUMED OR CALCULATED VALUE | MEASURED VALUE | |
|---|---|---|---|
| | | 1st EXPERIMENT | 2nd EXPERIMENT (IMPROVED FOCUSING) |
| Beam voltage (kV) | 16 | 16 | 16 |
| Beam current (A) | .932 | .870 | .870 |
| Perveance (μperv) | .46 | .43 | .43 |
| Frequency (GHz) | 8.95 | 8.95 | 8.95 |
| Output power (kW) | 4.17 | 3.94 | 3.68 |
| Basic efficiency (%) | 28 | 28.3 | 26.5 |
| Gain (dB) | 14.5 | 15.3 | 15.5 |
| Cold loss (dB) | 0 | 2.1 | 2.1 |
| Beam transmission (%): | | | |
| DC | 100 | 94.9 | 97.7 |
| RF | 100 | 77.0 | 88.4 |

Notes:

(a) The transmission refers to current passing through the pole piece of the main solenoid.

(b) Current intercepted on RF circuit in 2nd experiment was about 1 mA.

The objective of the second experiment was to achieve an improved beam transmission. It is seen from Figure 12 that the beam passing through the pole piece of the main magnet gets fairly close to intercepting. The hole diameter in the pole piece insert was therefore increased from .125" (.317 cm) to .150" (.381 cm). The movable pole piece, with the collector assembly, was also made reentrant to achieve a peaking of the field toward the output of the traveling-wave tube. In addition, the RF circuit was isolated, making it possible to measure the current intercepted thereon separately. The following changes in performance were observed as a result of these modifications:

(1) Beam transmission beyond the movable pole piece improved from 94.9 percent to 97.6 percent without RF drive and from 77.0 percent to 88.4 percent with RF drive.

(2) The decrease in interception (body current) was accompanied by a corresponding increase in the deflection magnet shield current; no significant change was noted in the current going to the refocusing magnet pole piece. The current entering the effective collector region was therefore about the same as before, but it could evidently be increased by enlarging the aperture in the deflection magnet shield. The current distribution to the first and second electrodes and the end plate, with RF and no depression, was very similar to the distribution observed in the first experiment. The collector performance would thus also be quite similar to the performance in the first experiment. (The actual measured currents with RF drive and no depression have been listed in Table IV, which will be discussed shortly.)

(3) Interception on the coupled cavity circuit both with and without RF drive was very small, estimated to be about 1 mA or .1 percent. Hence practically all the interception occurred on the pole piece.

(4) The saturated RF output power decreased from 3.94 kW to 3.68 kW. This is a result of the field peaking, which keeps the beam constrained to a smaller radius toward the output, and therefore reduces the effectiveness of the interaction between the beam and the circuit wave. Since no increase in the circuit interception current was observed with RF drive, the amount of peaking, about 20 percent, was likely to be larger than necessary.

It was concluded from the results of the second experiment that a significant improvement in the beam transmission into the effective collector region could be attained by appropriate modifications of the magnetic shield and pole piece apertures. Although no further experiments were actually made, the changes which were planned for the final four-stage collector evaluation are described in Section VIII.

The RF performance of the two-stage test collector is summarized in Table IV. The predicted performance is compared with three measured cases: the end plate voltage optimized, held at cathode potential, and connected to the second electrode. The last two are of interest from a system point of view, since one less voltage supply is needed. In each case, the electrode voltages, as well as the refocusing and deflection magnet currents, were optimized for maximum overall efficiency. Since the assumed and measured total beam currents were somewhat different, the current distribution has been expressed with fractional values. For completeness, the current distributions without depression in the two experiments are also included.

TABLE IV. RF PERFORMANCE OF TWO-STAGE TEST COLLECTOR

| CASE | OPTIMIZED COLLECTOR | | | | UNDEPRESSED COLLECTOR | |
|---|---|---|---|---|---|---|
| | CALCULATED | MEASURED, WITH POTENTIAL OF END PLATE | | | | |
| | | OPTIMIZED | AT CATHODE POTENTIAL | AT POTENTIAL OF 2nd STAGE | 1st EXP. | 2nd EXP. |
| $V_o$ (kV) | 16.0 | 16.0 | 16.0 | 16.0 | 16.0 | 16.0 |
| $I_o$ (A) | .932 | .870 | .870 | .870 | .870 | .864 |
| $V_{c1}$ (kV) | -5.5 | -5.12 | -5.12 | -5.12 | 0 | 0 |
| $V_{c2}$ (kV) | -10.3 | -9.55 | -9.55 | -10.38 | 0 | 0 |
| $V_{c3}$ (kV) | -16.0 | -14.6 | -16.0 | -10.38 | 0 | 0 |
| $I_B/I_o$ | 0 | .312 | .309 | .338 | .230 | .117 |
| $I_{DM}/I_o$ | 0 | .031 | .031 | .037 | .017 | .022 |
| $I_S/I_o$ | .1 | .195 | .191 | .205 | .029 | .151 |
| $I_{c1}/I_o$ | .72 | .276 | .284 | .264 | .136 | .133 |
| $I_{c2}/I_o$ | .18 | .155 | .168 | .022 | .178 | .217 |
| $I_{c3}/I_o$ | 0 | .031 | .017 | .135 | .410 | .361 |
| $P_c$ (kW) | 5.40 | 2.91 | 2.89 | 2.59 | - | - |
| $P_b$ (kW) | 11.1 | 7.82 | 7.82 | 7.82 | - | - |
| $\eta_c$ (%) | 48.8 | 37.2 | 37.0 | 33.2 | - | - |

NOTES:

(a) The current and voltage symbols are defined in Figure 10.

(b) In the depressed collector measurements, the main solenoid field was 1870 gauss (.187T); the refocusing field was 790 gauss (.079T), or 43 percent of the main field.

The following observations are made:

(1) The measured optimum collector electrode voltages were within 10 percent of the estimated values. This is encouraging but of somewhat unclear significance, since the measured and expected current distributions agreed only in part.

(2) The current to the end plate, $I_{c3}$, was non-zero even though the end plate was more depressed than the second electrode. The effective secondary emission coefficient was thus less than unity.

(3) The sum of the currents to the second electrode and the end plate was slightly larger than, but very close to, the predicted value. (Because not all the electrons impinging on the end plate produced secondary electrons which were collected at a less depressed potential, as was assumed in the analysis, an appropriate comparison to make is for the sum of the currents to the end plate and the second electrode.) Possible reasons why the measured value was somewhat larger are that the experimental potential of the second electrode was less depressed (-9.55 kV) than the value used in the analysis (-10.3 kV), and that the effective secondary emission coefficient was smaller than assumed; thus, some of the electrons striking the gun-side of the second electrode were also effectively collected there.

On the whole, however, the behavior of the high energy electrons agrees very well with predictions. This indicates that these electrons have been adequately represented by the high energy groups in the trajectory model of the beam entering the collector.

(4) The current to the first electrode is considerably smaller than predicted. As a consequence, the current going to ground potential is significantly larger. This discrepancy is discussed more fully in the next subsection.

(5) The collector efficiency, $\eta_c$, defined by the ratio of the recovered power, $P_c$, to the power in the incident spent beam, $P_b$, was only two-thirds of the estimated value, as a result of the large body current.

In calculating the collector efficiency, the power recovered by the collector is directly computed from measured values. The power in the spent beam entering the collector, $P_b$, is obtained from the energy balance condition

$$P_b = I_o V_o + P_{RF\ in} - P_{RF\ out} - P_{interception} - P_{circuit\ loss}$$

The first three terms on the right-hand side (the DC beam power and the RF input and output power) are measured quantities. The power intercepted on the RF circuit and the pole piece of the main solenoid was estimated by using the current interception value for no depression, 23 percent or 200 mA. (The body current with depression is larger because of electrons escaping to the vacuum envelope from unshielded portions of the collector, and because of possible returning electrons.) The energy of the intercepted electrons is not generally known. For simplicity it was assumed that the interception current consisted of the lowest energy electrons, since the slow electron trajectories tend to have larger radial oscillations than the fast ones. From the spent beam energy distribution curve in Figure 13, it is found that the average energy of these electrons corresponds to .53 times the DC energy. This gives an intercepted power of 1.70 kW. The power lost by dissipation in the circuit and RF leakage from the stacked assembly was calculated by assuming that the cold loss (2.1 dB) was uniformly distributed over the length of the circuit:

$$P_{\text{circuit loss}} = \int 2\,\alpha\, P_{RF}(z)\, dz,$$

$$\text{where} \quad \alpha = \frac{\text{loss (dB/unit length)}}{20 \log_{10} e} \quad \text{per unit length.}$$

This may be expressed in the form

$$P_{\text{circuit loss}} = .230 \quad L(\text{dB}) \left\langle P_{RF} \right\rangle_{\text{circuit}},$$

where L is the total cold loss in the circuit in dB and $\langle P_{RF} \rangle_{\text{circuit}}$ is the average power level in the circuit. The power distribution $P_{RF}(z)$ was obtained from the computer print-out and the integration performed numerically. The resulting circuit loss was .58 kW. The kinetic power of the spent beam entering the collector (more precisely the refocusing region) was then found to be 7.82 kW. With a recovered power of 2.91 kW the collector efficiency was 37.2 percent. The estimate is on the low side since part of the intercepted current consists of electrons with higher energies.

(6) The recovered power changed by less than one percent if the end plate was held at cathode potential (-16 kV) rather than the optimum value of -14.6 kV. With the end plate and the second electrode connected to the same voltage supply, the maximum power recovered by the collector decreased by about ten percent. Reducing the number of independent voltage supplies, by making use of the cathode voltage, appears well worthwhile in the

present collector. This is not necessarily true for other types of collectors, however, or even for an optimized geometry of the same general configuration.

The power recovered by the collector was fairly insensitive to deviations in the collector electrode voltages. A change of $\pm$ .5 kV in the first and second electrode voltages reduced the recovered power by less than 1.5%. The end plate voltage could be changed by $\pm$ 1 kV for less than a 1% reduction in recovered power. Also, no significant variation in collector performance was observed if the refocusing and deflection magnet currents were changed by 5%.

(7) The magnitude of the refocusing field, 43 percent of the main solenoid field, was in good agreement with the value derived in the analysis (40 percent), particularly since the experimental refocusing field was somewhat peaked.

As has been mentioned, the test collector was not an optimized design. The basic RF converion efficiency of the tube was raised by the collector from 28.3 percent to 35.8 percent. This degree of efficiency enhancement is possible with a single stage conventional depressed collector. The predicted overall efficiency, with no circuit losses, was 43.3 percent. If the circuit losses and the loss due to interception on the pole piece are included, the predicted efficiency would be 39.0 percent.

## DISCUSSION OF APPROXIMATIONS AND SOURCES OF ERROR

The main discrepancy between the predicted and measured performance of the two-stage test collector was the current going to the first electrode. It was found to be 28 percent of the total beam current instead of the estimated 72 percent. A comparison could also be made by referencing the electrode currents relative to the total current actually entering the main collector region, since in the analysis all the spent beam was assumed to pass through the aperture of the deflection magnet shield. With undepressed collector, 72 percent of the RF modulated beam is collected on the two electrodes and the end plate; with depression, 38 percent of this current goes to the first electrode. This is still only a little more than one-half of the predicted amount, even though the composition of the experimental beam entering the collector should now be more favorable than was assumed in the analysis.

Some of the possible factors contributing to the observed discrepancy are the following:

(1) Residual angular velocity in the expanded spent beam, as a result of non-zero magnetic cathode flux.

(2) Magnetic and electric fringing fields, particularly at the output of the deflection region; non-uniform magnetic field over the beam cross-section in the deflection region; refocusing field leakage into the deflection region; an axial leakage field in the collector region (this is further discussed at the end of Section VII).

(3) Electrons escaping from the depressed region to the vacuum envelope by imperfect shielding.

(4) Uncertainty in the analytical derivation of the trajectory launching conditions of the low and medium energy electrons into the collector, caused by:

i) The neglect of space charge forces due to RF beam bunching in the two-dimensional program.

ii) The assumption of uniform axial magnetic field over the beam area.

iii) The continuous interaction model of the two-dimensional program, used to represent the beam-circuit wave interaction in the coupled cavity structure.

Some information about the effect of these sources of error can be obtained from considering the collector performance under DC conditions. The uncertainty in trajectory launching conditions is then minimized, although it is still present to a degree because of beam scalloping and thermal velocity components. The current distributions recorded for some operating conditions of the collector with a 16 kV DC beam are shown in Table V. An undepressed collector intercepts approximately 70 percent of the current on the end plate, 20 percent on the second electrode, and 4 percent on the first electrode. According to analysis, it should be possible to direct the whole beam to the end plate. Only items (1) and (2) in the list (angular velocity and field irregularities) should be significant in this case.

A measure of item (3), electrons escaping to the vacuum envelope, is found by a comparison between cases II and IV in Table V. They differ principally by the voltage of the end plate, which in case IV was the same as the voltage of the second electrode, -9.9 kV, and in case II was at the cathode voltage. Because the voltages of electrodes 1 and 2 are nearly the same in the two cases, the same amount of current is entering through the aperture of the second electrode. In case IV, all these electrons impinge on the end plate and are generally collected there. In case II, practically all the electrons are reflected back from the end plate. Most of these electrons are collected on the second electrode; some stream back through the aperture and are intercepted on the first electrode or the deflection magnet shield, both of which therefore register an increase in current. But in addition, some of the current which in case IV went to the

TABLE V DC PERFORMANCE OF TWO-STAGE TEST COLLECTOR

| CASE | MEASURED COLLECTOR* | | | |
|---|---|---|---|---|
| | 1st EXPERIMENT | | 2nd EXPERIMENT | |
| | I | II | III | IV |
| $V_o$ (kV) | 16.0 | 16.0 | 16.0 | 16.0 |
| $I_o$ (kV) | .870 | .865 | .865 | .878 |
| $V_{c1}$ (kV) | 0 | -5.75 | 0 | -6.16 |
| $V_{c2}$ (kV) | 0 | -9.9 | 0 | -9.9 |
| $V_{c3}$ (kV) | 0 | -16.0 | 0 | -9.9 |
| $I_B/I_o$ | .051 | .183 | .024 | .100 |
| $I_{DM}/I_o$ | .009 | .008 | .014 | .011 |
| $I_S/I_o$ | .009 | .041 | .015 | .032 |
| $I_{c1}/I_o$ | .042 | .112 | .042 | .088 |
| $I_{c2}/I_o$ | .222 | .656 | .191 | .182 |
| $I_{c3}/I_o$ | .667 | 0 | .714 | .587 |

* The current and voltage symbols are defined in Figure 10.

end plate now escapes to the vacuum envelope through the gap between the end plate and the shield on the second electrode, causing the observed rise in the body current (83 percent).

For an RF modulated beam, the number of electrons escaping between the second electrode and the end plate will be relatively small, because of the reduced number of high energy electrons. A more significant number may escape between the first and second electrodes, however, particularly since the secondary electron generation at the second electrode is likely to be large as a result of grazing trajectories, as may be seen from Figure 20.

The greatest uncertainty in the collector analysis for an RF beam was in the derivation of the trajectory entrance conditions. An indication of the discrepancy between measured and calculated initial trajectory angles was provided by the current distribution in the undepressed collector, listed in Table IV. The measured currents, in the first experiment, recorded at the end plate, second and first electrodes were 41 percent, 18 percent and 14 percent respectively. Much the same distribution was observed in the experiment with improved focusing. According to analysis, 80 percent of the current should go to the end plate and the rest to the second electrode. Part of the discrepancy is due to the angular velocity component present in the beam and the field irregularities, which are not accounted for, just as in the DC case. But, in addition, approximations were made in the computation of the trajectory launching conditions with the two-dimensional large signal computer program, notably the neglect of space charge forces due to RF beam bunching. This was considered sufficiently important to be further investigated. The results are discussed in the next section.

Another approximation in the analysis was that the disk model of the beam is based on laminar flow with the axial field assumed to be uniform over the area of the beam. The spherical aberration effect of a changing magnetic field, particularly in the transition between the main solenoid field and the refocusing field, was thus neglected.

Finally, a truly satisfactory calculation should utilize the exact field distribution in the RF interaction gaps of the coupled cavity structure. The continuous electron beam-RF circuit wave interaction model, which is used in the two-dimensional large signal computer program, has generally been satisfactory for calculation of overall performance parameters, such as efficiency. The reason is that in a Fourier analysis of the RF wave, only one space harmonic remains approximately in phase with the electron velocity over an extended distance. The other space harmonics appear to be rapidly oscillating to the electrons and consequently contribute little to the average motion. For calculating the detailed motion of the electrons, however, it may well be necessary to take into account the complete RF field configuration in the last few cavities. It is thus believed, for example, that a calculation which includes the actual gap fields would predict some current interception on the output pole piece. This is not predicted with the continuous wave interaction fields, even in the presence of initial beam scalloping and RF space charge forces, although the trajectories get quite close to the pole piece.

# VII. CORRECTIONS TO INITIAL ANALYSIS PROCEDURE

The performance of the two-stage test collector indicated that the low and medium energy electrons did not behave as expected. This might, at least partially, be attributed to the omission of space charge forces due to RF beam bunching in the derivation of the launching conditions into the collector. These forces would be expected to affect the lower energy electrons most, and might produce a greater divergence of the trajectories at the end of the refocusing section. Such trajectories would result in reduced predicted current to the first depressed stage, which would be in better agreement with the test results. An analysis with RF space charge effects included was thus considered very desirable. Consequently, work on the collector study contract was suspended, for five months, until the space charge forces were incorporated into the two-dimensional computer program, as a result of a requirement in a parallel contract.

## EFFECT OF RF SPACE CHARGE FORCES

The spent beam energy distribution calculated with RF space charge effects is shown in Figure 21, both at saturation and at the end of the refocusing section. For comparison, the distribution obtained without the bunching forces is also displayed; it remains unchanged throughout the drift region beyond saturation. At the end of the refocusing section, the spent beam energy distribution calculated with RF space charge forces differs mostly by somewhat lower disk energies than in the distribution obtained without these forces. Otherwise, the shape of the two curves is similar. At saturation, the distribution with the space charge effects included is appreciably more bunched in energy and resembles quite closely the spent beam distribution calculated with the one-dimensional program (Figure 38 in Appendix C). Thus, during the drift through the refocusing section, the spent beam acquires a greater axial velocity spread. Generally, this reduces the collector efficiency.

The disk trajectories from saturation through the refocusing section, calculated with RF space charge forces, are displayed in Figure 22. Comparing the trajectory plot with Figure 12, it is seen that the effect of the space charge forces is to produce a less uniform beam with a larger variation in disk radii and trajectory slopes. There is also a somewhat greater trend for convergence of the slow electrons at the end of the refocusing section.

The composition of the spent beam at the output of the refocusing section is summarized by the graphs in Figure 23. The aforementioned effects are readily apparent in a comparison of the histograms in Figure 23 and Figure 13. A numerical analysis of the two cases is found in Table VI, which lists the parameters of a five energy-group model of the spent beam at the output of the refocusing section. Also included in the table are the parameter variations from the average values for each group.

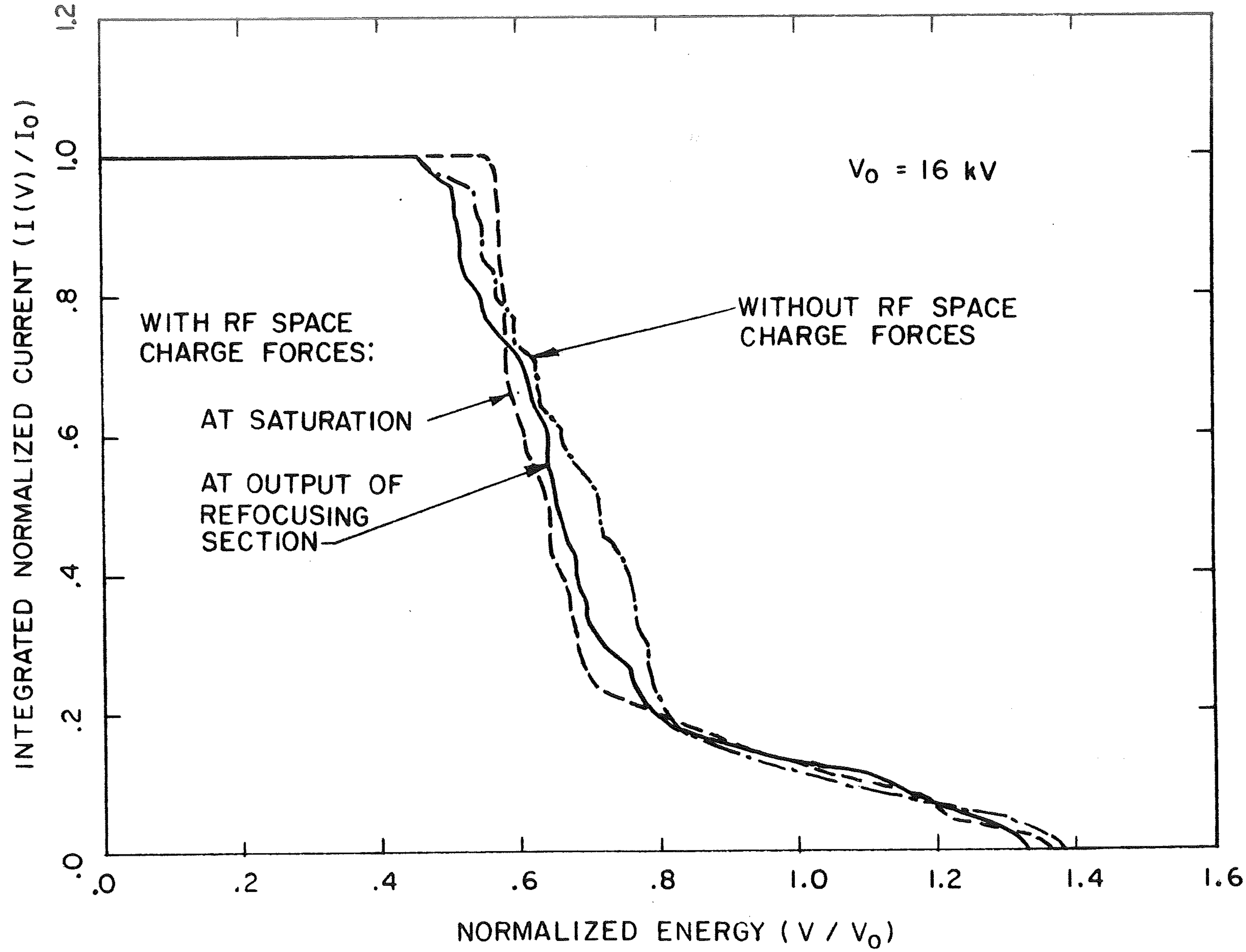


Figure 21 Spent beam energy distributions calculated with and without RF space charge forces.

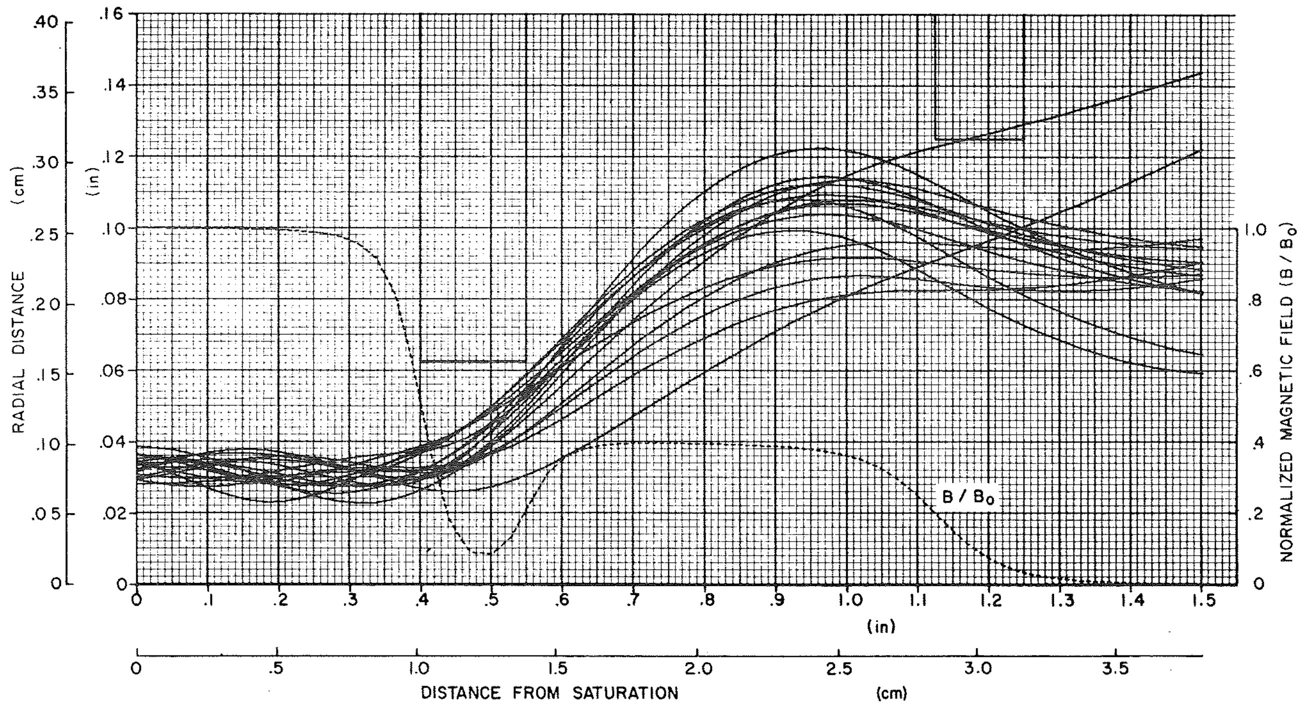


Figure 22 Disk edge trajectories in refocusing section calculated with RF space charge forces.

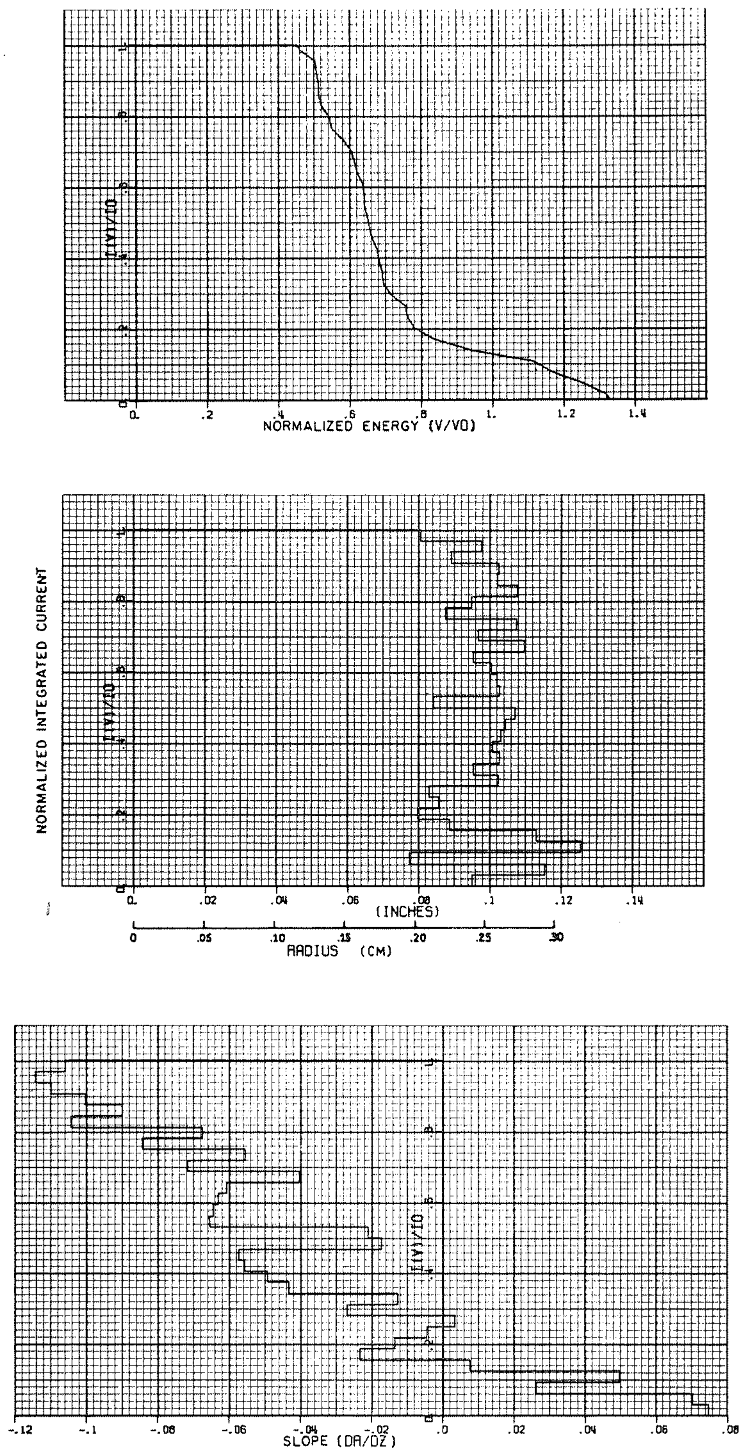


Figure 23  Spent beam composition at output of refocusing section calculated with RF space charge forces.

TABLE VI FIVE ENERGY-GROUP MODEL AT OUTPUT OF REFOCUSING REGION, DERIVED WITH AND WITHOUT RF SPACE CHARGE FORCES.

| RF SPACE CHARGE FORCES | ENERGY GROUP j | $V_j$ (kV) | $r_j$ (in) | $r_j$ (cm) | $\left(\frac{dr}{dz}\right)_j$ |
|---|---|---|---|---|---|
| No | 1 | 8.5 | .095 $^{+.003}_{-.012}$ | .241 $^{+.008}_{-.030}$ | -.08 $^{+.020}_{-.025}$ |
| | 2 | 9.8 | .099 $^{+.002}_{-.003}$ | .252 $^{+.005}_{-.008}$ | -.045 $^{+.017}_{-.022}$ |
| | 3 | 11.3 | .102 $^{+.001}_{-.001}$ | .259 $^{+.003}_{-.003}$ | -.01 $^{+.007}_{-.011}$ |
| | 4 | 12.5 | .103 $^{+.001}_{-.002}$ | .262 $^{+.001}_{-.005}$ | +.01 $^{+.013}_{-.008}$ |
| | 5 | 17.4 | .102 $^{+.002}_{-.003}$ | .259 $^{+.005}_{-.008}$ | +.04 $^{+.029}_{-.019}$ |
| Yes | 1 | 8.1 | .094 $^{+.014}_{-.012}$ | .239 $^{+.036}_{-.030}$ | -.10 $^{+.010}_{-.014}$ |
| | 2 | 9.5 | .099 $^{+.011}_{-.012}$ | .252 $^{+.028}_{-.030}$ | -.063 $^{+.023}_{-.021}$ |
| | 3 | 10.5 | .101 $^{+.006}_{-.017}$ | .257 $^{+.015}_{-.043}$ | -.047 $^{+.030}_{-.018}$ |
| | 4 | 11.6 | .093 $^{+.010}_{-.010}$ | .236 $^{+.025}_{-.025}$ | -.034 $^{+.027}_{-.033}$ |
| | 5 | 17.6 | .102 $^{+.023}_{-.025}$ | .259 $^{+.058}_{-.063}$ | -.03 $^{+.045}_{-.053}$ |

NOTES:

(a) Equal current distribution among the groups

(b) Radii and trajectory slopes are averages and maximum deviations from the average value.

The calculations with RF space charge forces thus indicate that, generally, the slow electrons converge more than originally estimated. It should be noted that this has the effect of producing trajectories which diverge more strongly some distance into the collector, as a result of both the space charge forces and the angular motion due to non-zero cathode flux. This may be seen from Figure 24, in which trajectory I with initially zero slope is compared with trajectories II and III with initial slopes of $\pm \alpha$; if the origin of trajectory II is displaced from 0 to 0', it will coincide with trajectory III. Or, it may be said that a beam with converging trajectories which after some distance become parallel, behaves like a beam with initially a smaller radius.

APPROXIMATE CORRECTION FOR ANGULAR VELOCITY

In the trajectory analysis of the asymmetric collector, it was not possible to directly account for the beam spreading effect of the residual angular velocity, since this would require a full three-dimensional computer program. A method of correcting for this effect, even though approximate, would be of value. One way of doing this is shown in Figure 25. It consists in finding the launching angle ($\alpha_e$) of an equivalent trajectory without angular velocity, which in the presence of space charge forces and electric retarding fields is deflected radially the same amount as a trajectory with the proper amount of angular velocity. The axial position of the reference plance would typically be at the location of the collecting electrode for a particular energy group.

A quantitative investigation of this effect was carried out with the trajectory computer program in the following way. The five energy groups of the spent beam model, with their average radii and trajectory slopes as calculated with RF space charge forces, were launched into a cylindrically symmetric version of the two-stage test collector. (Such a collector would be obtained by switching off the magnetic deflection field and shifting the collector electrode apertures to a coaxial position.) The magnetic focusing field was assumed to be zero everywhere, but the angular velocity due to non-zero cathode flux, which would be present in a field-free region, was included. Additional test trajectories with zero angular velocity were launched with each energy group for the purpose of finding the equivalent trajectory slope. The electrode potentials of the cylindrically symmetric two-stage collector were the same as the experimental potentials in the test collector. The results are listed in Table VII, and show that most of the converging rays should be replaced by diverging trajectories. Also shown in Table VII are the slopes of a strongly diverging beam model, constructed by changing the sign of the negative trajectory slopes in the model derived with RF space charge forces, as a measure of the degree of variation in angle which is possible.

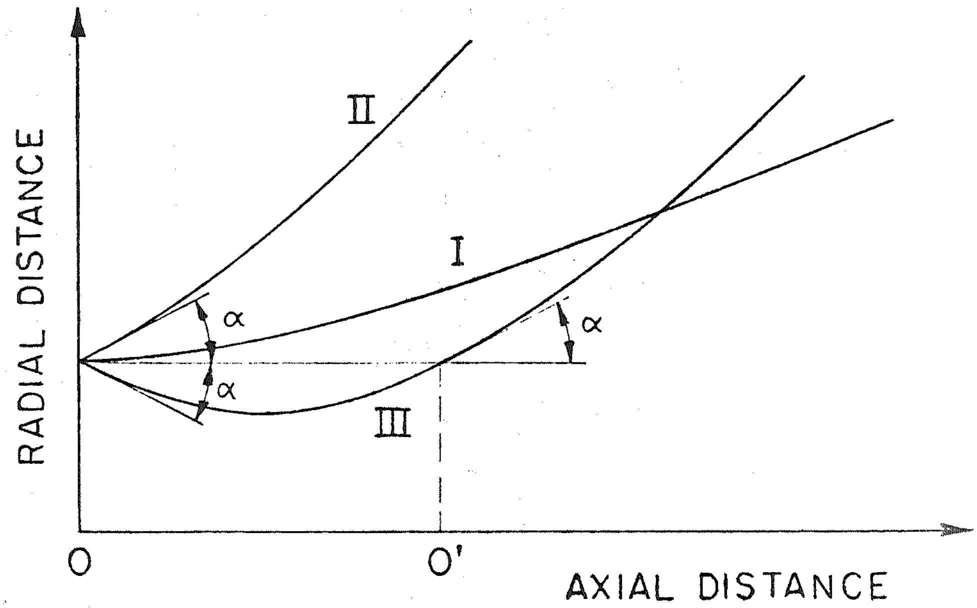


Figure 24 Effect of non-zero initial slope on trajectories with angular velocity in a region with no magnetic field.

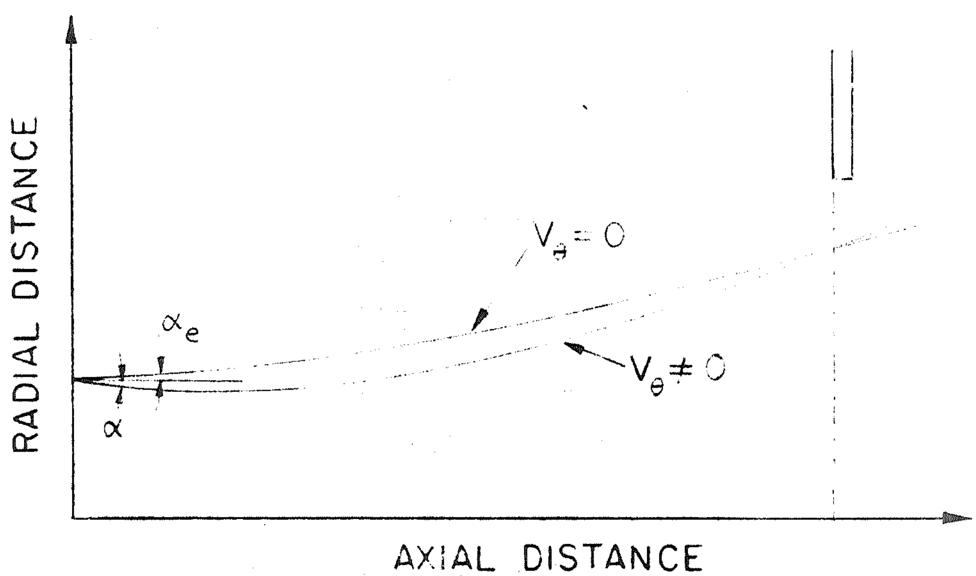


Figure 25 Radial spread of edge trajectory with angular velocity and of equivalent trajectory without angular velocity.

TABLE VII TRAJECTORY SLOPES OF CORRECTED AND STRONGLY DIVERGING BEAM MODELS

| | | Tan $\alpha_j = (dr/dz)_j$ | | |
|---|---|---|---|---|
| ENERGY GROUP j | $V_j$ (kV) | MODEL WITH RF SPACE CHARGE | EQUIVALENT RAY WITHOUT ANGULAR VELOCITY | MODEL WITH STRONGLY DIVERGING BEAM |
| 1 | 8.1 | -.10 | .01 | .10 |
| 2 | 9.5 | -.063 | -.015 | .063 |
| 3 | 10.5 | -.047 | .0 | .047 |
| 4 | 11.6 | -.024 | .018 | .024 |
| 5 | 17.6 | +.03 | .045 | .045 |

An analysis of the test collector, using the trajectory launching conditions corrected for the effect of angular velocity, was made with the end plate at the cathode voltage and the other two electrode voltages at the experimentally optimized values. A correction was also made for the energy removed from the spent beam due to circuit losses. The kinetic power in the beam emerging from the output coupler, given by

$$P_b = P_o + P_{RF\ in} - P_{RF\ out} - P_{circuit\ loss},$$

was then found to be 9.52 kW. This is equivalent to an average normalized energy of $\bar{V}/V_o = .683$, rather than the value of .714 in the computer-calculated spent beam. The first four energy groups were accordingly reduced in energy by about 5% and the highest energy group by 1%. (The dissipated RF energy is principally supplied by the low energy electrons.)

The estimated current distribution is shown in Table VIII, the next to the last column. The corresponding experimental values are also displayed, in a way which more explicitly demonstrates the effect of collector depression. The measured total currents going to the body, the deflection magnet (and refocusing magnet pole piece), and the deflection magnet shield have been separated into two parts, namely, the measured currents without depression and a remainder; the remainder thus reflects the effect of depression. The calculated current going to ground potential (15%) essentially comprises the sum of the currents to the deflection magnet and the shield as a result of depression, $(\Delta I_{DM} + \Delta I_S)/I_o$. Practically all the change in body current due to depression is from electrons escaping to the vacuum envelope because of imperfect shielding, principally from the region between the first and second electrodes.

TABLE VIII CORRECTED ANALYSIS OF RF PERFORMANCE OF TWO-STAGE TEST COLLECTOR WITH DEPRESSION.

| CASE | MEASURED | PERFORMANCE ESTIMATED FROM | | | |
|---|---|---|---|---|---|
| | | MEASURED VALUES ASSUMING | | TRAJECTORY ANALYSIS WITH | |
| | | 100 PERCENT TRANSMISSION | 100 PERCENT TRANSMISSION PERFECT SHIELDING | CORRECTED BEAM MODEL | DIVERGING BEAM MODEL |
| $I_{Bo}/I_o$ | .230 | .0 | .0 | .0 | .0 |
| $\Delta I_B/I_o$ | .079 | .120 | .0 | .0 | .0 |
| $I_{DMo}/I_o$ | .017 | .0 | .0 | .0 | .0 |
| $\Delta I_{DM}/I_o$ | .014 | .021 | .021 | ≈.0 | ≈.0 |
| $I_{So}/I_o$ | .029 | .0 | .0 | .0 | .0 |
| $\Delta I_S/I_o$ | .162 | .245 | .245 | .15 | .32 |
| $I_{c1}/I_o$ | .284 | .429 | .549 | .66 | .50 |
| $(I_{c2} + I_{c3})/I_o$ | .185 | .185 | .185 | .19 | .18 |

NOTES

(a) The current $\Delta I_x$ is the increase due to depression from the value $I_{xo}$ without depression.

(b) The electrode voltages in all cases are: $V_{c1}$ = -5.12 kV, $V_{c2}$ = -9.55 kV, $V_{c3}$ = -16.0 kV.

A major difference in the observed and estimated current distributions is the reduced transmission (72.4%) into the collector region even without depression. Because the interception on the coupled cavity circuit was found to be very small, at least with a peaked magnetic focusing field, it would be possible to improve the transmission into the collector dramatically by appropriate modifications of the pole piece and shield apertures. An estimate of the current distribution with perfect transmission (with depression) is also shown in Table VIII. It was obtained by assuming that the originally intercepted current consisted of low and medium energy electrons which were redistributed on the body, deflection magnet, shield and first electrode in the same ratio as the measured current components due to depression. If it is further assumed that with perfect shielding the registered body current goes to the first electrode, the current distribution is fairly similar to the distribution derived by trajectory analysis. The difference is a shift of 11% of the total current from the first electrode to the deflection magnet shield.

The presence of an axial leakage field would have the effect of increasing the electron backstreaming. A direct analysis of the two-stage collector with an axial magnetic field component was not possible with the computer program. Instead, a computer run was made with such a field in a cylindrically symmetric version of the test collector. An increased tendency of the central trajectories to return through the electrode apertures was noted, but the effect did not appear to be sufficiently significant to account for the observed excess current to the deflection magnet shield.

The results of a trajectory analysis with the strongly diverging beam model are included in the last column of the table. Evidently, the degree of assumed divergence is too severe.

Considering the presence of other sources of error, as discussed previously, it may be concluded that the corrected spent beam trajectory launching conditions predict a collector performance which is in fair agreement with the experimental results.

## VIII MULTISTAGE DEPRESSED COLLECTOR DESIGN

According to the initial plan, an optimized multistage collector with up to five depressed stages was to be designed and evaluated. The design procedures were intended to be verified through the evaluation of an optimized two-stage collector. Even before any test results had become available, however, computer investigations were started on some four-stage collector configurations. These involved simple modifications of the two-stage designs, by the addition of two intermediate electrodes.

The trajectory plot for one such four-stage collector is shown in Figure 26. It is a modification of the all-electrostatic collector in Figure 19. The efficiency of this collector was estimated to be 68 percent, or 9 percentage points higher than the efficiency of the two-stage design from which it was derived.

A similar modification of the two-stage collector with initial magnetic deflection (Figure 18) was not successful. Several of the low and medium energy electrons were not sufficiently deflected by the now-reduced electrostatic transverse force beyond the first depressed electrode, resulting from the intermediate electrode voltage between the two original electrodes. Also, as was discussed previously, the energy groups are more crowded together in a collector with initial magnetic deflection, making an electron sorting by energy more difficult. The scheme was therefore abandoned.

The first test results of the two-stage collector indicated that a greater spread of the low and medium energy electrons occurred, such that a substantially decreased number were collected on the first stage. Another collecting electrode was therefore added in the four-stage electrostatic design, located between the first stage and ground and having a depression voltage of 70 percent of that of the first stage. The effective decrease in the axial length of the initial deflection region was compensated for by moving the grounded back plate closer to the depressed deflection control electrode. A configuration was then found which, with the same original trajectory input conditions, produced no significant change in the trajectory pattern occurring in the four-stage design. The added stage would, however, collect some of the trajectories which would be actually more diverging than assumed in the beam model.

### TRAJECTORY DESIGN ANALYSIS OF FINAL FOUR-STAGE COLLECTOR

Generally the collector designs, which were analyzed with the originally derived spent beam model, were characterized by an electron sorting process which depended not only on the electron energy, but also, quite critically, on the trajectory launching conditions. In the four-stage collector in Figure 26, for example, it is seen that the fourth energy group is collected on all four electrodes*, depending on the launching position within the

*One of the trajectories of the fourth energy group is collected on the electrode with -12.5 kV depression, even though the initial kinetic energy is 12.5 keV. The reason why this is possible is the potential depression due to the space charge at the collector entrance.

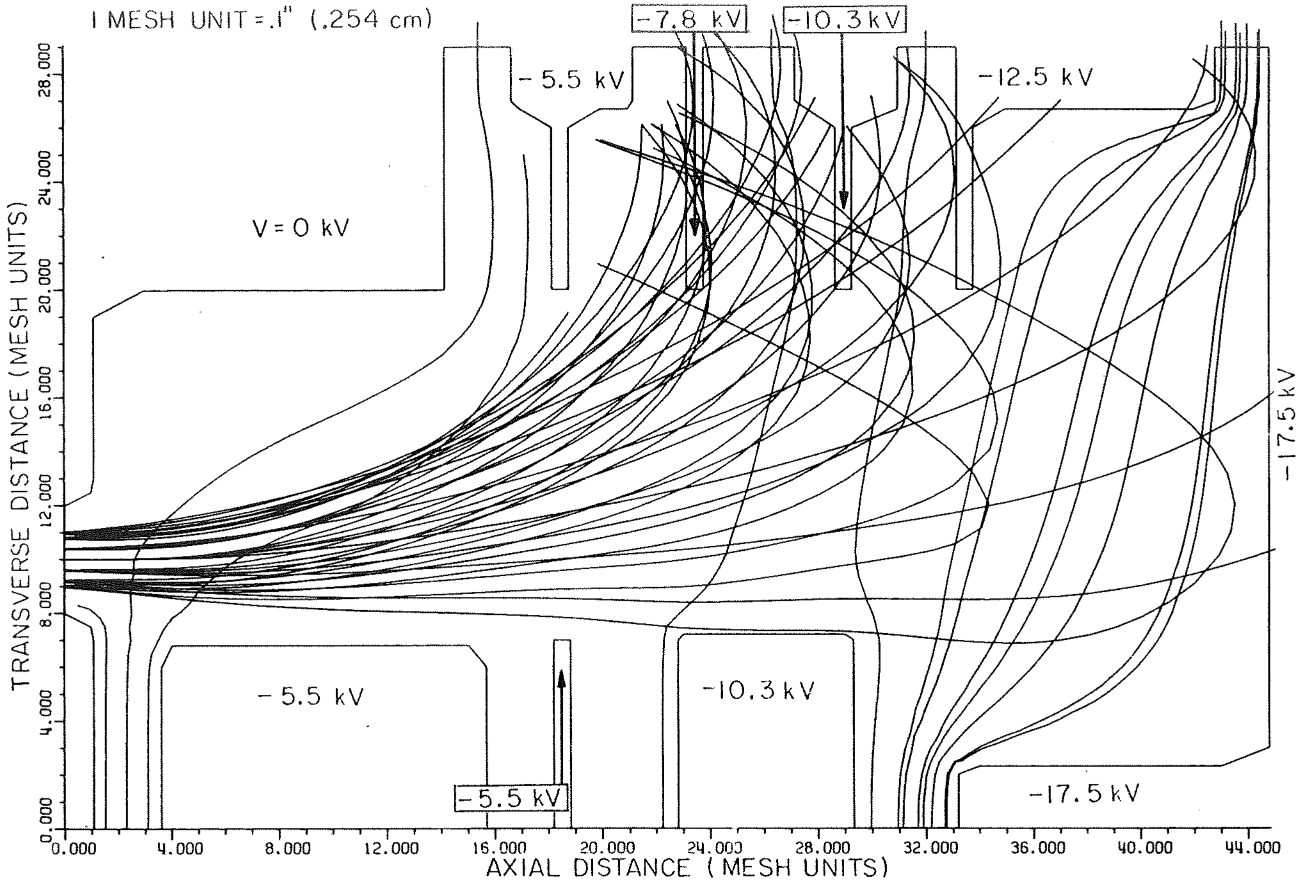


Figure 26 Four-stage depressed collector with electrostatic deflection.

beam. An inspection of the trajectories reveals that the initial trajectory angle would also be significant. When the space charge forces due to RF beam bunching were included in the derivation of the trajectory launching conditions into the collector, a greater variation in radial position and trajectory angle were found among the electrons composing an energy group. It was therefore desirable to modify the design to be more independent of the trajectory input conditions. This can be achieved by applying a greater deflection force. Generally it entails a reduction in efficiency, because of increased transverse velocity of the impacting electrons. Nevertheless, because of the uncertainties inherent in the analysis, and the relatively strong space charge forces, the approach used for the design of the final collector was to maintain a greater control of the beam.

A trajectory plot of the final four-stage collector is shown in Figure 27. The number of effective depressed stages was limited by the number of available feed-through connectors (seven), three of which would be used for the refocusing magnet, the first deflection control electrode and the non-collecting deflection electrode at the top. The remaining deflection electrodes are connected electrically to two collection electrodes. The composition of the beam used in the computation was the one calculated with the inclusion of RF space charge forces, and corrected, in a first approximation, for the spreading effect of the rotational motion in the beam (Table VII).

An indication of how well the beam is controlled is given by a comparison of Figure 27 with the trajectory plot obtained in the first iteration, displayed in Figure 28. The space charge forces in the collector region have thus not been included. It is seen that their effect is relatively minor. A computer run was also made with the strongly diverging beam model in Table VII. The final iteration of this run, including space charge forces, is shown in Figure 29. The low energy groups do not focus quite as well after turnaround, with a consequent loss of energy selectivity. Considering, however, that the assumed trajectory slopes represent worst-case estimates, the collector design is generally fairly insensitive to the variations in the electron trajectory angles.

The electrode configuration and the voltages were chosen to provide a smooth, relatively constant force on the electrons in most of the collector region. An optimized design of an ideal four-stage collector, based on the spent beam energy distribution at the output of the refocusing section, was used as a guide. This is believed to be appropriate for the present collector, in which the sorting is determined principally by the electron energy. (For the previously investigated collector types, the performance was more strongly dependent on the trajectory input conditions.) The spent beam energy distribution and an optimized design of the ideal four-stage collector is shown in Figure 30. The voltage step between the last two stages in the ideal design is about twice the step between the less depressed adjacent stages. To maintain an approximately uniform potential gradient, the distance between the last two stages has thus been made correspondingly larger.

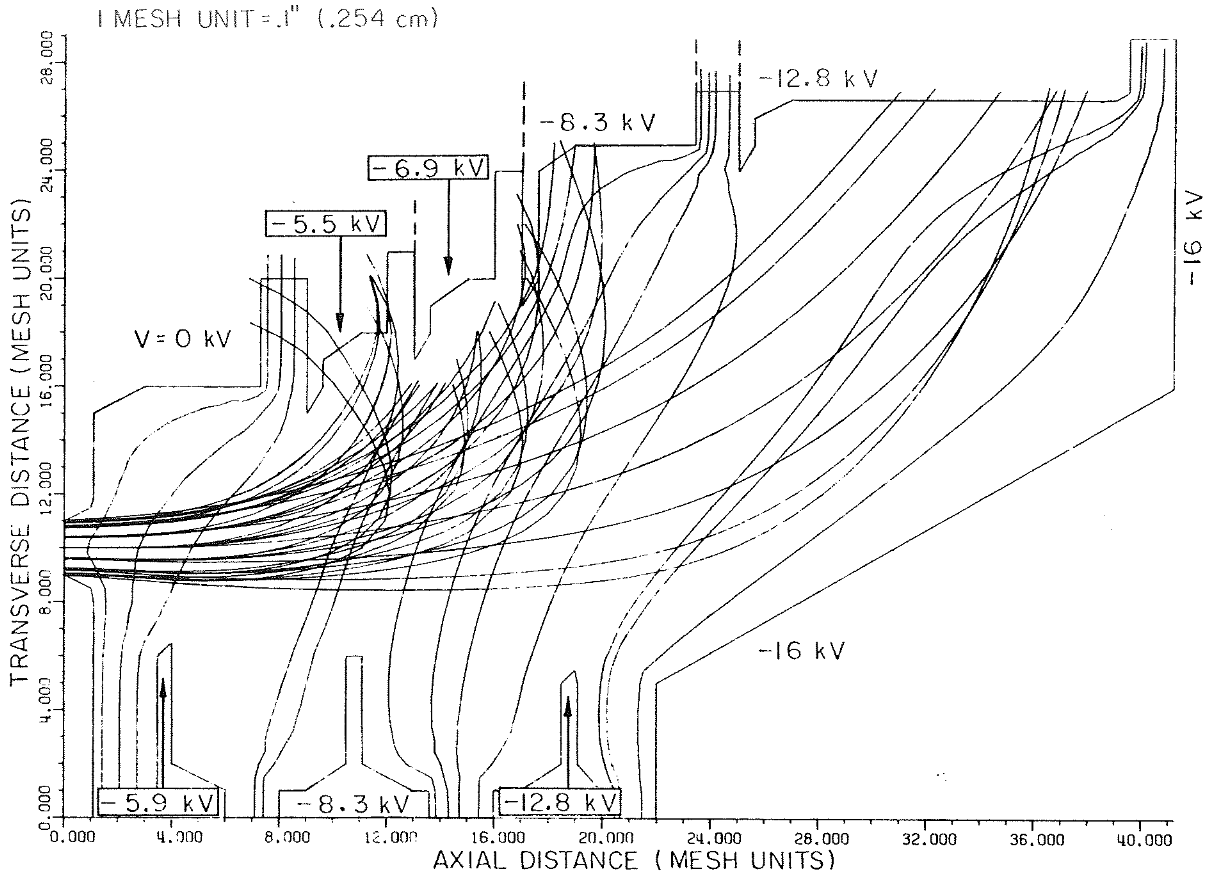


Figure 27 Calculated spent beam trajectories and equipotentials in final four-stage collector (space charge effects included).

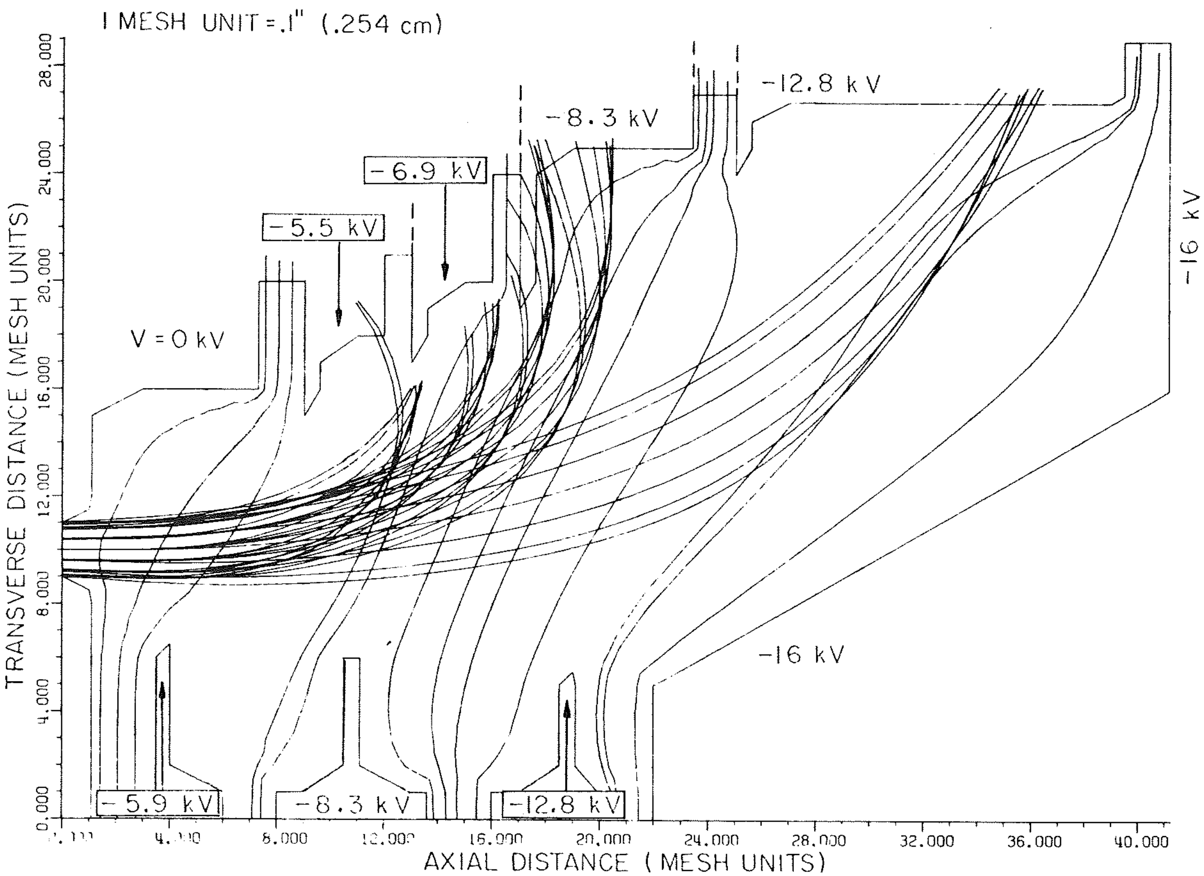


Figure 28 Calculated spent beam trajectories and equipotentials in final four-stage collector without space charge.

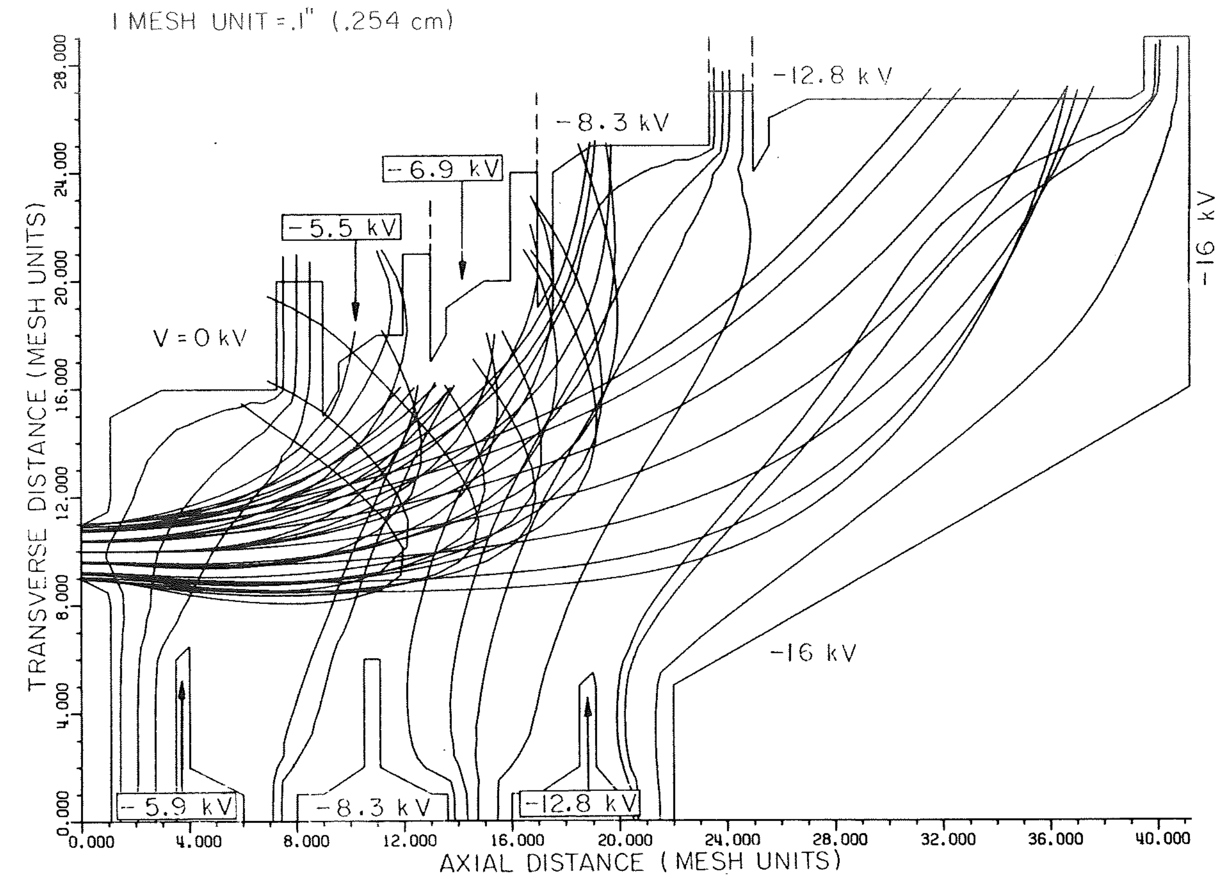


Figure 29 Calculated trajectories and equipotentials in final four-stage collector using strongly diverging beam model.

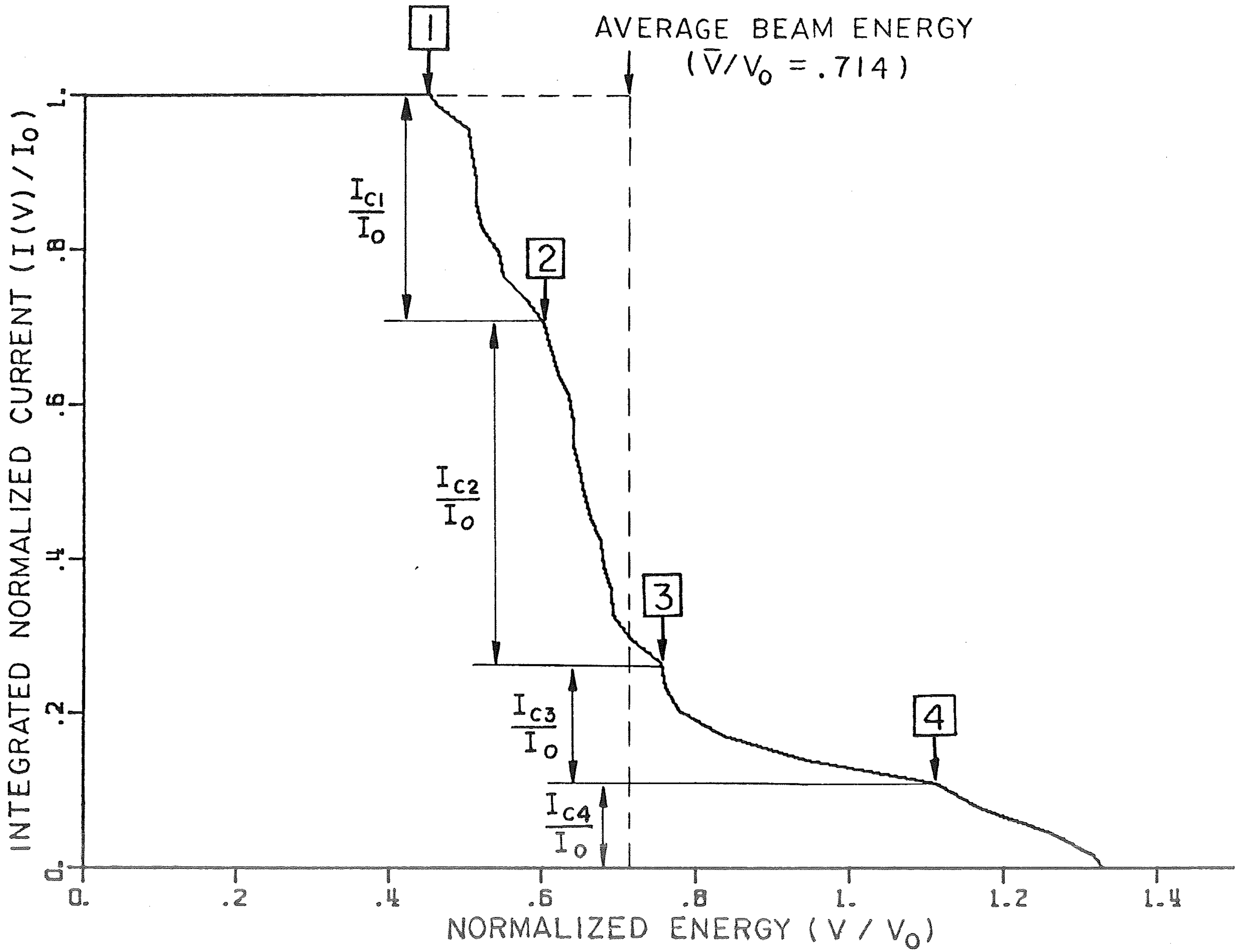


Figure 30 Spent beam energy distribution with optimized ideal four-stage collector design.

## ESTIMATED PERFORMANCE OF OPTIMIZED FOUR-STAGE COLLECTOR

The performance of the four-stage collector may be estimated in the following way. From the trajectory plot in Figure 27 it is found that the amount of energy recovered by the collector ranges from 67% for the slow group to 73% for the fast group. In case the trajectories of an energy group are collected on two different electrodes, as happens for the third group, the recovered energy may be weighted accordingly. On the average, therefore, about 70% of the energy is recovered. This would be a rough estimate of the collector efficiency.

A more valid calculation would be based on an increased number of energy groups. This would generally give a lower efficiency, as was observed in the analysis of the two-stage test collector with four and five energy groups. In the four-stage collector, however, the efficiency reduction with added energy groups is expected to be larger than in the two-stage collector because of the greater energy selectivity.

Another method of calculating the expected collector efficiency is to start from the ideal four-stage collector. Its performance is summarized in Table IX. Even though all the energy of a given electron could be recovered by an ideal collector, the distribution of electron energies is a spent beam would require an infinite number of electrodes for 100% collector efficiency. For the four-stage collector, the efficiency is 89%.

The relative decrease in efficiency due to finite number of stages can also be applied to the actual non-ideal collector, provided the maximum amount of energy recovered from a typical energy group is known. A measure of the maximum recoverable energy is obtained when an entire energy group just barely reaches a depressed stage. (Because of the spatial spread of the trajectories of an energy group at collection, this would still be an underestimate; for an increased number of stages additional energy would be recovered from some of the electrons in the group.) In Figure 27, all the trajectories of the first energy group are collected on the first electrode, but evidently, this would still happen for an increased amount of depression. The margin is closer for the second energy group, which is collected entirely on the second electrode. The recovered energy for this group is somewhat less than 73 percent. Using this number as the maximum collection efficiency for a typical group, and multiplying by the correction factor .89 applicable for four stages, gives an efficiency of 65 percent for the actual four-stage collector.

In a similar analysis with the strongly diverging beam model (Figure 29), the recovered energy varied monotonically from 61 percent for the slow group to 73 percent for the fast group. The average collection efficiency was 67 percent, or three points lower than for the first beam model. To take the variation in trajectory launching conditions into account to some extent, a compromise procedure was adopted to arrive at a best estimate. The maximum

TABLE IX ESTIMATED PERFORMANCE OF FOUR-STAGE COLLECTOR

| Stage k | Ideal Collector | | Actual Collector ($V_o$=16kV) | | |
|---|---|---|---|---|---|
| | $-V_{ck}/V_o$ | $I_{ck}/I_o$ | $-V_{ck}/V_o$ | $V_{ck}$(kV) | $I_{ck}/I_o$ |
| 1 | .45 | .29 | .30 | - 4.8 | .29 |
| 2 | .6 | .45 | .41 | - 6.6 | .45 |
| 3 | .76 | .15 | .53 | - 8.5 | .15 |
| 4 | 1.11 | .11 | .80 | - 12.8 | .11 |

Notes:

(a) Calculated spent beam power: $P_b$ = .714 $I_oV_o$.

(b) For ideal collector, recovered power = .637 $I_oV_o$; $\eta_c$ = 89%.

(c) For actual collector, recovered power = .44 $I_oV_o$; $\eta_c$ = 62%.

recoverable energy for a typical energy group was reduced from 73 to 70 percent. Correcting by the factor .89 for four stages gives a collector efficiency of 62 percent. This is considered a conservative estimate. However, degrading effects due to initial or acquired motion perpendicular to the symmetry plane have not been included.

A summary of the estimated performance characteristics of the collector is given in Table IX. The optimized electrode potentials are assumed to be about 70 percent of the ideal potentials. The electrode currents should be similar to the ideal currents under these conditions, although some current would go to ground potential. It may be noted from the spent beam energy distribution in Figure 30, that relatively small changes in the potentials of the second and third electrodes will produce significant changes in the electrode currents. The change in efficiency will be minor, however, since by virtue of the optimization $\partial \eta_c / \partial V_{ck} = 0$.

The collector combined with a (lossless) 28 percent efficient traveling-wave tube would give an overall efficiency of 51 percent. For the stacked coupled-cavity circuit, for which the power loss at saturation was estimated to be .58 kW, the overall efficiency would be 48 percent, assuming 97 percent transmission into the collector. It is believed that with the modifications which are described in the following subsection, this transmission could be achieved.

CONFIGURATION OF FOUR-STAGE COLLECTOR

The actual design of the four-stage collector, which was planned for evaluation in the demountable apparatus, is shown in Figure 31, in the plane of reflection symmetry. It corresponds closely to the configuration used in the trajectory calculations.

In the computer runs a planar collector geometry was assumed, with an appropriate planar simulation of an initially cylindrical beam. An effort was made to maintain planar symmetry in the actual collector, within the constraints of the available test apparatus. The electrode outlines are shown in Figure 32.

The planar geometry extends over a distance of about one inch (2.5 cm) from the symmetry plane. As a check on the design, an estimate was made of the extent of electron displacement perpendicular to this plane in the collector. An initial transverse velocity in this direction may be caused either by a radial velocity component or an angular velocity component. Since these components are mutually perpendicular, both of them cannot be maximally effective simultaneously. Worst-case estimates of the radial trajectory slopes yield transverse velocities typically equal to $.2 \times 10^9$ inches/s ($.5 \times 10^9$ cm/s). The time of flight in the collector for the corresponding electrons was obtained from the computer print-out. It was at most 2.5 ns, resulting in a displacement of .5 inches (1.3 cm). The maximum angular velocity, assuming a cathode flux of 87 percent relative to the DC beam and laminar flow, is $.15 \times 10^9$ inches/s ($.38 \times 10^9$ cm/s). The

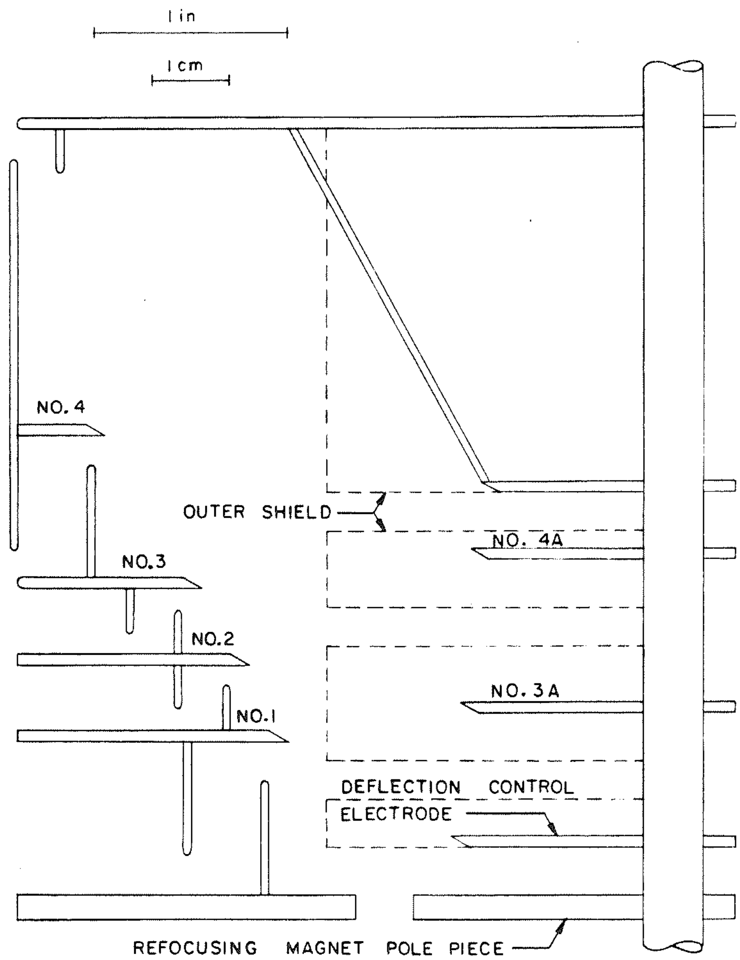


Figure 31 Schematic of final four-stage collector in plane of reflection symmetry.

maximum time of flight, which was applicable in this case, was 2.8 ns, producing a displacement of about .4 inches (1 cm). Effects due to space charge and non-laminar flow may contribute another half inch (1.3 cm). The collector configuration is therefore reasonable, although a greater margin might have been desirable.

An elaborate shielding arrangement, shown only partially in Figures 31 and 32, was designed to prevent electrons from escaping to the vacuum envelope, or being captured on the ceramic spacers. Grooves machined into the gun side of the active part of the electrodes were planned in order to minimize grazing incidence of electrons and thus reduce production of secondaries.

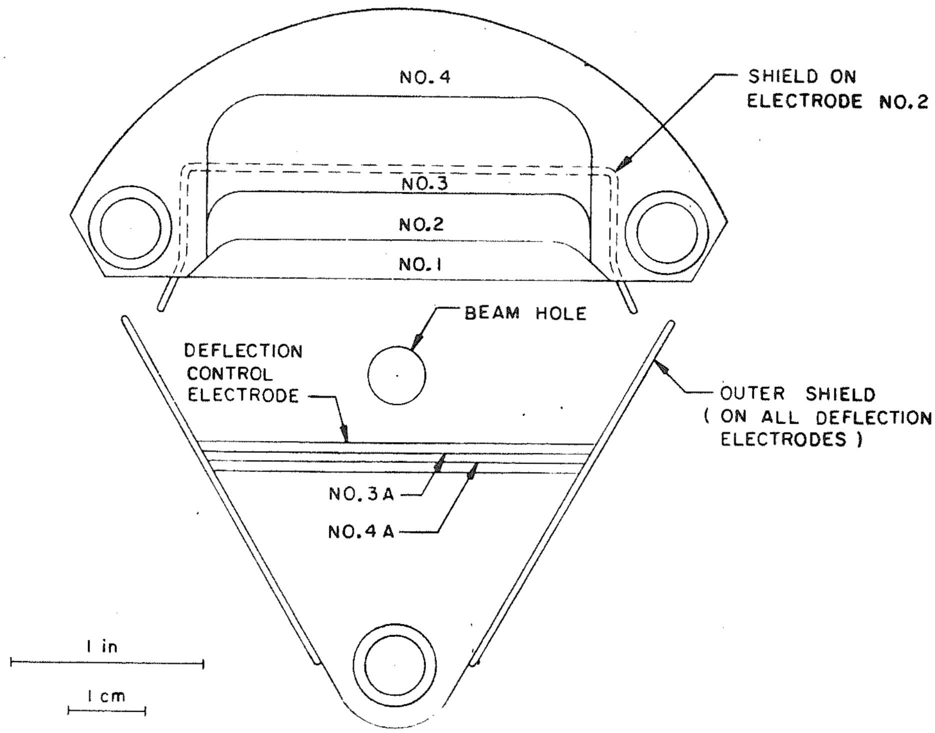


Figure 32 Electrode configurations in final four-stage collector.

To improve the beam transmission into the collector, the following modifications were planned. The beam hole in the main solenoid pole piece was to be chamfered with a radius of .075 inches (.191 cm) at the gun side and .100 inches (.254 cm) at the collector side. This should very effectively reduce the interception on this pole piece, judging from the trajectory plot in Figure 22, and the measured negligible interception on the RF circuit (the beam hole radius of the circuit was .050 inches). The beam hole in the refocusing magnet pole piece was to be similarly chamfered with radii of .1375 inches (.349 cm) and .1575 inches (.400 cm). The slight change in the magnetic field expected as a result of these modifications should have no significant effect on the refocusing characteristics. It was also planned to reduce the amount of field peaking at the output of the traveling-wave circuit from 20 percent, maintained in the improved focusing experiment, to 10 percent.

## IX DISCUSSION OF RESULTS AND SUGGESTED DIRECTION OF FUTURE STUDIES

It has been shown that the measured and calculated performance of the two-stage test collector were in fair agreement. This conclusion is somewhat obscured because certain assumptions had to be made as a result of perturbing effects in the experiment (relatively large current interception and imperfect shielding of the collector region). The method of analysis developed was therefore basically sound, even though it was based on some recognized approximations.

It is thus believed that the design analysis of the final four-stage depressed collector is valid, particularly since the design was made relatively insensitive to uncertainties in the velocity distribution of the incident beam. Because of constraints imposed by the demountable apparatus on the construction of the asymmetric four-stage collector, its geometry was quite complex. Without these constraints, a considerable simplification of the structure could be achieved. Even so, a cylindrically symmetric structure would generally be preferable from a construction point of view.

The predicted efficiency of the four-stage collector was 62 percent. This is comparable to a reported collector efficiency of 63 percent with a cylindrically symmetric electrostatic collector having ten depressed stages and operated on a klystron with a basic efficiency of 45 percent.[2] Considerably higher efficiencies (approaching 90 percent) have been predicted for a slightly different type of symmetric electrostatic collector.[4] Since both the analysis and construction of an asymmetric collector is appreciably more difficult, the two types of asymmetric collectors which were investigated (the electrostatic type and one with limited magnetic deflection) would thus stand at a disadvantage to a symmetric design. Upon request from NASA, the four-stage collector was therefore not evaluated.

An asymmetric electrostatic multistage collector might be desirable in certain applications. A base plate cooling scheme, for example, would benefit from a collector in which the heat is generated on one side. It would be desirable in such a case for the tube to be operated with a shielded cathode to minimize angular electron velocities. Also, magnetic shielding of the collector should be provided, and an effort made to minimize other field irregularities.

Another kind of asymmetric collector, utilizing an axial magnetic field, which has recently been investigated analytically, has shown promise of efficiencies up to 80 percent.[3] The magnetic field in this case is used more to confine the beam than to sort it, which is a distinct advantage, since the detrimental effect of beam spread due to space charge has been shown to be considerable.

One way of considering the difference between an asymmetric and a symmetric design is that in the former type of collector, the whole beam is deflected to one side, whereas in the latter type only half the beam is deflected to one side. The asymmetric collector therefore has to provide a sorting of electrons for which the variation in initial transverse velocities is twice that in a symmetric collector. Also, the beam is evidently allowed to spread less in an asymmmetric collector, which results in stronger space charge forces. The reason why an asymmetric collector with an axial magnetic field appears attractive is that it reduces the beam spread due to both these effects.

One advantage of an asymmetric design is the relative ease with which a tilted electric field of variable angle can be achieved for increased control over the beam. In a cylindrically symmetric design, there are practical difficulties in obtaining a specified potential along the axis to produce a similar effect.[2]

The general analysis procedure, which was developed for the asymmetric collector types in the present investigation, is equally applicable to symmetric designs. A very attractive feature of the method is that it is based on a calculation of the entire electron motion from the beginning of the interaction region. In most collector studies which have been conducted so far, independent assumptions have been made for the trajectory input conditions into the collector. The analysis procedure does, however, contain some approximations, the effect of which should be determined. In particular, an exact treatment of the gap fields in a coupled cavity structure would be desirable.

The detailed nature of the trajectory launching conditions into the collector remains as one of the main uncertainities in the analysis. An effort should be made to obtain experimental corroboration of the calculated spent beam energy distribution in a given application. Also, an experimental evaluation of an expansion and refocusing scheme would be another profitable subject of study, to verify the validity of the computer-derived electron motion. This would be especially valuable if an RF modulated spent beam were used, but even an investigation with a DC beam would be significant.

## X CONCLUSIONS

An investigation was made of a multistage collector for efficiency enhancement of traveling-wave tubes.

A method of analyzing an asymmetric collector scheme, either all-electrostatic or one with transverse magnetic field, was developed. The analysis procedure was verified to be basically valid, by comparing the predicted and measured performance of a two-stage test collector employing initial magnetic deflection of the spent beam. An attractive feature of the analysis method was that the entire electron motion from the beginning of the RF interaction to the capture in the collector was calculated in a well-defined manner.

The asymmetric all-electrostatic collector scheme promised to give higher efficiency than a scheme using initial magnetic deflection of the spent beam. A four-stage electrostatic collector with a predicted efficiency of 62 percent was designed. If applied to a traveling-wave tube of 28 percent basic efficiency, it would achieve an estimated overall tube efficiency of about 50 percent.

The performance of an asymmetric electrostatic collector is, at best, comparable to the performance of a cylindrically symmetric electrostatic collector. Since both the construction and analysis of an asymmetric collector are more complex than for a symmetric type, it is generally not as practical. In certain applications, such as for a device with base plate cooling where heat generation in a plane is desirable, it may, however, be advantageous.

## APPENDIX A

## DC-TO-RF POWER CONVERSION EFFICIENCY AND COLLECTOR EFFICIENCY

The usefulness of a depressed collector on an electron beam device, such as a traveling-wave tube, is primarily measured by its ability to raise the basic efficiency of the device, $\eta_o$, to a higher value, $\eta$. For a traveling-wave tube, the basic undepressed efficiency is usually defined by the ratio of RF output power to the DC beam power:

$$\eta_o = P_{RF\ out} / (I_o V_o) \qquad (1)$$

If part of the spent beam is collected at one or more depressed potentials, a portion of the kinetic beam power, $P_c$, is recovered by the collector, resulting in a saving of the DC power supplied to the device. The efficiency with a depressed collector is then

$$\eta = P_{RF\ out} / (I_o V_o - P_c) \qquad (2)$$

The recovered power may be expressed by

$$P_c = -\Sigma_k I_{ck} V_{ck} \qquad (3)$$

where $I_{ck}$ is the current collected at the electrode with potential $V_{ck}$ relative to ground (for a depressed electrode $V_{ck}$ is negative, yielding a positive contribution to $P_c$).

For the purpose of comparing one collector design with another it is convenient to separate the collector performance from the traveling-wave tube characteristics. The concept of collector efficiency provides the means for such a comparison. The collector efficiency, $\eta_c$, is the fraction of the energy recovered from the incident spent beam. If the power of the spent beam is $P_b$, the collector efficiency is thus defined by

$$\eta_c = P_c / P_b \qquad (4)$$

The concept of collector efficiency is particularly useful in collector design analysis, since a certain fixed spent beam composition may be assumed in the evaluation of various collector configurations. Even if the actual spent beam is somewhat different, the collector efficiency tends to remain about the same, because there will be a corresponding change in the recovered power.

The power in the spent beam can be calculated only approximately. To relate the collector efficiency to the significant experimental property of overall tube-collector efficiency, the energy balance condition is made use of:

$$P_b = I_o V_o + P_{RF\ in} - P_{RF\ out} - P_{interception} - P_{circuit\ loss} \qquad (5)$$

The RF input power term, which is usually negligible, has been included here because the traveling-wave tube used in the experiments had low gain. The last two terms on the right hand side, the power dissipated by the intercepted current and the power lost by the resistive cavity walls (or lost by leakage in a stacked structure), can only be estimated. An example of such an estimate is found in Section VI. Using equations (1), (4) and (5), the overall efficiency can be expressed as

$$\eta = \frac{\eta_o}{1 - \eta_c (1 - \eta_o - \eta')} \qquad (6)$$

where

$$\eta' = (P_{\text{interception}} + P_{\text{circuit loss}} - P_{\text{RF in}})/(I_o V_o) \qquad (7)$$

Solving for $\eta_c$ gives the inverse relationship

$$\eta_c = \frac{1 - \eta_o/\eta}{1 - \eta_o - \eta'} \qquad (8)$$

## APPENDIX B

## NECESSITY FOR BEAM EXPANSION*

A preliminary analysis of the beam spread in the collector was made by considering the DC beam which was to be used in the experiments. The beam had a design perveance of .46 μperv. Its cathode flux parameter k, defined by the ratio of the magnetic flux passing through the cathode surface and the flux enclosed by the beam, was .87. For an ideal, non-thermal, non-laminar flow such a beam would require a focusing field of twice the Brillouin field.

Figure 33 shows the calculated beam contours in a field free region for various initial beam sizes in relation to the radius of the focused DC beam, $r_o$. For comparison, the beam contours in the case of zero cathode flux have also been plotted. The beam is assumed to have been expanded and refocused, as illustrated in Figure 34, so that it is launched in a condition of parallel flow. With no prior expansion, the beam spreads by more than a factor of three over a distance of 15-20 times the DC beam radius. This distance corresponds to about .5" (1.3 cm), which is the approximate length of the deflection region into which the beam from the refocusing section is to be launched. If the beam is first expanded to three times the DC radius, the subsequent spread in the field free region is less than 20% of the launching radius over the same distance. It was concluded that a beam expansion of three or more was desirable.

The method of producing such an expansion and refocusing of the beam is illustrated in Figure 35. A reduced magnetic field, which follows the main focusing field, causes an initial expansion of the DC beam, since it is no longer in balanced flow. In an extended region with reduced field, the beam would scallop about the larger balanced-flow radius ($r_o'$ in the figure) of the decreased field. If the reduced field region is terminated at the axial distance for which the beam radius is maximum, an expanded beam in parallel flow will be obtained.

For estimating the amount of field reduction and the length of the refocusing field region that is required to produce a given amount of expansion, the beam edge trajectories for the DC beam were calculated beyond the point of maximum radius for various magnitudes of reduced field. The results are depicted in Figure 36. It is seen that a DC beam expansion of a factor of three is achieved with a 60% reduction in the field over a distance of 26 beam radii, or about .75" (1.9 cm) in the present case.

A practical field configuration used for the expansion and refocusing of the spent beam is shown in Figure 7 of Section IV.

---

* Part of this work was carried out under a separate, parallel contract (NAS 3-11539), on the subject "Refocusing of the Spent Axisymmetric Beam in Coupled Cavity Traveling-Wave Tubes". It is here included for the sake of completeness.

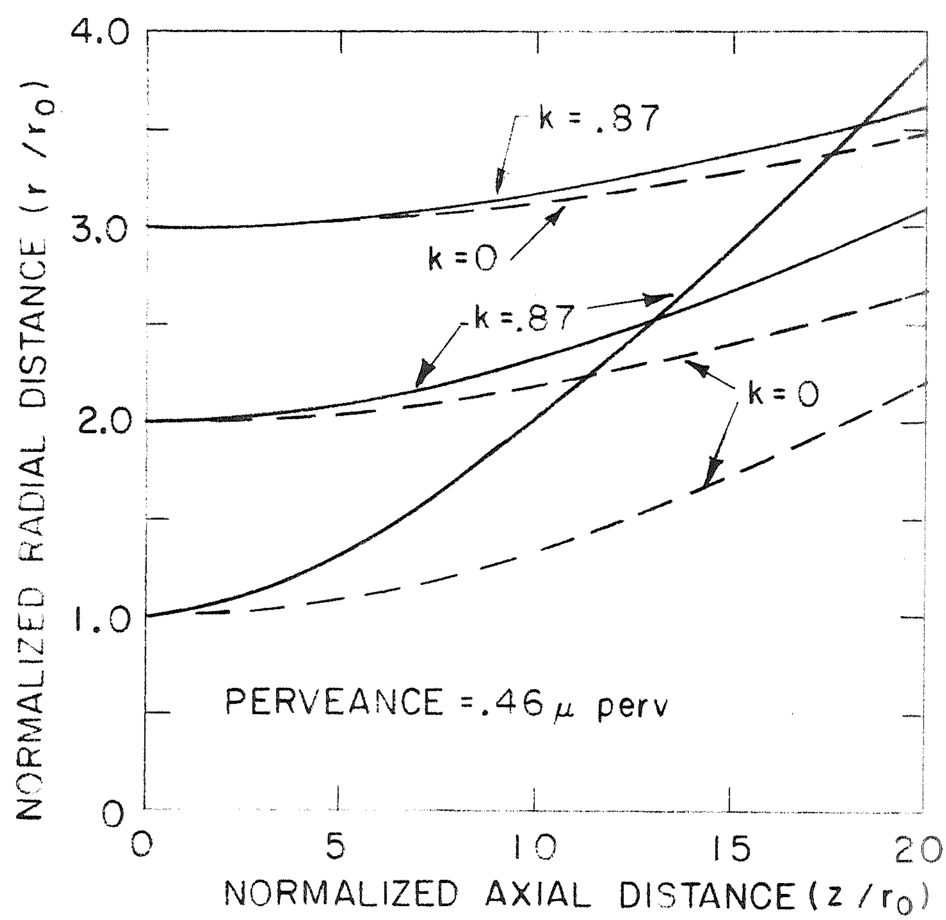


Figure 33 Calculated spread of an initially parallel beam in a field free region with and without cathode flux for various initial beam radii.

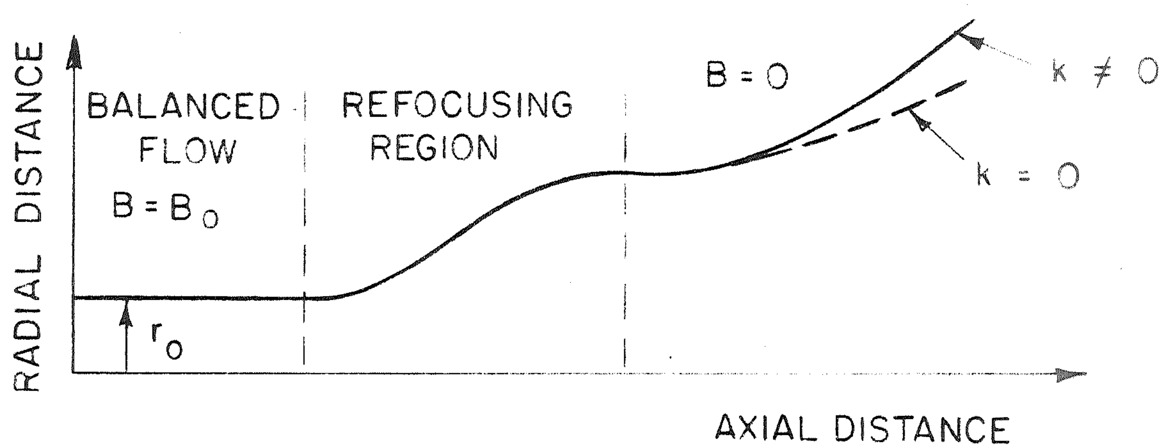


Figure 34 Beam development for achieving an expanded beam in parallel flow into a field free region, and its subsequent spread with and without cathode flux.

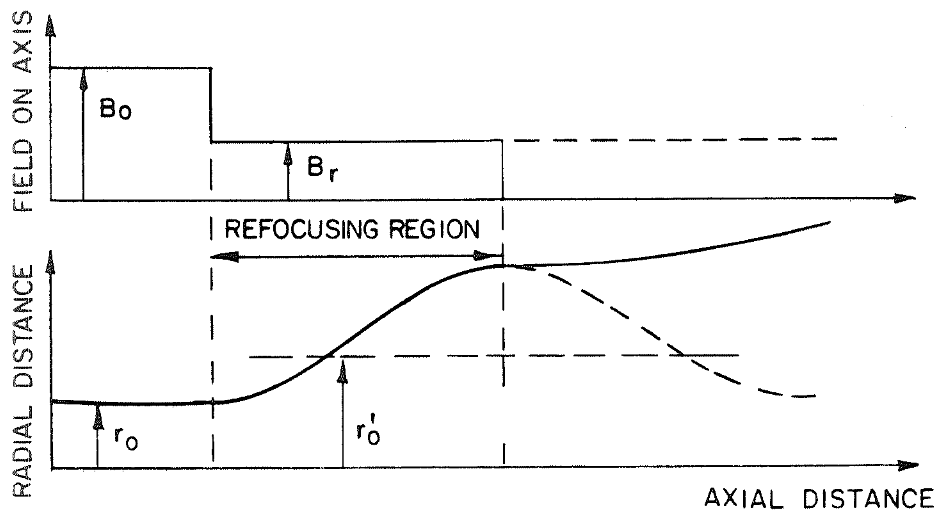


Figure 35 Idealized axial field for achieving an expanded beam in parallel flow.

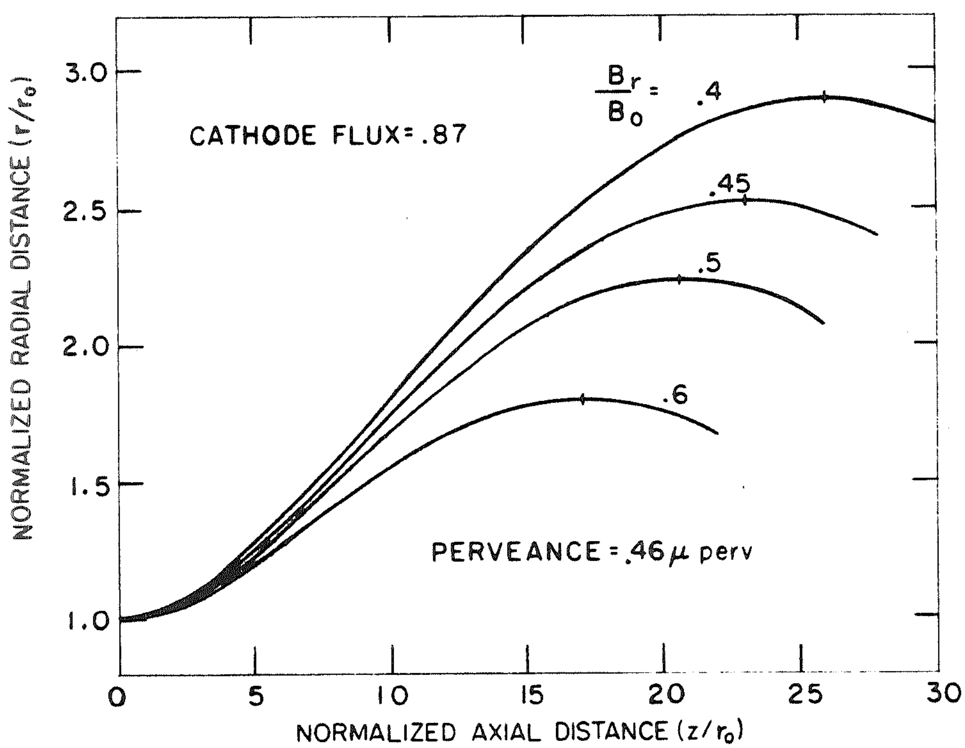


Figure 36 Calculated beam contours in a region with reduced constant magnetic field.

## APPENDIX C

## LARGE SIGNAL ANALYSIS OF RF CIRCUIT

An initial analysis of the coupled cavity X-band test circuit was carried out with a one-dimensional large signal computer program, for the purpose of selecting the operating voltage to be used in the collector evaluations. The one-dimensional program includes circuit loss and the space charge forces due to RF beam bunching, but is based on a disk model of the electron beam in which the disk radius is assumed to remain constant throughout. It could therefore not be employed to investigate the radial motion of the electrons. Later on in the study, a two-dimensional program, based on a disk model of the beam in which the disk radii are variable, became available. This program, which did not initially include RF space charge forces or circuit losses, was then used to evaluate the radial motion of the electrons in the RF circuit.

In the runs with the one-dimensional program, the beam voltage was varied from 15 kV to 22 kV with the gun perveance fixed at the design value of .46 μperv. The analysis was made at a single frequency (8.95 GHz). Predictions for the electronic efficiency and the efficiency with ideal optimized multistage depressed collectors were obtained. The results are shown in Figure 37, for collectors having up to five depressed stages. Although the calculated efficiencies with ideal depressed collectors are considerably higher than what can be expected with practical devices, they may be used as guides to determine the best operating conditions. It is seen that best performance for multistage collector operation may be expected at 16 kV beam voltage; it may also be noted that this is lower than the optimum voltage for maximum basic (undepressed) efficiency. A beam voltage of 16 kV was therefore selected and used for all subsequent work. The predicted efficiencies from a computer run with the two-dimensional program at 16 kV are also indicated in the figure. In this run circuit losses and RF space charge effects were not included. The difference in multistage collector efficiency for the two programs is typically 5%.

The ideal multistage collector predictions in Figure 37 are derived from the calculated spent beam energy distributions. The distributions obtained with the two programs for a 16 kV beam voltage are displayed in Figure 38. The normalized integrated current, $I(V)/I_o$, plotted as a function of the normalized equivalent voltage $V/V_o$, is the fraction of the beam current having kinetic energy greater than or equal to V. (An ideal DC beam would thus be represented by two lines drawn normal to the axis from the point $I(V)/I_o = V/V_o = 1$.) Also shown in the figure are the optimized bias voltages of the ideal depressed collectors with up to five stages, from which the efficiencies were calculated. The qualitative features are similar, although some disagreement can be noted for the optimum collector bias voltages.

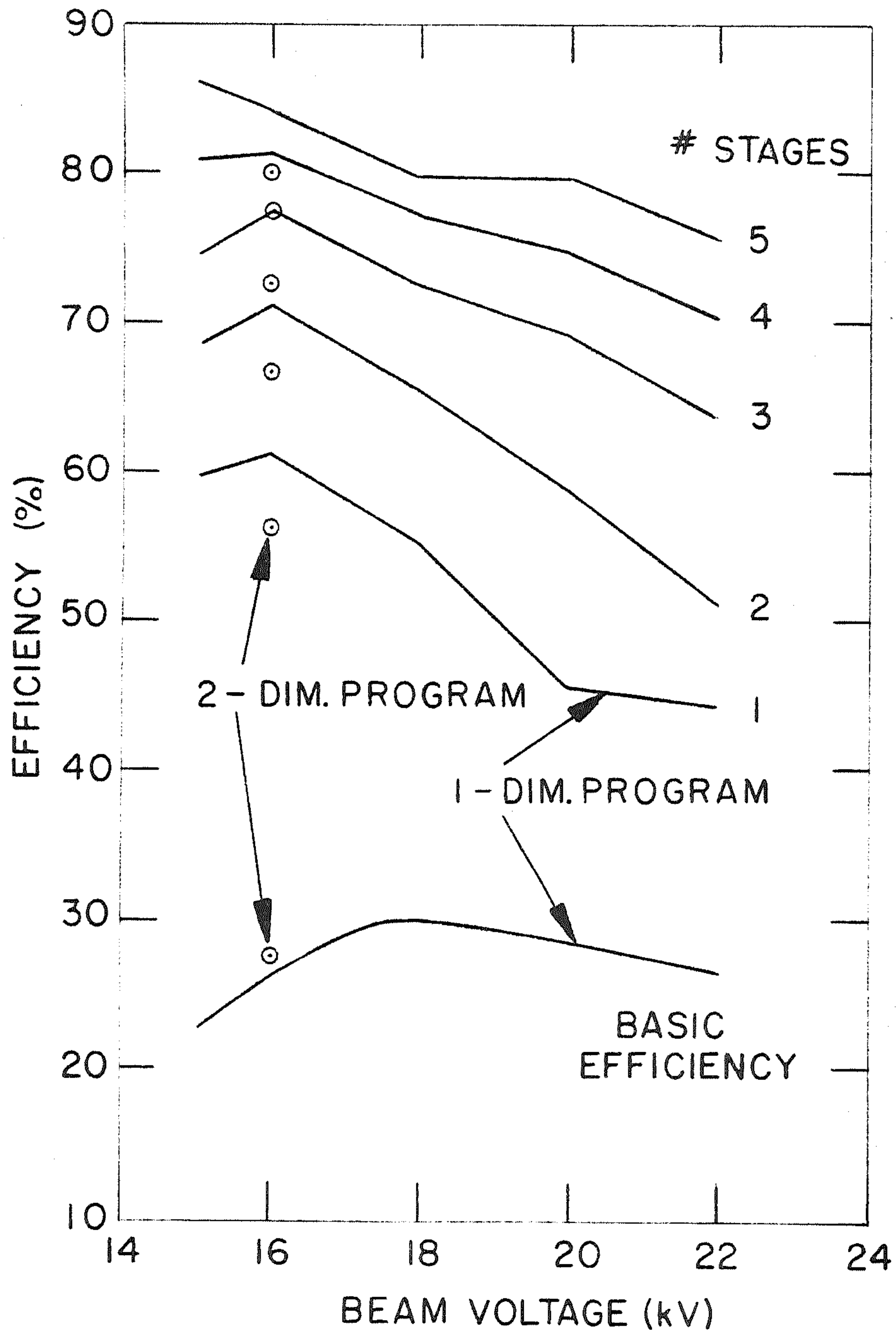


Figure 37 Optimum ideal multistage collector efficiencies computed with one-dimensional and two-dimensional programs.

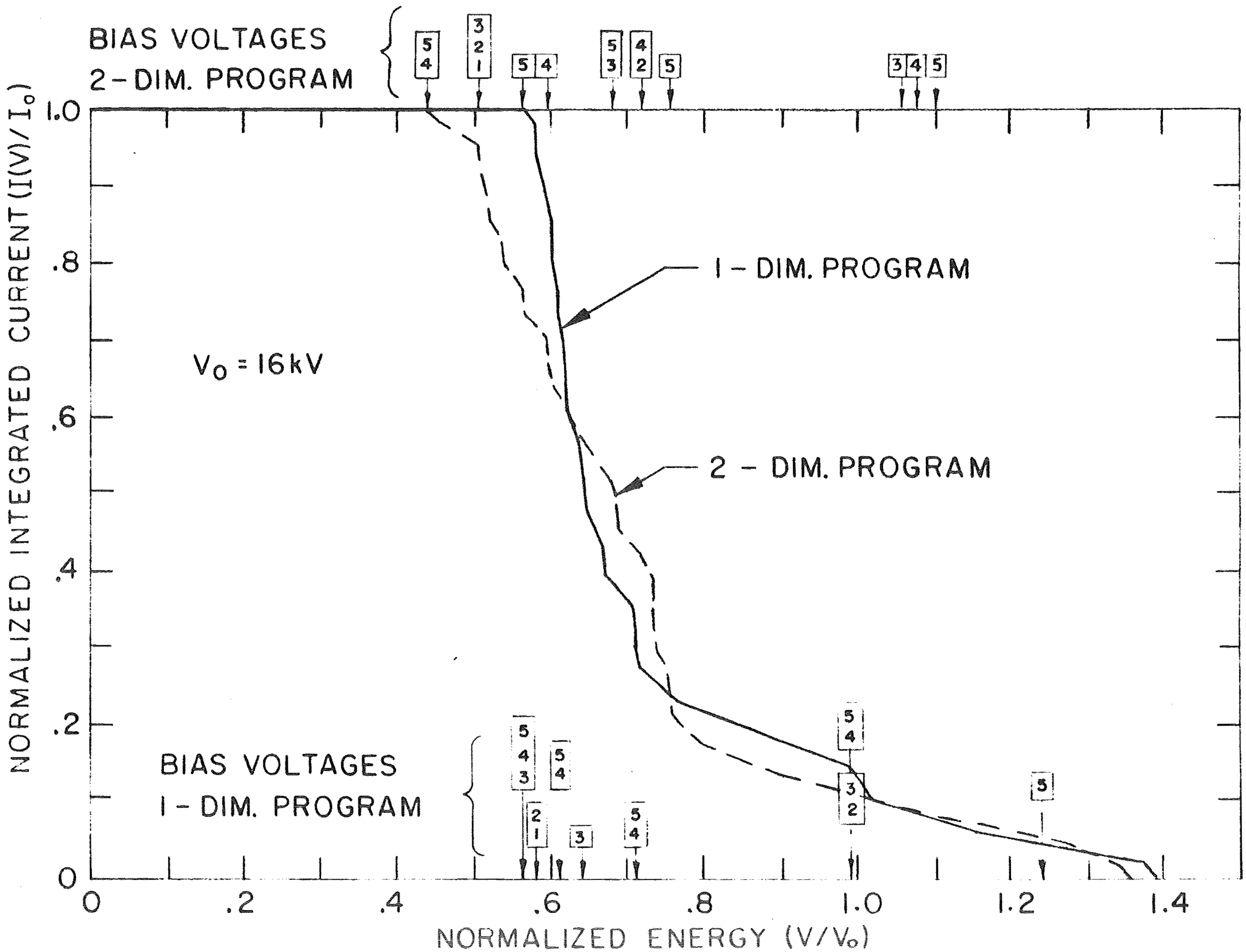


Figure 38 Spent beam energy distribution and optimum bias voltages of ideal multistage collectors up to five stages, computed with one-dimensional and two-dimensional programs (cathode voltage -16 kV).

## APPENDIX D

### DEBUNCHING OF THE SPENT BEAM IN A DRIFT REGION

In the large signal computer program, the electron beam is represented by disks of charge, which are initially uniformly spaced over an axial distance of one electronic wavelength. In the calculations, the spatial distribution of the disks around a given axial plane is expressed in terms of their phases relative to the phase of the RF wave, rather than in terms of distance. The initial uniform distribution in space is thus actually represented by a uniform distribution of disk phases, in the normalized range $-\pi$ to $+\pi$. A change in the bunching characteristics of a modulated beam is most conveniently studied by a plot of the disk phases as a function of distance.

Such a plot of the phases of all the 32 disks used to represent the beam is displayed in Figure 39, starting at saturation and extending through the refocusing region. (In a drift region, the phases are calculated relative to a fictitious circuit wave moving with a velocity equal to the undisturbed circuit wave velocity.) At saturation, the disks are bunched with phases between $-\pi/2$ and $+\pi/2$. Beyond saturation the bunch disperses because of the electron velocity spread. The space charge effects due to bunching have not been included in the computer run represented in Figure 39. The phase graphs are therefore straight lines because the axial disk velocities remain constant in the absence of RF wave and RF space charge forces. (The near-vertical lines which occur at the phase discontinuities due to the normalization should be ignored.) At the end of the refocusing region the phases are spread out quite uniformly over the whole range from $-\pi$ to $+\pi$, indicating that the beam at this point has no charge density modulation. The space charge forces will tend to bring about this condition more quickly and also tend to maintain it. This is seen in Figure 40 which is a similar plot calculated with the RF space charge forces included.

At the output of the refocusing section, the spent beam may therefore be considered to be a mixture of independent DC beams with several velocities.

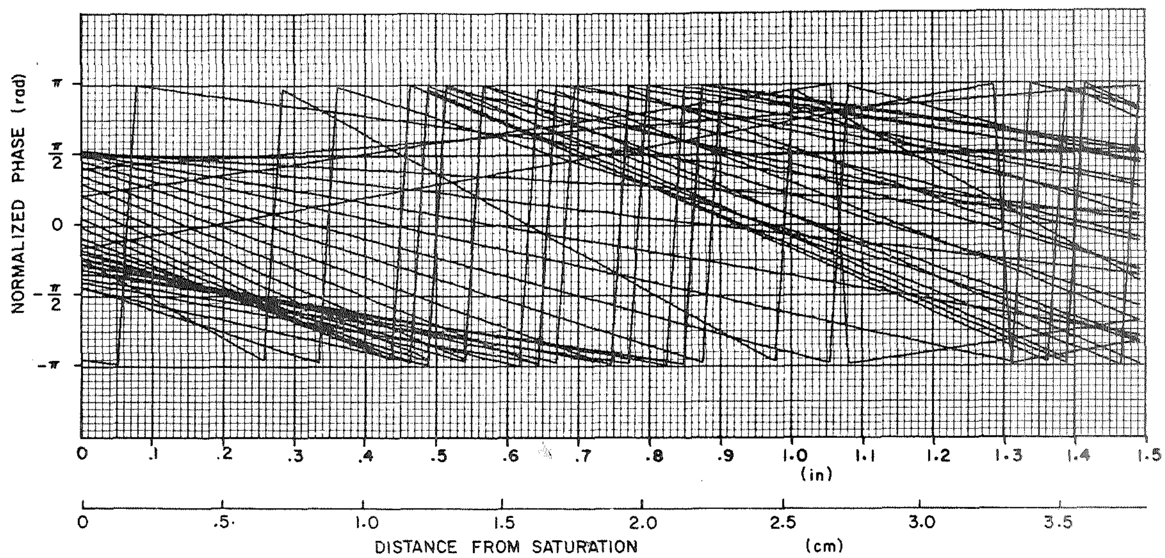


Figure 39 Normalized disk phases in refocusing region calculated without RF space charge forces.

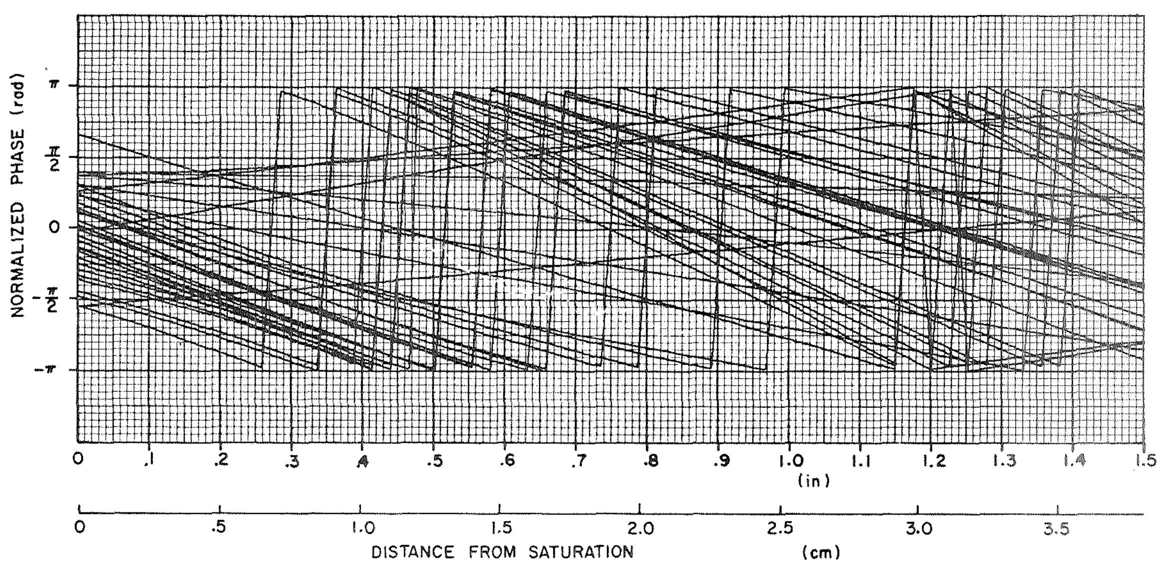


Figure 40 Normalized disk phases in refocusing region calculated with RF space charge forces.

APPENDIX E

EFFICIENCY EVALUATION FROM TRAJECTORY PLOTS

The collector efficiency, $\eta_c$, is evaluated from the computed trajectory plots in the collector region. It is defined by the ratio

$$\eta_c = P_c/P_b ,$$

where $P_c$ is the kinetic power recovered by the collector and $P_b$ is the incident power in the spent beam. The spent beam was in these studies represented by a reduced number of discrete energy groups, usually four or five. Letting the subscript j denote an energy group in the spent beam with (equivalent) voltage of $V_j$ and current $I_j$, the power in the spent beam may be expressed by

$$P_b = \sum_j I_j V_j$$

In order to calculate the effectiveness of a collector in recovering the kinetic energy in the spent beam, it is necessary to know what fraction of each energy group is collected at each different voltage in the depressed collector. If the fraction $f_{jk}$ of the current in energy group j is collected at a voltage of $V_{ck}$ relative to ground potential, the kinetic power recovered by the collector is obtained by

$$P_c = - \sum_{jk} I_j \; f_{jk} \; V_{ck}$$

With a given spent beam and given electrode voltages, the only unknowns are thus the fractions $f_{jk}$.

The computed trajectory plots supply information on the beam behavior in the plane of reflection symmetry. A simple method of obtaining the fractions $f_{jk}$ is to count the number of current-carrying trajectories in each group which are collected at the various voltages. This method is not appropriate in the present case, however. The collector geometry is complex, and some information on the trajectories on either side of the symmetry plane is necessary. Also, the great spread of some of the energy groups produce large variations in the local current density in different regions of the collector; therefore, giving equal weight to each trajectory may not be satisfactory.

The method which has been adopted consists in referring the beam behavior in the collector back to the beam entrance-plane by a mapping process. The assumption is that the current density at the entrance plane is uniform over the beam cross-section for each energy group. If a mapping can be made in this plane of the various potential regions at which the electrons are collected, the fractions $f_{jk}$ are simply given by the corresponding fractional areas. An example of this is shown in Figure 41, where the cross-section of energy group j has been divided into three regions

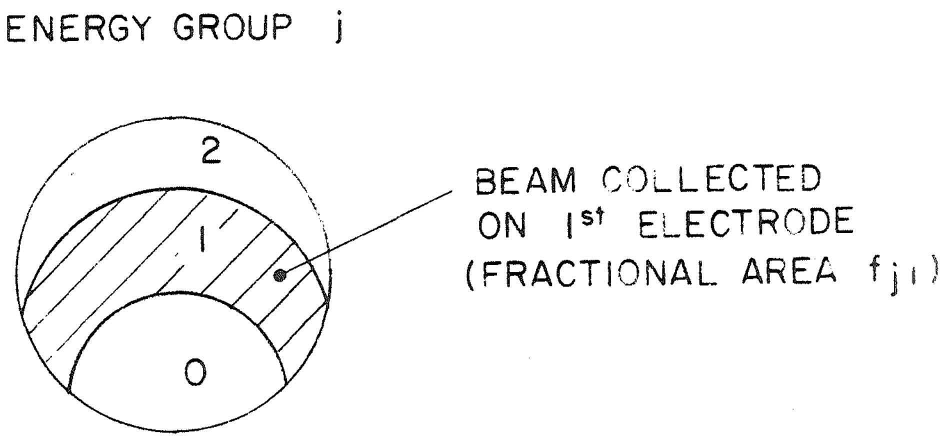


Figure 41 Mapping of the beam cross section of an energy group at the collector entrance.

corresponding to the collector voltages $V_{co}$ ( = 0, ground), $V_{c1}$ ( = potential of first electrode), and $V_{c2}$ ( = potential of second electrode). The fraction $f_{j1}$ of group j which is collected at potential $V_{c1}$ is evidently just the shaded fraction of the total beam area, because of the assumed uniform current density.

The following additional assumptions have been made for carrying out the mapping process:

(1) The transverse deflection in the direction parallel to the symmetry plane is independent of the originating distance from the symmetry plane.

(2) The impinging of an electron on the surface of an electrode causes a secondary electron to be emitted perpendicular to the intercepting surface.

(3) The beam spread in both transverse directions is of comparable magnitude, at least in a region not too close to trajectory turn-around.

As an illustrative example of the mapping process and the assumptions involved, the third energy group in the test collector will be analyzed in the plane of the second electrode before turn-around. In Figure 42, the trajectories of the third energy group from Figure 20 have been replotted separately. At the collector entrance, these trajectories originate along the vertical line in the cross-section diagram. Along this line, the trajectory plot supplies complete mapping information by interpolation. The top trajectory hits the edge of the first electrode. By assumption (2), a secondary electron is emitted, which falls back to ground potential. The top trajectory is therefore effectively collected at ground potential, designated by 0 in the diagram. The next two trajectories are collected at the potential of the first depressed stage, either directly or by emission of secondaries. The center trajectory as well as the bottom trajectory are collected on the second depressed stage. The two intermediate trajectories return to the first stage after having penetrated into the region between the second stage and the end plate. Evidently, some of the electrons between these two trajectories would fall all the way back to ground potential; this has been indicated in the cross-section map.

Assumptions (1) and (3) are invoked to complete the mapping at the collector entrance on either side of the line of symmetry. A detailed example is shown by the distribution of the trajectories in the plane of the second electrode. The location of the rays along the vertical line, in relation to the circular electrode aperture, is obtained directly from the trajectory plot. By assumption (1), all the electrons injected along the horizontal line through the center will remain in a horizontal line throughout the motion. To obtain the spacing between these electrons in the plane of the second electrode, assumption (3) is made use of. As seen in the diagram of this plane, the distance between the center ray and the two adjacent rays in the horizontal direction has been made comparable to the distance between the center ray and the two rays in the vertical direction. The remaining electrons along the horizontal line are spaced out with the just-established distance as a scale. The approximate boundary of the energy group at the second electrode can now be drawn in. The electrode aperture, which separates the electrons collected on the second stage from those collected on the first stage, is finally mapped out on the beam cross-section diagram at the entrance, by using corresponding mesh points as a guide. The other boundary lines for the energy group are mapped out in similar fashion.

The mapping diagrams of all the energy groups are shown in Figure 43. From the partial areas, which in practice were measured with a planimeter, the fractions $f_{ik}$ can be obtained. This allows a calculation of the power recovered by the collector, and hence the collector efficiency.

The procedure which has been described is most appropriate for collector configurations in which the transverse deflection of the beam as a whole is relatively small, such as in the test collector, in order to retain reasonable validity of assumption (3). For configurations with stronger transverse

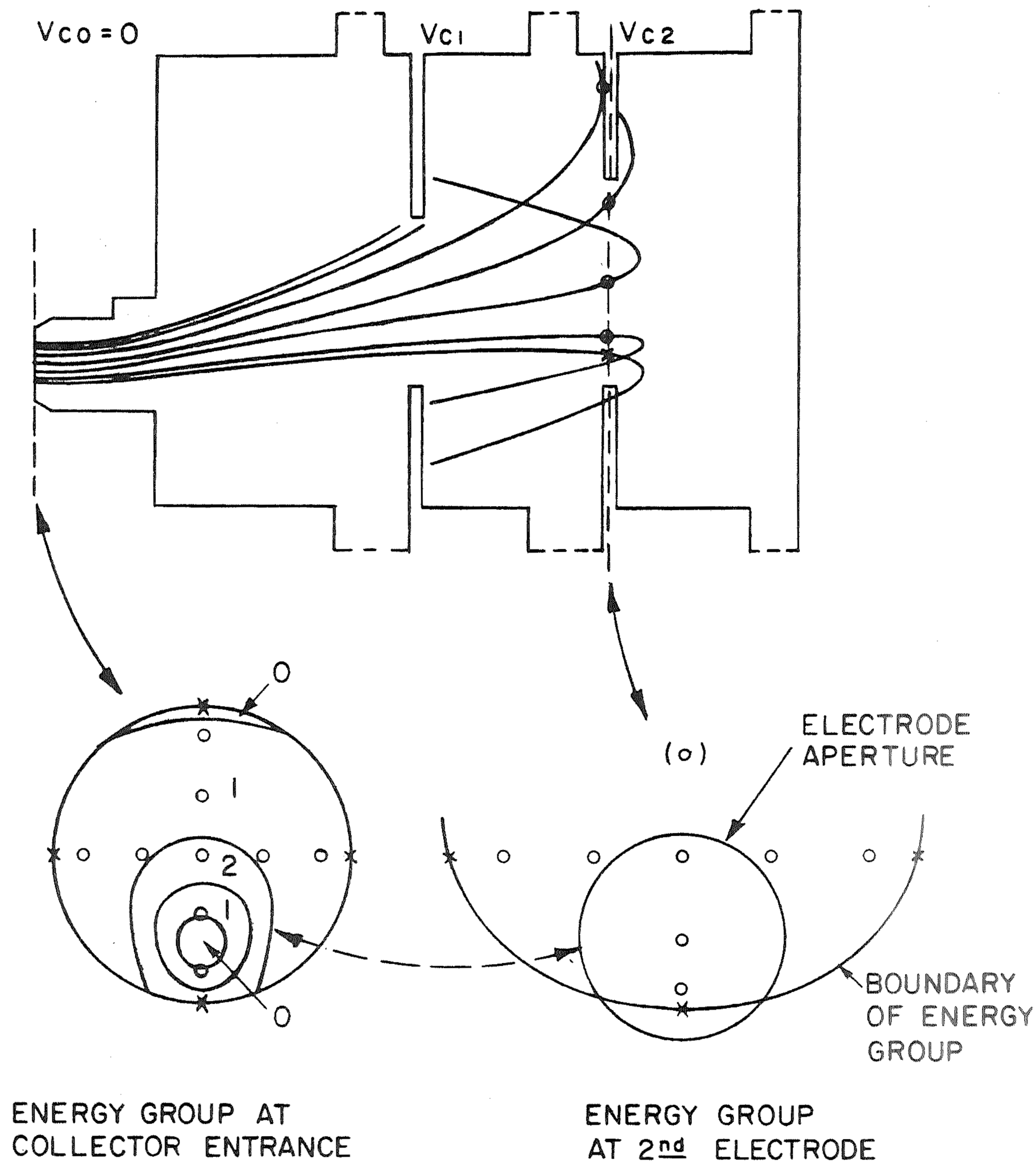


Figure 42 Illustrating the mapping procedure with the third energy group in the test collector in the plane of the second electrode before trajectory turn-around.

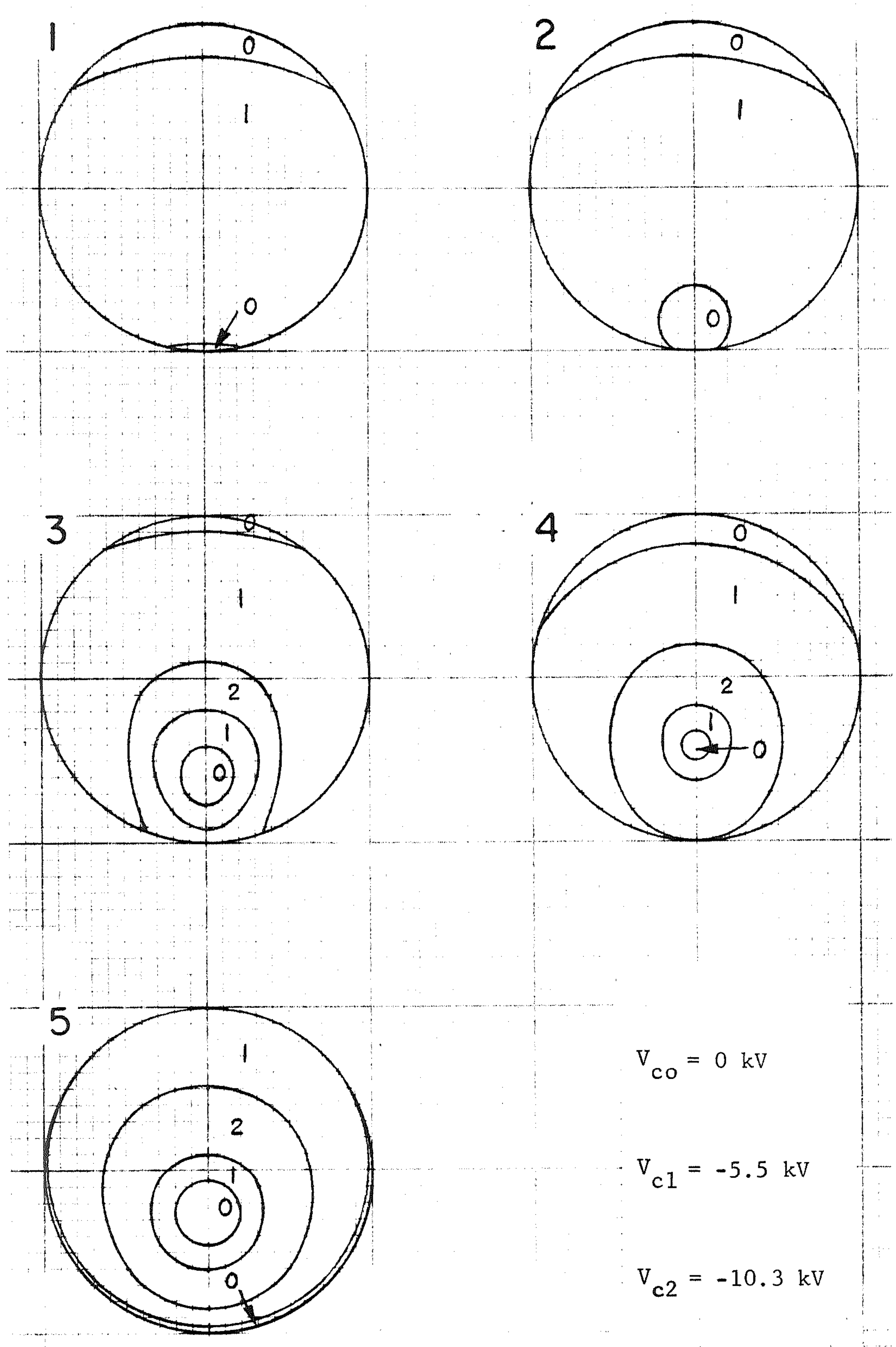


Figure 43 Mapping of beam cross-section at collector entrance for five energy groups in the two-stage test collector. The electrons in regions labeled 0, 1, and 2 are (effectively) collected at $V_{co}$, $V_{c1}$ and $V_{c2}$ respectively.

deflection, as in those employing additional electrostatic deflection force, a more independent judgment has to be made about the beam spread perpendicular to the symmetry plane. In these cases, the corresponding spread without transverse deflection can be used as a guide.

The presence of residual rotation in the expanded spent beam, resulting from non-zero cathode flux, makes assumption (1) only approximate. A distortion of the cross-sectional trajectory pattern takes place, such that reflection symmetry is no longer maintained. The expansion of the beam in the refocusing section reduces the effect, but it remains as one of the weak points in the analysis.

A different procedure has been used for the efficiency estimate of the final four-stage collector. This collector is an all-electrostatic collector with rather strong deflection, designed so that all the trajectories in an energy group end up fairly close together. The procedure, described in Section VIII. is therefore considerably simpler.

## REFERENCES


1. Sauseng, O. G.,Basiulis, A., Tammaru, I., "Analytical Study Program to Develop the Theoretical Design of Traveling-wave Tubes," NASA Final Report CR-72450, Contract No. NAS 3-9719, October 1968.

2. Neugebauer, W., Mihran, T. G., "Multistage Depressed Collector for Magnetically Focused Space Borne Klystrons," NASA Final Report CR-72767, Contract No. NAS 3-11532, September 1970.

3. Mihran, T. G., Neugebauer, W., "Analytical Study of a Depressed Collector for Linear Beam Microwave Amplifiers," NASA Final Report CR-72768, Contract No. NAS 3-11530, July 1970.

4. Kosmahl, H. G., "A Novel, Axisymmetric, Electrostatic Collector for Linear Beam Microwave Tubes," NASA Technical Note D-6093, February 1971.

5. Molnar, J. R.,Moster, C. R., "Some Calculations of the Magnetic Field Requirements for Obtaining Brillouin Flow in Cylindrical Electron Beams," Bell Telephone Lab Report 51-2940-1, January 1951.

6. Detweiler, H. K., "Characteristics of Magnetically Focused Large-Signal Traveling-Wave Amplifiers," RADC Technical Report TR-68-433 Contract No. AF 30(602)-3569, October 1968.

7. Gilmour, A. S., "Drive-Induced Current Minima in Velocity-Modulated Brillouin Beams" in "Theoretical and Experimental Investigations of Linear-Beam Microwave Tubes," RADC Final Report TDR-63-518, Contract No. AF 30 (602)-2573, School of Electrical Engineering, Cornell University, Ithaca, N. Y., December 1963.

## FINAL REPORT MAILING LIST

National Aeronautics & Space Administration
Headquarters
Washington, D. C. 20546

| | | |
|---|---|---|
| Attention: | SA/L. Jaffe | 1 copy |
| | SAC/A.M.G. Andrus | 10 copies |

NASA-Lewis Research Center
21000 Brookpark Road
Cleveland, Ohio 44135

| | | |
|---|---|---|
| Attention: | C. C. Conger (M.S. 54-1) | 1 copy |
| | R. E. Alexovich (M.S. 54-3) | 1 copy |
| | Dr. H. G. Kosmahl (M.S. 54-3) | 1 copy |
| | Technology Utilization Officer (M.S. 3-19) | 1 copy |
| | Library (M.S. 60-3) | 2 copies |
| | Report Control Office (M.S. 5-5) | 1 copy |
| | N. T. Musial (M.S. 501-3) | 1 copy |
| | G. J. Chomos (M.S. 54-5) | 50 copies |
| | J. R. Eski (M.S. 500-110) | 1 copy |

Communication Systems Inc.
5817 Columbia Pike
Falls Church, Virginia 22046

| | | |
|---|---|---|
| Attention: | J. Bisaga | 1 copy |

Rand Corporation
1700 Main Street
Santa Monica, California 90404

| | | |
|---|---|---|
| Attention: | Dr. J. Holt | 1 copy |

NASA Electronics Research Center
575 Technology Square
Cambridge, Massachusetts 02139

| | | |
|---|---|---|
| Attention: | E/Dr. L. Vanatta | 1 copy |
| | FM/C. Veronda | 1 copy |
| | Library | 1 copy |

NASA-George C. Marshall Space Flight Center
Huntsville, Alabama 35812

| | | |
|---|---|---|
| Attention: | RASTR-A/E. C. Hamilton | 1 copy |
| | Library | 1 copy |

NASA-Goddard Space Flight Center
Greenbelt, Maryland 20771

| | | |
|---|---|---|
| Attention: | 733/R. Pickard | 1 copy |
| | Library | 1 copy |

NASA-Ames Research Center
Moffett Field, California 94035

| | | |
|---|---|---|
| Attention: | OART-MOA/E. Van Vleck (M.S. 202-6) | 1 copy |
| | Library | 1 copy |

NASA-Langley Research Center
Langley Station
Hampton, Virginia 23365

| | | |
|---|---|---|
| Attention: | B. Kendall (M.S. 173) | 1 copy |
| | Library (M.S. 185) | 1 copy |

NASA-Manned Spacecraft Center
Houston, Texas 77001

| | | |
|---|---|---|
| Attention: | Library | 1 copy |

Jet Propulsion Laboratory
4800 Oak Grove Drive
Pasadena, California 91103

| | | |
|---|---|---|
| Attention: | L. Darr | 1 copy |
| | Library | 1 copy |

NASA Scientific and Technical Information Facility
Box 5700
Bethesda, Maryland 20740

| | | |
|---|---|---|
| Attention: | NASA Representative | 3 copies |

RCA Corporation
Astro-Electronics Division
Princton, New Jersey 08540

Attention: R. B. Marstin 1 copy

TRW Systems
One Space Park
Redondo Beach, California 90278

Attention: W. A. Finley/Space Vehicle Division 1 copy

General Dynamics/Convair Division
P. O. Box 1128
San Diego, California 92112

Attention: F. J. Dois/Advanced Programs 1 copy

Hughes Aircraft Company
Space Systems Division
1194 W. Jefferson Boulevard
Culver City, California 90230

Attention: H. A. Rosen/Satellite Systems Laboratory 1 copy

General Electric Company
Missile and Space Division
Valley Forge Space Technology Center
P. O. Box 8555
Philadelphia, Pennsylvania 19101

Attention: H. Collins 1 copy
P. Nadler 1 copy

Federal Communications Commission
521 12th Street
Washington, D. C. 20554

Attention: M. Fine 1 copy

U. S. Information Agency
25M Street S.W.
Washington, D. C. 20547

Attention: IBS/EF/G. Jacobs 1 copy

General Electric Company
Tube Department
Microwave Tube Business Section
Schenectady, New York 12305

Attention: R. Dehn — 1 copy

Litton Industries
Electron Tube Division
960 Industrial Road
San Carlos, California 94070

Attention: Dr. C. Pokerney — 1 copy
J. Orr — 1 copy
W. Day — 1 copy
Dr. O. Sauseng — 1 copy

SFD Laboratories Inc.
800 Rahway Avenue
Union, New Jersey 07083

Attention: Dr. G. Farney — 1 copy

Hughes Aircraft Company
Electron Dynamics Division
P. O. Box 2999
Torrance, California 90509

Attention: Dr. J. Mendel — 1 copy

Watkins Johnson Company
333 Hillview Avenue
Palo Alto, California 94304

Attention: Dr. D. Watkins — 1 copy

Varian Associates
611 Hansen Way
Palo Alto, California 94303

Attention: I. Maltzer — 1 copy

R.C.A. Corporation
Industrial Tube Division
Lancaster, Pennsylvania 17604

Attention: W. P. Bennett 1 copy

Raytheon Company
Research Division
28 Seyon Street
Waltham, Massachusetts 02154

Attention: W. Teich 1 copy
Dr. J. M. Osepchuk 1 copy

U. S. Naval Research Lab
Aerospace Radar Branch
Washington, D. C. 20390

Attention: Mr. Lawrence Dasch 1 copy

Martin-Marietta Corp.
Denver Division
P. O. Box 179
Denver, Colorado 80201

Attention: Mr. Robert Richardson 1 copy
(Mail No. 1620)

Philco Ford Corporation
WDL Division
3939 Fabian Way
M.S. C-70
Palo Alto, California 94303

Attention: Dr. William E. Waters 1 copy
Sr. Engr. Staff Specialist

NASA-Goddard Space Flight Center
Greenbelt, Maryland 20771

Attention: Mr. George Orr 1 copy
(Code 733)

Commander
Naval Electronic Systems Command
Attn: Code 05143141
Washington, D. C. 20360

1 copy